Université de Montréal

Nouvelles observations et techniques d'apprentissage automatique appliquées aux galaxies et aux amas de galaxies

par

Carter Rhea

Département de Physique
Faculté des arts et des sciences

Mémoire présenté en vue de l'obtention du grade de
Maître ès sciences (M.Sc.)
en Astrophysique et Astronomie

October 21, 2020

Université de Montréal

Faculté des arts et des sciences

Ce mémoire intitulé

Nouvelles observations et techniques d'apprentissage automatique appliquées aux galaxies et aux amas de galaxies

présenté par

Carter Rhea

a été évalué par un jury composé des personnes suivantes :

Pierre Bergeron
(président-rapporteur)

Julie Hlavacek-Larrondo
(directeur de recherche)

Daryl Haggard
(membre du jury)

Résumé

Les amas de galaxies sont l'une des plus grandes structures dans l'univers et jouent le rôle d'hôte de plusieurs phénomènes complexes. Bien qu'il existe beaucoup d'études portant sur leur formation et leur évolution, l'avènement récent de l'apprentissage automatique en astronomie nous permet d'investiguer des questions qui, jusqu'à maintenant, demeuraient sans réponse. Même si ce mémoire se concentre sur l'application de techniques d'apprentissage automatique aux observations en rayons X des amas de galaxies, nous explorons l'usage de ces techniques à son homologue à une échelle réduite : les galaxies elles-mêmes. Malgré le fait que les trois articles présentés dans ce mémoire se concentrent sur différents aspects de la physique, sur de différentes échelles et sur de différentes techniques, ils forment une base d'études que je continuerai pendant mon doctorat : l'usage des nouvelles techniques pour investiguer la physique des régions galactiques et extragalactiques.

Dans le premier article, nous introduisons les premières observations en rayons X d'un amas de galaxies lointain qui détient des attributs particuliers comme une formation stellaire hors pair ($\sim 900 M_{\odot}$/an). Dans cet article, nous employons les techniques traditionnelles en astronomie rayons X pour déterminer si ce taux de formation stellaire est dû à un courant de refroidissement désinhibé. Puisque l'objet est très lointain ($z = 1.7$), il faut faire nos calculs sans beaucoup de photons et il faut donc utiliser les indices par procuration. Nous déterminons que la galaxie centrale est séparée d'une distance de plus de 50 kpc du coeur froid de l'amas. À cause de cette séparation, le trou noir supermassif central n'est pas alimenté et il ne peut pas prévenir le courant de refroidissement. Ceci est le premier exemple d'un amas de galaxies où nous observons l'échec de la rétroaction d'un trou noir supermassif. De plus, ceci nous fournit un autre mécanisme qui peut créer la lumière intra-amas.

Dans le deuxième article présenté ici, nous examinons l'émission rayons X provenant du milieu intra-amas extrêmement chaud des amas de galaxies. Nous développons une méthode compréhensive qui détermine le nombre de composantes thermiques sous-jacentes dans un spectre de plasma. Notre nouvelle technique est basée sur une combinaison d'algorithmes d'apprentissage automatique non supervisé (analyse de composantes principales) et d'apprentissage automatique supervisé (arbre aléatoire). Nous créons un ensemble de 100 000 observations synthétiques et réalistes de *Chandra* qui représentent le gaz chaud dans les

amas de galaxies voisines. Après la réduction de notre ensemble d'entraînement à ses 25 composantes principales, nous entraînons notre classificateur afin qu'il puisse déterminer le nombre de composantes thermiques sous-jacentes. Une fois l'étape d'entraînement terminée et l'optimisation des hyperparamètres terminée, nous appliquons la méthodologie à l'amas de galaxies de Persée. En plus de créer une carte de l'amas qui indique le nombre de composantes thermiques nécessaires afin de modéliser précisément l'émission du gaz chaud, nous avons développé un ensemble d'outils numériques qui calculent les températures associées. Nos résultats sont en accord avec plus d'une décennie d'études sur l'amas de galaxies de Persée et nous indiquent qu'il faut utiliser plusieurs composantes thermiques pour modéliser le milieu intra-amas correctement.

Le troisième article présenté dans ce mémoire emploie de nouveau l'apprentissage automatique pour résoudre une question précédemment sans réponse nécessaire pour la caractérisation précise de la cinématique de gaz chaud dans les galaxies. Nous avons construit un réseau de neurones convolutif qui estime la vitesse et l'élargissement des raies d'émission d'un spectre de galaxies en visible. Une fois construit, nous l'appliquons aux données synthétiques qui répliquent les observations réelles de SITELLE du programme SIGNALS. En utilisant notre réseau bien entraîné, nous caractérisons l'émission d'une cible de SIGNALS : la galaxie M33. Nos résultats indiquent que notre algorithme surpasse les méthodes standards et s'adapte bien aux procédures d'ajustement spectral. En outre, notre méthodologie augmente la vitesse des calculs par plus d'un ordre de grandeur. Bien que l'algorithme soit entraîné spécifiquement pour SITELLE, on peut faire de petites modifications pour l'utiliser avec des autres interféromètres tels que MUSE et ses futurs analogues dans la prochaine génération de télescopes.

Notez que j'ai mené à titre de premier auteur deux des trois articles présentés dans ce mémoire et apporté des contributions majeures au troisième. Les trois articles ont déjà été acceptés pour publication ou ont déjà été soumis et révisés une fois.

Mots-clés: amas de galaxies – apprentissage automatique – régions H II – analyse de composantes principales – réseau de neurones convolutif – milieu interstellaire – milieu intra-amas – rayons X.

Abstract

Galaxy clusters are one of the largest structures in the universe and host several complex physical phenomena. Although a wealth of knowledge already exists on their formation and evolution, the recent advent of machine learning in the astronomical sciences has allowed us to probe questions hithertofore unanswered. While this thesis does focus heavily on the applicaiton of machine learning techniques to X-ray observations of galaxy clusters, it takes the techniques applied there to galaxy cluster's smaller counterparts: the individual galaxies themselves. Although the three papers presented here focus on distinct physics, scales, and techniques, they all form a basis of studies that I will continue during my doctorate: using new techniques to probe the underlying physics of galactic and extragalactic regions.

The first paper introduced is a study of a galaxy cluster near the beginning of the epoch of cluster formation exhibiting peculiar attributes such as an elevated stellar formation rate ($\sim 900 M_{\odot}/yr$). In this paper, we employ traditional techniques in X-ray astronomy to determine whether or not the prodigious formation rate is due to an uninhibited cooling core. Since the object is so distant ($z = 1.7$), we must execute our calculations with relatively few photons and thus rely on proxy measures. We determine that there exists a strong cooling flow offset by over 50 kpc from the central galaxy. Because of this offset, the AGN is not fueled and thus fails to heat up the cooling flow. This is the first example of a galaxy cluster in which we observe the failure of AGN feedback. Additionally, this provides another mechanism for the creation of intracluster light.

The second article presented here focuses on X-ray emission from the hot intra-cluster medium within the galaxy cluster. We develop a comprehensive method for determining the number of underlying thermal components in the plasma's spectra. Our novel technique relies on a combination of an unsupervised learning algorithm (principal component analysis) and a supervised learning algorithm (random forest classification). We create a set of 100,000 realistic mock *Chandra* observations of the hot X-ray emitting gas in nearby galaxy clusters. After reducing our synthetic training set to its 25 most important principal components, we trained a random forest classifier to distinguish between the number of underlying thermal components. After successful testing and hyperparameter optimization, we applied the metholodogy to the Perseus Cluster. In addition to creating a map of the cluster indicating

the number of thermal components required to accurately model the thermal emission, we developed a suite of analysis routines to determine the temperatures of the underlying components. Our results are in agreement with over a decade of studies on the Perseus cluster and indicate that multiple temperature components are required for the accurate study of its intracluster medium.

The third paper featured in this thesis once again employs machine learning to solve a previously undetermined question necessary for the accurate characterization of the kinematics of the warm gas in galaxies. We constructed a convolutional neural network to estimate the velocity and broadening parameters from optical spectra of emission-line nebula and applied it to synthetic data replicating real SITELLE observations from the SIGNALS program. With a trained and optimized network in hand, we apply our methodology to a target of the SIGNALS program: the galaxy M33. Our results indicate our algorithm out-performs previous methods and nicely complements spectral fitting procedures. Moreover, the methodology increases calculation speeds by more than an order of magnitude – thus greatly reducing the time needed to determine the kinematic parameters. Although the algorithm was trained for SITELLE data, this method can be readily ported to other IFUs such as MUSE.

I have led two of the papers presented in this memoire and made major contributions to the third. All three papers have been either accepted for publication or have already been submitted and revised once.

Keywords: galaxy clusters – machine learning – HII regions – principal component analysis – convolutional neural network – interstellar medium – intracluster medium – X-ray analysis.

Table des matières

Liste des tableaux

Liste des figures

Liste des sigles et des abréviations

ANN	*Artificial Neural Network*
ACIS	*Advanced CCD Imaging Spectrometer*
AGN	Noyau actif de galaxie, de l'anglais *Active Galactic Nuclei*
BCG	Galaxie dominante d'un amas, de l'anglais *Brightest Cluster Galaxy*
BI	Éclairés à dos, de l'anglais *Back Illuminated*
BLR	Région de raies larges, de l'anglais *Broad Line Region*
CCA	L'analyse de corrélation canonique, de l'anglais *Canonical Correlation Analysis*
CCC	Amas à coeur froid, de l'anglais *Cool Core Cluster*
CCD	Dispositif à transfert de charges, de l'anglais *Charge-Coupled Device*

CF	Fonction de coût, de l'anglais *Cost Function*
CFHT	Télescope Canada-France-Hawaii
CNN	Réseau de neurones convolutif, de l'anglais *Convolutional Neural Network*
CXC	*Chandra X-ray Observatory*
DT	Arbre de décision, de l'anglais *Decision Tree*
FI	Éclairés en front, de l'anglais *Front Illuminated*
ICM	Milieu intra-amas, de l'anglais *Intra-Cluster Medium*
ISCO	Dernière orbite circulaire stable, de l'anglais *Innermost Stable Circular Orbit*
MSE	Moyenne erreur standard, de l'anglais *Mean Standard Error*
NN	Réseau de neurones, de l'anglais *Neural Network*
NCC	Amas sans coeur froid, de l'anglais *non-cool core*
NLR	Région de raies minces, de l'anglais *Narrow Line Region*

ORB	Outil de réduction binoculaire
ORBS	Outil de réduction binoculaire pour SITELLE
ORCS	Outil de réduction de cubes spectraux
RFC	Arbre aléatoire, de l'anglais *Random Forest Classifier*
SIGNALS	*Star-formation, Ionized Gas and Nebular Abundances Legacy Survey*
SITELLE	Spectromètre imageur à transformée de fourier pour l'etude en long et en large de raies d'emission
SMBH	Trou noir supermassif, de l'anglais *Super-Massive Black Hole*
SML	L'apprentissage automatique supervisé, de l'anglais *Supervised Machine Learning*
SVD	Décomposition de valeur singulaire, de l'anglais *Singular Value Decomposition*
UML	L'apprentissage automatique non-supervisé, de l'anglais *Unsupervised Machine Learning*

Remerciements

Je voudrais remercier ma directrice de recherche, Prof Julie Hlavacek-Larrondo, pour son soutien en recherche et dans la vie. Julie me conseille toujours sur n'importe quel sujet sans hésitation. Sa patience a été cruciale dans mes réussites. Merci de toujours me pousser à être un meilleur chercheur. J'ai hâte de continuer le travail avec vous pendant les prochaines quatre années.

Je voudrais remercier tous les membres de notre équipe, passés et présents: Marie-Lou Gendron-Marsolais, Annabelle Richard-Laferrière, Théophile Bégin, et Myriam Prasow-Émond. Vous étiez toujours là pour discuter d'astronomie, de la vie universitaire ou de la vie en général. Je voudrais ajouter un remerciement sincère à Marie-Lou pour tous ses conseils.

Un merci tout particulier pour mon ami, Christian Thibeault. Je ne peux pas compter les heures que nous avons passées à discuter d'astronomie et de la vie. Merci de me supporter dans mon apprentissage de la langue française. Vous êtes un vrai ami.

Merci à Daryl Haggard et à Tracy Webb de McGill University pour toute l'aide avec Sp1049 et les discussions éclairantes.

Merci à Laurie Rousseau-Nepton du CFHT. Votre aide afin de comprendre les complexités de SITELLE était cruciale.

Merci à mes chats, Lemur, Pumpkin, et Luci, de me fournir le soutien émotionnel.

Merci à ma femme, Catherine, pour tout dans la vie.

Chapitre 1

Introduction

L'astronomie a subi une révolution importante dans les années 1920 lorsque Edwin Hubble a établi que certaines étoiles étaient trop loins pour appartenir à notre propre galaxie. Cette affirmation a mené éventuellement à la conclusion que l'univers était beaucoup plus grand qu'on ne le pensait et qu'il était rempli d'une quantité énorme de galaxies, chacune contenant des millions, voir milliards d'étoiles (p. ex. Carroll and Ostlie 2007).

Dans le prochain chapitre, nous discuterons de ces découvertes qui sont les plus fascinantes : les galaxies, ainsi que leur agglomération, les amas de galaxies.

1.1. Galaxies

On peut décrire une galaxie simplement comme un regroupement d'étoiles qui orbitent autour d'un point central. Une galaxie peut contenir entre 10^8 et 10^{14} étoiles. La masse de ces objets varie entre $10^7 M_\odot$ et $10^{12} M_\odot$ (p. ex. Voigt and Fabian 2006). Cependant, la majorité de la masse d'une galaxie est sous la forme de matière sombre (p. ex. Rubin 1983).

Les galaxies sont souvent divisées en deux grandes catégories : *spirales* et *elliptiques*. La figure 1.1 montre les deux types de galaxies. Les galaxies spirales contiennent un grand disque mince en rotation, contenant des bras spiraux très lumineux. Dans ces bras, le taux de formation des étoiles est plus élevé. Les galaxies elliptiques n'ont pas de structure étroite comme les bras des galaxies spirales, mais elles contiennent des étoiles, souvent plus âgées, qui orbitent aléatoirement autour d'un point central. À cause de la rareté des étoiles jeunes, on appelle souvent les galaxies elliptiques *rouges et mortes* (de l'anglais *red and dead*).

Par contre, dans les galaxies plus actives, plusieurs indices de la formation stellaire existent; par exemple, l'étude des régions H II forme la base de la plupart des articles sur la formation stellaire dans les galaxies. Ces régions se forment quand un nuage de

(a) M87 – une galaxie elliptique (b) M83 – une galaxie spirale

Fig. 1.1. Deux exemples qui démontrent la diversité des galaxies. À gauche, dans la galaxie elliptique, il n'y a pas de structure interne apparente. On voit uniquement une agglomération d'étoiles en une structure quasi sphérique. La structure bleue qui s'étend du centre vers la droite est un jet de plasma qui provient de l'AGN central. À droite, dans la galaxie spirale, il existe une structure évidente sous la forme de bras spiraux où il y a beaucoup de formation stellaire (en rose). Source: Hubble Heritage.

gaz est irradié par une étoile à l'intérieur qui est jeune et chaude. Parfois, ces régions contiennent plusieurs étoiles à l'intérieur qui peuvent ioniser le gaz. Malgré le fait que les composantes principales des régions soient l'hydrogène et l'hélium, les nébuleuses de gaz peuvent aussi contenir des métaux. Les spectres typiques des régions H II contiennent plusieurs lignes d'émissions fortes, voir la figure 1.2, comme Hα, Hβ, [O I]λ6300, [O II]λ3727, [O III]λ5007, [N II]λ6548, [N II]λ6583, [S II]λ6717 et [S II]λ6731 (p. ex. Baldwin et al. 1981; Kewley et al. 2006; Oey, Kennicutt 1993; Osterbrock, Ferland 1989). La majorité de l'émission provient de la recombinaison et de la collision entre les électrons libres et les ions/atomes dans le gaz. Pour cette raison, on peut utiliser ces régions pour étudier la dynamique des galaxies et même la structure des champs magnétiques et les effets de turbulence à petite échelle dans une galaxie (p. ex. Osterbrock, Ferland 1989; Kewley et al. 2006).

Afin d'étudier les galaxies elles-mêmes, il faut inspecter leurs spectres et donc comprendre leurs composantes principales. Le spectre d'une galaxie est formé, en partie, par le spectre de millions (ou milliards) d'étoiles qui la composent et pour cette raison, la caractéristique sous-jacente est le spectre d'un corps noir — une matière qui émet dans toutes les longueurs

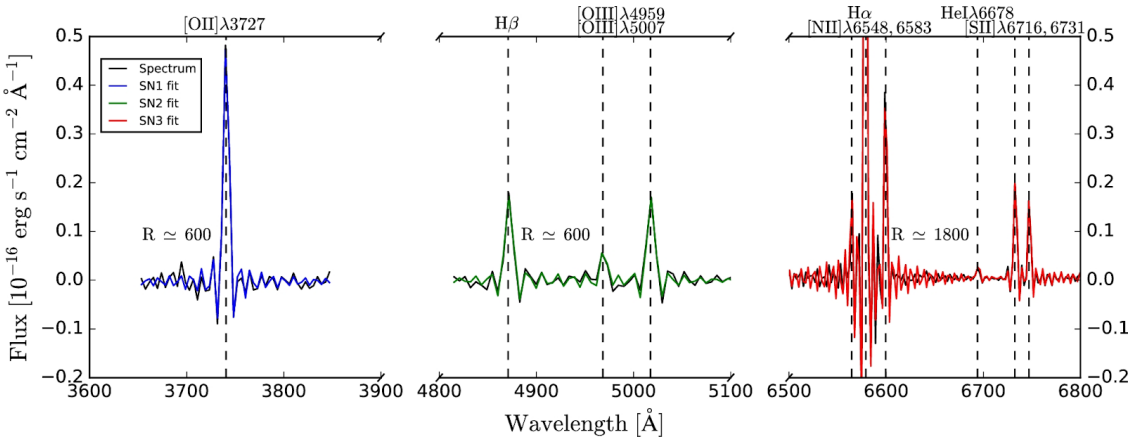

Fig. 1.2. Un spectre typique d'une région H II pris par SITELLE (voir §1.6.2 pour les détails concernant SITELLE). Dans ce spectre, on voit les lignes d'émission fortes Hα, Hβ, [O II]λ3727, [O III]λ4959, [O III]λ5007, [N II]λ6548, [N II]λ6583, [He I]λ6678, [S II]λ6717 et [S II]λ6731. Source : Rousseau-Nepton et al. (2019)

d'onde. En utilisant la loi de Planck, on peut décrire un spectre mathématiquement :

$$B(\lambda, T) = \frac{2hc^2}{\lambda^5} \frac{1}{\exp \frac{hc}{\lambda k_B T} - 1} \tag{1.1.1}$$

où λ est la longueur d'onde, T est la température, h est la constante de Planck ($6{,}626 \times 10^{-34}$ J s), c est la vitesse de la lumière ($2{,}99792 \times 10^{8}$ m s^{-1}) et k_B est la constante de Boltzmann ($1{,}38 \times 10^{-23}$ J K^{-1}). La longueur d'onde où l'émission est maximale est décrite par la loi de Wein : $\lambda_{max} T = b$, où $b \approx 2.897 \times 10^{-3}$ m K. Deux autres caractéristiques les plus communes sont les raies d'absorption, qui proviennent d'un objet froid qui absorbe des photons à des longueurs d'onde spécifiques, et les raies d'émission, qui proviennent d'un objet chaud ou excité qui émet des photons à cette longueur d'onde.

Bien que l'étude des galaxies soit très compliquée et fascinante en elle-même, ce mémoire porte aussi sur les amas de galaxies.

1.2. Amas de galaxies

Formés par l'effondrement gravitationnel, les amas de galaxies sont considérés comme les structures les plus grandes dans l'univers. Ils sont gouvernés par le théorème du viriel qui stipule que l'énergie gravitationnelle, U, et l'énergie cinétique, K, sont associées par l'équation suivante :

$$2\langle K \rangle = -\langle U \rangle \tag{1.2.1}$$

Dans le cas d'un amas de galaxies :

$$\frac{1}{2} \mu m_H \sigma^2 = \frac{3 k_B T}{2} \tag{1.2.2}$$

où μ est la masse moléculaire moyenne, m_H est la masse de l'atome d'hydrogène, σ est la dispersion de la vitesse des galaxies dans l'amas et T est la température du gaz (p. ex. Binney and Tremaine 1987). À cause de ce puits gravitationnel, les amas de galaxies contiennent une quantité énorme d'énergie. Ainsi, cette énergie se manifeste sous la forme d'émission électromagnétique ou de luminosité.

Bien que les quasars soient les sources rayons X les plus lumineuses dans l'univers, les amas de galaxies ne sont pas très loin derrière avec une luminosité rayons X située entre 10^{43} et 10^{46} erg s^{-1} (p. ex. Maughan 2012; Donahue et al. 2006). En moyenne, le diamètre d'un amas de galaxies varie entre 2 et 10 Megaparsecs, Mpc[1]. Souvent, il existe une galaxie elliptique extrêmement grande et lumineuse au centre d'un amas de galaxies appelée la galaxie dominante d'un amas (BCG, de l'anglais *Brightest Cluster Galaxy*). Le rayon moyen des BCGs est environ 30 kpc, tandis que la masse est entre 10^{11} et $10^{12} M_\odot$ (p. ex. Dubinski 1998; De Lucia and Blaizot 2007). Selon Matthews et al. (1964), un pourcentage non négligeable de toutes les BCGs est considéré comme cD, c'est-a-dire des galaxies elliptiques ayant un halo stellaire considérable; on pense qu'elles sont formées par la fusion consécutive de galaxies avec la BCG. Ce fait indique l'importance et la fréquence des fusions galactiques au centre de l'amas de galaxies.

1.3. Milieu intra-amas

En raison de de leurs caractéristiques, les amas ont des masses de l'ordre de 10^{14} à $10^{15} M_\odot$, quoique la majorité de la masse, soit 84%, est sous la forme de la matière sombre (comparable à une galaxie individuelle). La partie qui reste vient du milieu intra-amas (ICM, de l'anglais *Intra-Cluster Medium*), soit 13%, et des galaxies individuelles, soit 3% (p. ex. Mohr et al. 1999; Nagai et al. 2007). L'ICM est constitué de gaz et de poussière qui peuplent la région entre les galaxies individuelles dans les limites de l'amas. On considère souvent l'ICM comme une substance qui est en équilibre hydrostatique puisque le temps de propagation du son est considérablement moindre que l'âge de l'amas. En utilisant cette supposition et l'équation d'équilibre hydrostatique (équation 1.3.1), on peut calculer la masse approximative de l'amas.

$$\frac{1}{\rho}\frac{dP}{dR} = -\frac{GM(< R)}{R^2} \tag{1.3.1}$$

où M est la masse de l'amas, G est la constante gravitationnelle ($6{,}674 \times 10^{-11}$ m^3 kg^{-1} s^{-1}) et R est le rayon de l'amas. On peut obtenir la pression du gaz, P, et la densité du gaz, ρ, en effectuant des mesures en spectroscopie rayons X. Selon McNamara, Nulsen (2012), les estimations de la masse sont en accord avec les autres mesures (ex. via les lentilles

[1]Un parsec est la distance à laquelle le rayon de la Terre sous-tend un angle d'une seconde d'arc; par exemple, la distance entre le Soleil et la Terre est 5×10^{-6} parsec (ou 1 unité astronomique, AU).

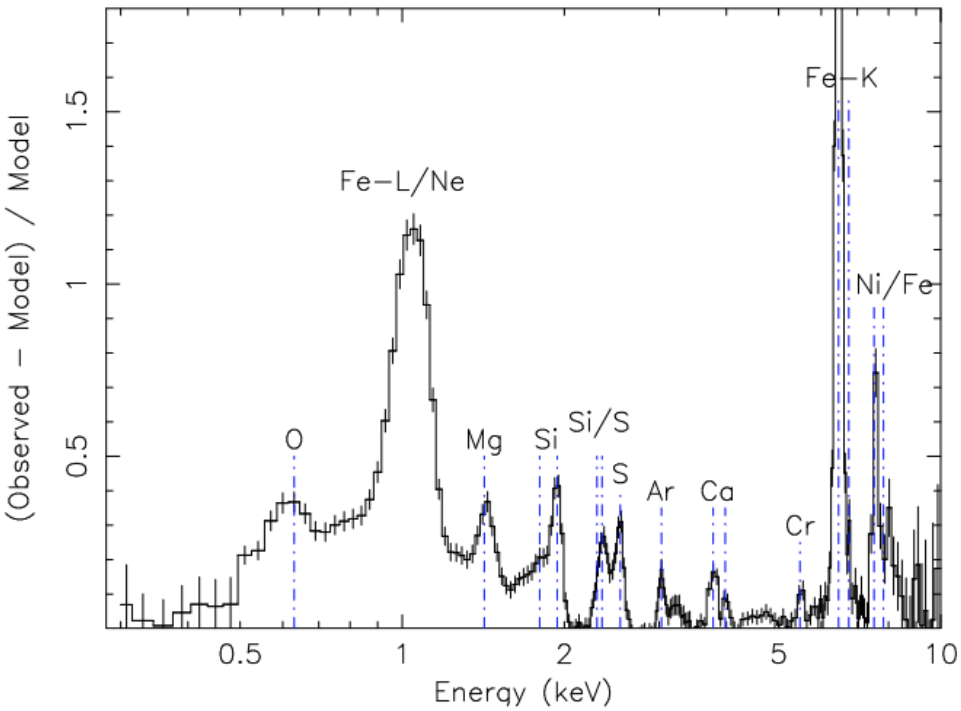

Fig. 1.3. Spectre rayons X de l'amas 2A 0335+096 pris par le télescope spatial XMM-Newton. Dans cette figure, nous voyons les raies d'émission, notées par un trait bleu vertical, qui contribuent significativement à l'émission totale d'un amas. Source : Boehringer and Werner (2009)

gravitationnelles) jusqu'à plusieurs dizaines de pourcentages.

Tandis que la majorité de la luminosité de l'ICM est expliquée théoriquement par l'effondrement gravitationnel, il reste une partie qui n'est pas expliquée par l'effondrement; il faut donc qu'un autre mécanisme existe pour jouer un rôle central dans l'injection d'énergie dans l'ICM – celui-ci est décrit à la section 1.4.2. L'ICM est principalement composé d'hydrogène (71%), d'hélium (28%) et d'autres éléments lourds (1%; p. ex. Tozzi, Norman 2001). En raison de la haute température ($10^7 - 10^8$ K), l'hydrogène et l'hélium sont ionisés, alors que les éléments lourds retiennent certains de leurs électrons. La densité de l'ICM est relativement basse, soit d'environ 10^{-3} particules par centimètre cube (Peterson, Fabian 2006). Le plasma ionisé de l'ICM émet dans les rayons X à cause du Bremsstrahlung thermique – la radiation électromagnétique produite par le ralentissement d'une particule chargée par une autre particule chargée (Lea et al. 1973). On croit que la majorité de cette radiation s'échappe sans qu'elle n'interagisse avec les autres particules parce que la densité est très basse (donc l'ICM est considéré comme optiquement mince). Plusieurs raies d'émission sont aussi présentes dans les rayons X (p. ex. Fabian 1994); les raies proviennent souvent des éléments lourds comme Fe, Si et Mg (voir figure 1.3).

1.3.1. Courant de refroidissement et amas à coeur froid

On peut observer les effets de rétroaction dans les BCGs qui se trouvent dans un amas de galaxies à coeur froid (CCC, de l'anglais *Cool Core Cluster*). On classifie un amas comme un CCC lorsque la majorité de l'émission rayons X provient de son centre géométrique. Mais, si ceci n'est pas observé, alors on le considère comme un amas sans coeur froid (NCC, de l'anglais *Non Cool Core Cluster*; voir figure 1.4).

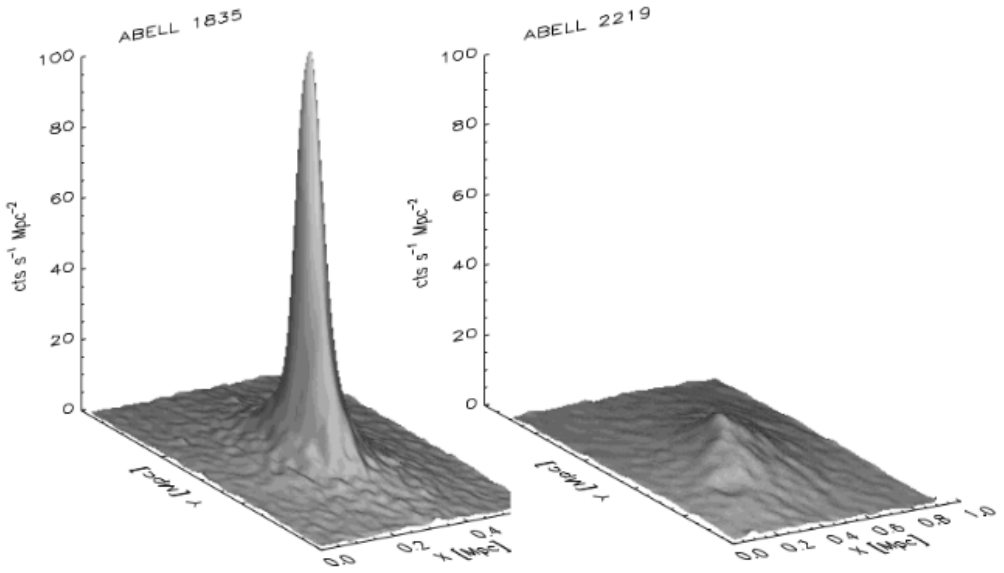

Fig. 1.4. À gauche, un amas à coeur froid est facilement reconnaissable par son pic d'émission; à droite, un amas sans coeur froid où l'on note la paucité d'émission centrale. L'image est prise dans les rayons X. Cette distinction dans le profil de l'émission est typique pour distinguer entre les deux catégories d'amas. Source : Hlavacek-Larrondo et al. (2012)

Selon Hudson et al. (2010), les CCCs ont un temps de refroidissement plus court que le temps de Hubble. En effet, le plasma ICM commence à refroidir en raison de la forte émission rayons X; une conséquence de ceci est que la densité de l'ICM près du centre de l'amas s'accroît tandis que l'ICM refroidit. Puisque l'émission rayons X augmente proportionnellement avec le carré de la densité du plasma, le temps de refroidissement diminue davantage (p. ex. Fabian et al. 2003). Un courant de refroidissement se forme quand le gaz perd assez d'énergie ; il ne peut donc plus supporter les couches d'ICM les plus loin du centre. Ce courant de refroidissement continue et éventuellement, des nuages moléculaires froids se forment et se condensent au centre de l'amas. On s'attendrait donc à voir une panoplie de nouvelles étoiles au centre des amas de type CCC. Toutefois, selon Peterson, Fabian (2006), les astronomes n'observent pas de taux de formation stellaire (SFR,

de l'anglais *Stellar Formation Rates*) aussi haut que le modèle le prévoit : $100-1000 M_{\odot}/\mathrm{yr}$ prédit versus $10-300 M_{\odot}$ observé (p. ex. McDonald et al. 2015). Il y a plusieurs explications possibles pour ce désaccord : l'efficacité de la formation stellaire, la rétroaction des AGNs, les effets d'une fusion mineure de galaxies (p. ex. McDonald et al. 2015; Hlavacek-Larrondo et al. 2012). Cependant, la méthode la plus proéminente est celle de la rétroaction des noyaux actifs de galaxie (AGN, de l'anglais *Active Galactic Nuclei*); selon Yang and Reynolds (2016), les bulles et les chocs faibles se développent à cause de jets provenant des AGNs et ils interagissent avec l'ICM pour le réchauffer et empêcher la formation stellaire.

Il y a plusieurs méthodes utilisées pour déterminer si un amas doit être classifié comme CCC ou NCC. Après avoir observé un maximum dans les rayons X au centre de l'amas, le temps de refroidissement permet de confirmer s'il s'agit d'un CCC. Ce temps peut être calculé via l'équation suivante :

$$t_{\mathrm{cool}} = \frac{5}{2} \frac{1.9\, n_{\mathrm{e}}\, kT\, V}{L_{\mathrm{X}}}, \tag{1.3.2}$$

où n_{e} est la densité électronique du gaz, kT est la température du gaz, V est le volume de gaz dans une région pré-spécifiée et L_{X} est la luminosité de gaz en rayons X. Si le temps de refroidissement est plus petit que 3 Gyr, on considère l'amas comme étant un CCC. Une autre caractéristique commune est l'entropie de l'amas (voir la figure 1.5; Sanderson et al. 2009) :

$$S = \frac{kT}{\rho^{\frac{2}{3}}} \tag{1.3.3}$$

où ρ est la densité du gaz. Selon Cavagnolo et al. (2008), si la valeur de l'entropie tombe en dessous de 30 keV, l'amas est considéré comme un CCC. On calcule les caractéristiques en utilisant les observations rayons X des amas de galaxies.

1.4. Noyau actif de galaxie

Au centre de toutes les galaxies massives, il existe un monstre : un trou noir supermassif (SMBH, de l'anglais *Supermassive Black Hole*). S'il accrète une quantité significative de masse, alors on réfère plutôt à un AGN. Pour être plus précis, l'AGN comporte un disque d'accrétion qui entoure le SMBH. Ce disque d'accrétion est responsable de la luminosité extrême que l'on observe chez les AGNs (p. ex. Zackrisson 2005; Carroll and Ostlie 2007). Tel qu'illustré dans la figure 1.6, il y a plusieurs structures qui entourent le disque d'accrétion dont nous allons discuter plus tard. Le disque lui-même est formé de gaz et de poussière qui sont attirés vers le trou noir central à cause de l'interaction gravitationnelle. Le gaz et la poussière dans le disque tournent et interagissent. Pendant les collisions, en raison de la viscosité du milieu, les particules perdent leur moment angulaire et leur énergie.

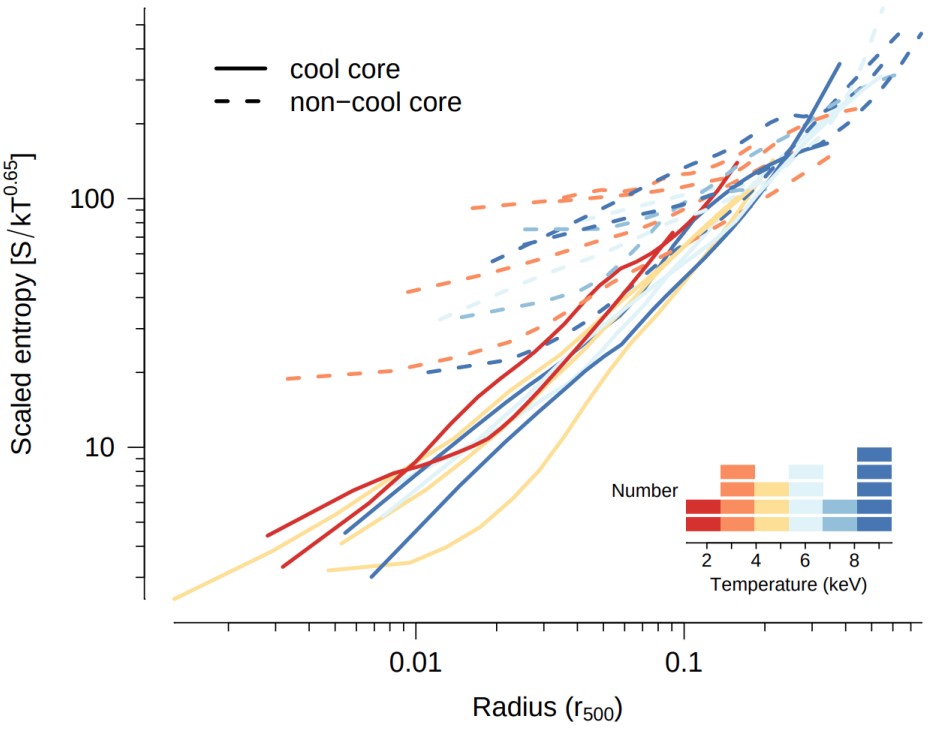

Fig. 1.5. L'entropie en fonction du rayon pour un échantillon d'amas de galaxies. Les amas de type CCC ont une entropie centrale nettement plus petite que les amas de type NCC. Source: Sanderson et al. 2009

Au moment où les particules perdent leur moment angulaire, elles tombent vers le centre du disque. L'énergie gravitationnelle des particules est transformée sous forme d'énergie thermique qui se traduit par l'émission (p. ex. Abramowicz and Fragile 2013; White and Holt 1982). La température du disque devient plus grande plus près du centre et à cause de cette différence, le disque émet des photons dans plusieurs longueurs d'onde.

Le disque du trou noir s'étend jusqu'à une position qui s'appelle la dernière orbite circulaire stable (ISCO de l'anglais *Innermost Stable Circular Orbit*). La valeur de l'ISCO dépend de la rotation et de la masse du trou noir via l'équation du rayon de Schwarzschild (Schwarzschild 1916):

$$r_{isco} = 3R_s = 3\frac{2GM_{BH}}{c^2} \tag{1.4.1}$$

où R_s est le rayon de Schwarzschild et M_{BH} est la masse du trou noir.

1.4.1. Jets

En utilisant les radiotélescopes, on observe que les AGNs produisent souvent des structures étendues, appelées jets (voir la figure 1.7). On est d'avis que les jets jouent un rôle

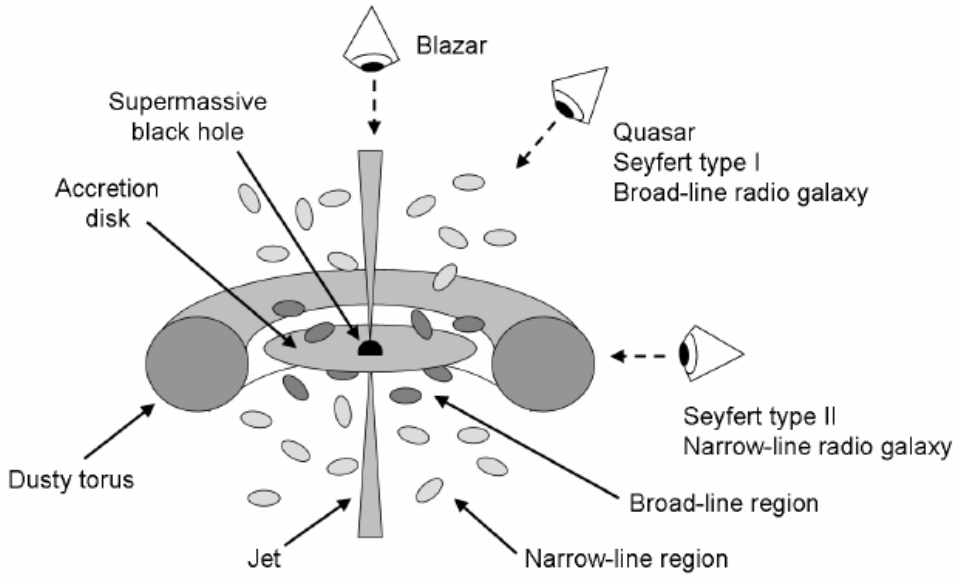

Fig. 1.6. Schéma représentant les structures autour d'un trou noir actif. On peut voir qu'il y a plusieurs sources différentes d'émission et d'absorption dans la région voisine. Selon la théorie d'unification des AGNs, les différentes catégories d'AGN seraient dues uniquement à des effets de projection. Source: Zackrisson (2005).

important dans l'évolution des galaxies. On croit que la collimation et l'évolution des jets sont formées par le disque d'accrétion qui contient un champ magnétique puissant d'environ 10^4 G (p. ex. O'Sullivan and Gabuzda 2009); peut-être que le champ magnétique est emballé autour du disque d'accrétion ou même dans le trou noir lui-même. Les jets sont souvent visibles en radio puisqu'ils sont composés de particules relativistes qui émettent de la radiation. À cause de l'émission synchrotron (Sokolov and Ternov 1966).

Il y a trois façons connues pour produire les jets : la première est purement hydrodynamique, la deuxième inclut les champs magnétiques et finalement, la troisième inclut la rotation du disque (Pino 2005). Introduit pendant les années 1970, le modèle à double échappement explique la formation des jets en utilisant uniquement l'hydrodynamique (Blandford and Rees 1974). Dans ce processus, on présume qu'une source de plasma est générée par le disque d'accrétion qui va alimenter les jets. Le plasma chaud est dans une région d'un gaz plus froid qui crée une pression sur le plasma chaud. Selon le modèle à double échappement, le gaz froid est en rotation et c'est en raison de cette dernière que les jets seront lancés dans la direction de l'axe de rotation. Selon l'équation de Bernoulli, si un jet apparaît, il faut qu'un autre jet apparaisse. Malgré le fait que ce processus décrive bien une façon de créer des jets, il néglige les champs magnétiques associés avec ceux-ci.

Le modèle magnétocentrifuge par Blandford and Payne (1982) considère les effets d'un champ magnétique sur la création des jets. Le modèle de Blandford-Payne constate qu'il existe un champ magnétique ayant des lignes de champ figées dans le disque. En raison de la rotation du disque, les lignes de champ vont s'emmêler, ce qui cause plus de stress magnétique. Si nous prenons une pièce du disque avec une masse, M, à une distance du centre, r_0, nous pouvons calculer la vitesse (képlérienne) de cette pièce comme (Choudhuri and Choudhuri 1998):

$$\Omega_0 = \sqrt{\frac{GM}{r_0^3}} \tag{1.4.2}$$

À ce point, il y a deux forces : la force centrifuge, $F_c = \Omega_0 r^2$, où r est la distance et la force gravitationnelle. Nous pouvons calculer la force totale sur une portion de matière étant à une distance au-dessus du disque, z, en calculant le potentiel à ce point. Ainsi, nous utilisons l'équation suivante qui associe la force et un potentiel (ϕ) :

$$\mathbf{F} = -\nabla\phi = -\frac{d\phi}{ds}\hat{s} \tag{1.4.3}$$

où $\hat{s}$ est le vecteur qui pointe dans la direction de r. Le potentiel est

$$\phi = \phi_c + \phi_G = -\frac{1}{2}\Omega_0^2 r^2 - \frac{GM}{\sqrt{r^2+z^2}} \tag{1.4.4}$$

Si nous réécrivons l'équation en utilisant l'équation 1.4.1 et en utilisant le fait que $r = r_0 + r'$ où r' est le déplacement et que $|r'| < |r_0|$, on a :

$$\phi = \frac{-GM}{r_0}\left[\frac{3}{2} + \frac{3}{2}\left(\frac{r'}{r_0}\right)^2 - \frac{1}{2}\left(\frac{z}{r_0}\right)^2\right] \tag{1.4.5}$$

À partir de cela, nous pouvons exprimer nos variables en fonction de l'angle α, l'angle entre la portion de matière et le disque le long d'une ligne de champ magnétique, et s, la distance entre la pièce de matière et le disque le long de la ligne de champ magnétique : $r' = s\cos(\alpha)$ et $z = s\sin(\alpha)$. Donc,

$$\phi = \frac{-GM}{r_0}\left[\frac{3}{2} + \frac{3}{2}\left(\frac{s\cos(\alpha)}{r_0}\right)^2 - \frac{1}{2}\left(\frac{s\sin(\alpha)}{r_0}\right)^2\right] \tag{1.4.6}$$

En utilisant l'équation 1.4.1, nous avons que

$$\mathbf{F} = \frac{GM}{r_0^3}[3\cos^2(\alpha) - 2\sin^2(\alpha)]\hat{s} \tag{1.4.7}$$

Cette dérivation démontre que la force ressentie par une pièce de plasma va éjecter le plasma du disque si l'angle entre le disque et la ligne magnétique, α, est plus petit que 60 degrés. Dès que le plasma est éjecté, les champs magnétiques emmêlés vont le collimater.

Il existe un troisième mécanisme permettant d'éjecter le plasma en forme d'un jet qui s'appelle le modèle de Blandford-Znajek (Blandford and Znajek 1977). Le processus de Blandford-Znajek ressemble fortement à celui de Blandford-Payne, mais ce processus constate que le puissant champ magnétique accumule l'énergie du moment angulaire intrinsèque du trou noir.

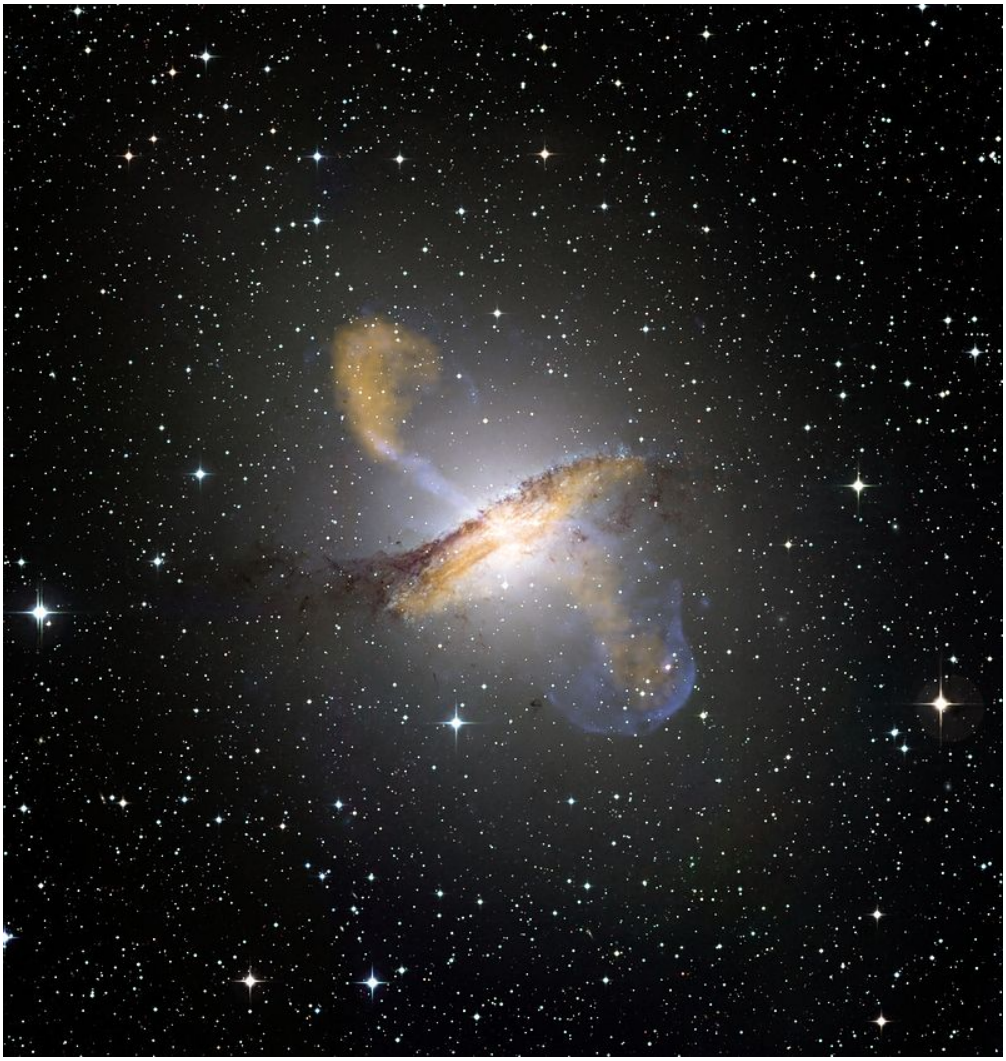

Fig. 1.7. Image qui met en évidence les jets puissants et étendus de Centaurus A. Les jets entraînent du matériau du centre et sont créés par l'AGN. Source: *NASA/IPAC Extragalactic Database*

1.4.2. Mécanismes de rétroaction

La rétroaction est l'interaction entre le gaz de la galaxie hôte et l'énergie (souvent en forme de radiation, vents, ou jets) de l'AGN central. Dans le cas d'un amas de galaxies, la rétroaction est l'interaction entre l'ICM et l'AGN au centre de la BCG. La rétroaction

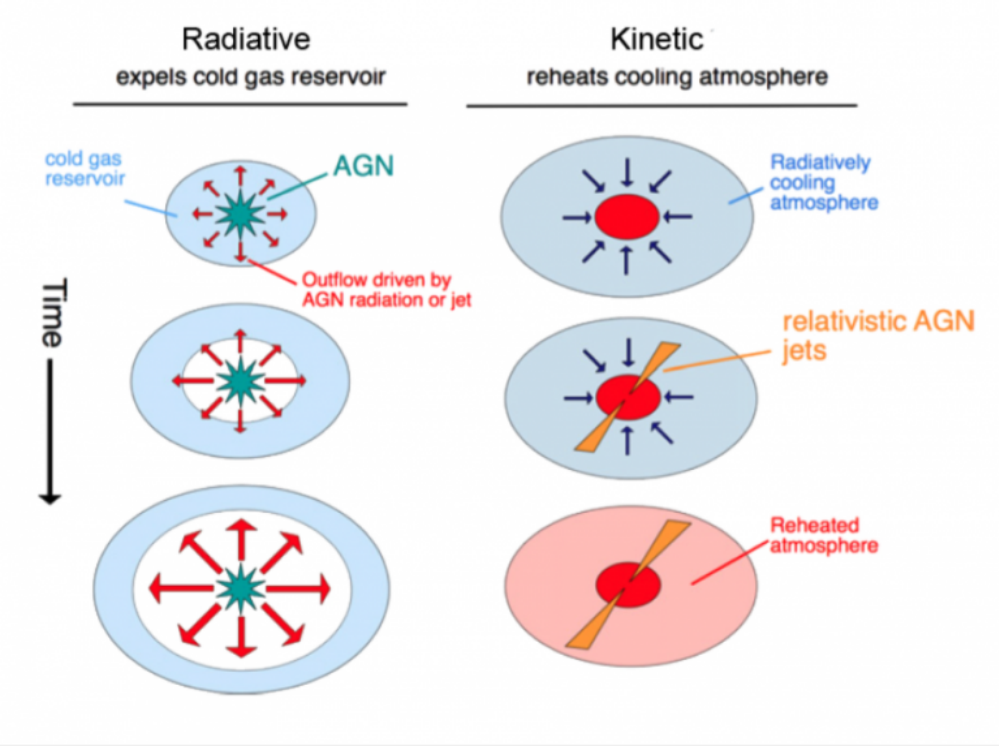

Fig. 1.8. Un graphique qui démontre deux types de rétroaction: cinétique et radiative. Source : Astrobites

dépend du taux d'accrétion de l'AGN. Nous utilisons le ratio d'Eddington pour décrire le taux d'accrétion :

$$\eta = \frac{L_{AGN}}{L_{Edd}} \tag{1.4.8}$$

où L_{AGN} est la luminosité bolométrique de l'AGN et L_{Edd} est la luminosité d'Eddingtion qui est décrite par l'équation suivante :

$$L_{Edd} = \frac{4\pi GMcm_p}{\sigma_T} \tag{1.4.9}$$

où M est la masse du SMBH, m_p est la masse d'un proton et σ_T est la section efficace de la diffusion de Thompson (Carroll and Ostlie 2007). L_{Edd} est la luminosité maximale d'un AGN. On catégorise deux genres de rétroaction à partir de la valeur : si η est plus petit que 0.01, on a le mode cinétique, tandis que si η est plus grand que 0.01, on a le mode radiatif (p. ex. Fabian 2009). La figure 1.8 met en évidence les deux types de rétroaction.

1.4.2.1. *Mode radiatif*

Le mode radiatif ou le mode quasar se présentent si l'AGN accrète du gaz à haut taux, c'est-à-dire que $L_{AGN} > 0.01 L_{Edd}$ (Wandel 1991). Pendant ce mode, la majorité de l'énergie injectée dans l'ICM est sous la forme de radiation et de vents (Gallagher and Everett 2007; Churazov et al. 2005). Les SMBH les plus actifs sont définis comme des quasars et leur

luminosité atteint presque la luminosité d'Eddington (Hopkins and Elvis 2010). Les quasars aussi manifestent les régions de raies larges (BLR, de l'anglais *broad line regions*); on croit que les BLRs sont le résultat de puissants vents radiatifs accélérés par le rayonnement du disque d'accrétion (Kaspi et al. 2005; Hamann et al. 2013). Par la présence de vents, le mode radiatif est très important pour l'évolution de la galaxie hôte. Selon Fabian et al. (2011), les vents des quasars atteignent parfois $5 - 10\%$ du pourcentage d'accrétion suffisant pour expulser le gaz de la galaxie hôte. Les AGNs ont aussi des régions de raies étroites (NRL, de l'anglais *narrow line regions*), qui ont une densité basse, mais une température haute (Cohen 1983; Bennert et al. 2002).

1.4.2.2. *Mode cinétique*

Le mode cinétique se développe lorsque le taux d'accrétion diminue au-dessous de 1% du taux d'Eddington. À ce moment-là, l'AGN peut créer les jets (les mécanismes sont décrits dans §1.4.1) qui réchauffent le gaz (p. ex. Fabian 2009; Gan et al. 2014). On peut décrire la rétroaction avec trois processus principaux : la création de puissants jets, la formation des bulles de plasma relativistes autour de l'AGN et ensuite la propagation des bulles.

Comme vu précédemment, les jets existent souvent dans les CCCs et proviennent de l'AGN dans la BCG; les jets créent des bulles dans l'ICM en déplaçant le gaz chaud – voir la figure 1.9. La figure 1.10 montre la relation entre le pouvoir des jets et la luminosité en rayons X des bulles. Les bulles, qui sont vues comme des cavités dans l'ICM en rayons X, ne contiennent pas autant de gaz que le reste du centre de l'amas – voir figure 1.9 (p. ex. Birzan et al. 2004; McNamara et al. 2005). Les bulles les plus proches de l'AGN sont entourées par des régions de haute pression. Il existe souvent une région de choc à la frontière des bulles (McNamara et al. 2005).

Selon McNamara, Nulsen (2012), les bulles ont un diamètre d'environ une douzaine de kpc. Il qualifie l'enthalpie des bulles comme :

$$H = \frac{\gamma_1}{\gamma_1 - 1} pV \tag{1.4.10}$$

où γ_1 représente la capacité thermique des bulles (c.-à-d. dans le cas de particules relativistes $\gamma_1 = 4/3$), p est la pression et V est le volume des bulles. L'enthalpie est importante parce que si on la connaît, on peut calculer l'énergie des bulles et donc l'énergie qui est injectée par les jets qui proviennent de l'AGN. Pour calculer la puissance qui est injectée à la galaxie hôte, on doit simplement diviser l'énergie par l'âge de la bulle. Il y a trois estimations pour l'âge d'une bulle selon Rafferty et al. (2006) et Birzan et al. (2004) : le temps de flottaison (t_{flot}), le temps de remplissage (t_{remp}) et le temps de la traversée (t_{c_s}). On calcule ces quantités de

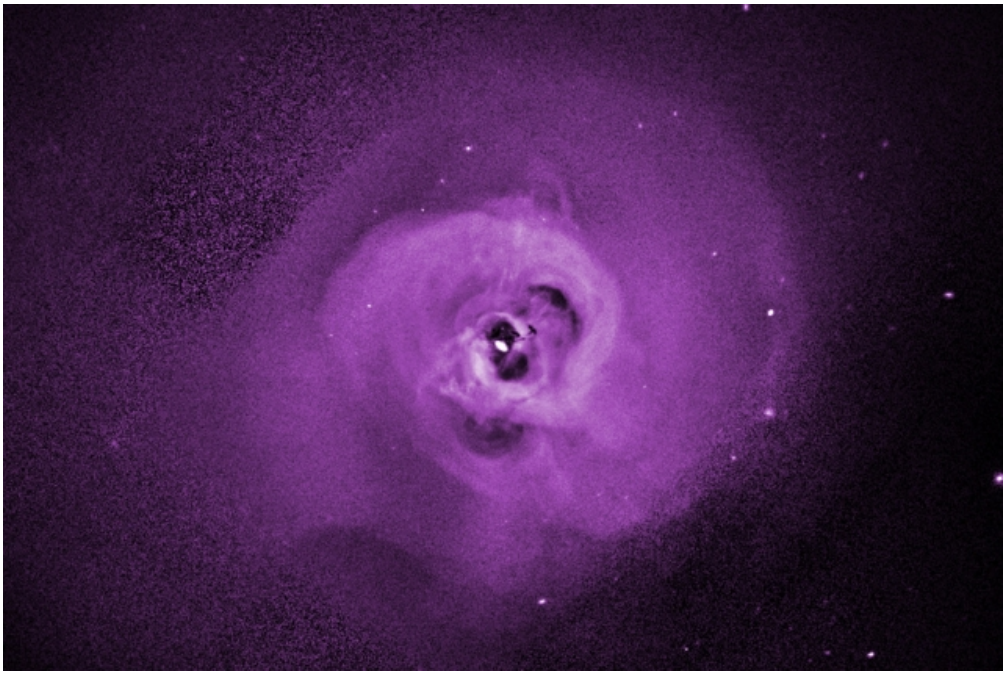

Fig. 1.9. Image en rayons X de l'amas de galaxies de Persée. On peut observer les cavités, ce qui signifie que le mode cinétique est actif. Les astronomes étudient ces bulles pour comprendre la relation entre les jets qui proviennent de l'AGN et l'ICM. Source: NASA/CXC/Stanford/I.Zhuravleva, et al.

la façon suivante :

$$t_{flot} = \frac{R}{v_t} \sim R\sqrt{\frac{SC}{2gV}} \tag{1.4.11}$$

$$t_{remp} = 2\sqrt{\frac{r}{g}} \tag{1.4.12}$$

$$t_{c_s} = \frac{R}{c_s} = R\sqrt{\frac{\mu m_H}{\gamma kT}} \tag{1.4.13}$$

où R est la distance entre l'AGN et la bulle, $v_t = \sqrt{\frac{2gV}{SC}}$ est la vitesse terminale, g est l'accélération gravitationnelle, S est l'entropie, C est le coefficient de traînée, r est le rayon de la bulle, $c_s = \sqrt{\frac{\gamma kT}{\mu m_H}}$ est la vitesse du son, kT est la température du plasma, μ est la masse par particule dans la bulle (≈ 0.61), γ est le ratio des chaleurs spécifiques (dans le cas de plasma relativiste $\gamma_1 = 4/3$) et m_H est la masse de l'hydrogène – le constituant principal. Bien que les trois équations donnent trois temps différents, ils sont assez similaires ; on peut donc utiliser n'importe lequel d'entre eux (McNamara and Nulsen 2007). Les estimations de la puissance indiquent que les bulles créées par l'AGN injectent une quantité d'énergie considérable (voir la figure 1.10; Birzan et al. 2004). Par conséquent, les bulles contrebalancent le refroidissement radiatif de l'ICM et peuvent expliquer le manque de formation d'étoiles (p. ex. Fabian 1994).

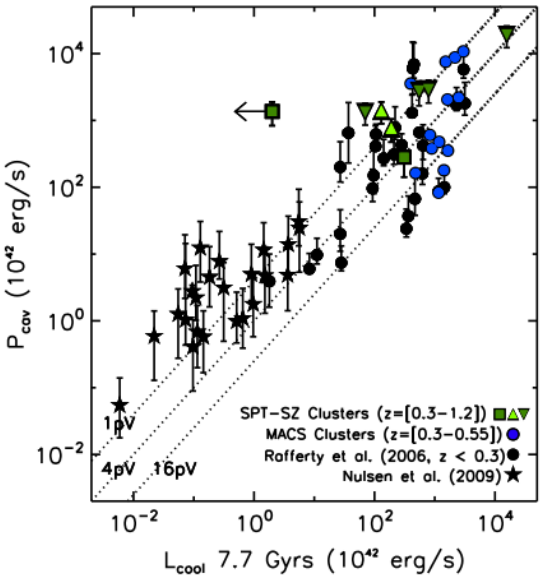

Fig. 1.10. Graphique mettant en évidence la relation entre la luminosité en rayons X et la puissance d'une cavité. Malgré la dispersion, cette figure démontre qu'il existe une relation étroite entre les deux paramètres. Source: Hlavacek-Larrondo et al. (2015)

1.5. Apprentissage automatique

Depuis quelques dizaines d'années, les méthodes d'apprentissage automatique ont été employées en astronomie observationnelle. L'apprentissage automatique est un amalgame de méthodes qui nous aide à apprendre plus de nos données et sont souvent utilisées pour explorer un espace de paramètres précédemment inexploré (p. ex. Baron 2019). Récemment, la communauté astronomique l'a utilisé pour étudier les spectres galactiques, extragalactiques et stellaires (McGurk et al. 2010; Pace et al. 2019; Ronen et al. 1999), calculer la masse dynamique d'amas de galaxies (Ntampaka et al. 2016; Ntampaka et al. 2019) et explorer les ensembles de données massives (Ball and Brunner 2010; Castro-Ginard et al. 2018). Il existe plusieurs techniques qui appartiennent à la famille des algorithmes connue comme l'apprentissage automatique : nous allons explorer l'analyse de composantes principales (PCA, de l'anglais *Principal Component Analysis*), les arbres de décision (DT, de l'anglais *Decision Tree*), le classificateur des forêts aléatoires (RFC, de l'anglais Random Forest Classifier) et les réseaux des neurones (NN, de l'anglais *Neural Network*). Dans les deux derniers articles de ce mémoire, nous allons investiguer l'utilisation de ces techniques en astronomie observationnelle.

1.5.1. Analyse en composantes principales

L'analyse en composantes principales est une technique qui combine l'apprentissage automatique et les statistiques classiques. Cette méthode trouve la relation complexe entre

les variables et leurs composantes les plus fondamentales selon Jolliffe, Cadima (2016). Pour être plus précis, PCA représente une rotation des données en une base nouvelle et orthonormale dans laquelle la première coordonnée contient la projection de données qui maximise la variance (la première composante principale), la deuxième coordonnée contient le deuxième ordre de variance (la deuxième composante principale) et ainsi de suite. Cette technique revient a calculer les valeurs/vecteurs propres, ce qui est répandu en techniques statistiques multivariables comme la décomposition de valeur singulière (SVD, de l'anglais *Singular Value Decomposition*) et l'analyse de corrélation canonique (CCA, de l'anglais *Canonical Correlation Analysis*). PCA a été utilisée plusieurs fois en astronomie observationnelle et sert souvent à améliorer les algorithmes de classification. Nombreux auteurs l'ont appliquée aux spectres galactiques et stellaires (p. ex. Ronen et al. 1999; McGurk et al. 2010; Pace et al. 2019).

Avant d'explorer l'usage de PCA sur l'ICM, nous allons décrire le processus standard de PCA selon Murtagh, Heck (1987). En termes plus mathématiques, cette technique est une transformation orthogonale qui crée une base orthogonale de composantes principales qui sont utilisées pour projeter les nouvelles données dans l'espace vectoriel des composantes elles-mêmes. Dans le contexte de notre travail, chaque composante primaire représente un mélange de paramètres de l'émission (la température, l'abondance de métaux, la densité de colonne, le décalage vers le rouge, etc.).

1.5.2. Arbres de décision et classificateur des arbres aléatoires

Un autre algorithme de l'apprentissage automatique bien connu et fortement utilisé est l'arbre de décision (voir la figure 1.11 pour un exemple simple). Ce groupe d'algorithmes forme une classe des méthodes qui sont souvent utilisées pour les tâches de classification. Par exemple, les données sont introduites dans l'algorithme qui va les classifier en un groupe de sortie. Les paramètres de cet algorithme sont appris pendant un processus d'entraînement (*training* en anglais). Durant ce processus, l'algorithme montre l'entrée et la bonne classification; cela forme un groupe de modèles connu comme étant un apprentissage supervisé (SML, de l'anglais *Supervised Machine Learning*). Pendant que l'algorithme s'entraîne, il optimise les paramètres en minimisant une fonction de coût (FC, de l'anglais *cost function*) entre la sortie et la bonne classification.

Explorons maintenant le processus d'entraînement pour l'algorithme de l'arbre de décision. D'abord, l'algorithme doit déterminer la meilleure façon de distribuer le noeud de base en sous-noeuds. En général, nous employons un algorithme gourmand (en anglais *greedy algorithm*) qui calcule récursivement le coût d'une division associé avec un attribut

dans les données (p. ex. Baron 2019; Quinlan 1986; Tan et al. 2005). Quand l'algorithme trouve la meilleure division, il crée une branche qui représente cet attribut. L'algorithme essaie de regrouper les données à chaque étape en deux groupes homogènes. De cette façon, l'arbre de décision détermine une liste de tranches des attributs pour classifier les données.

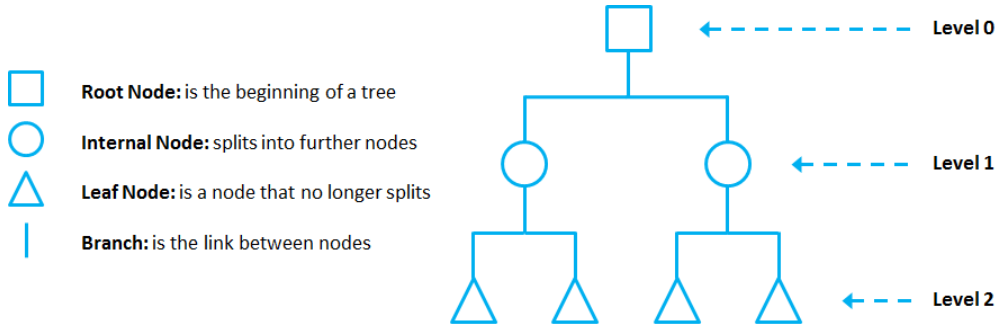

Fig. 1.11. Un exemple simple d'un arbre de décision avec trois étapes. On voit les relations entre les trois types de noeuds : noeud de base, noeud interne et noeud de feuille. Source : TowardsDataScience

Malgré le fait que les arbres de décision soient capables de bien classifier des données complexes, si l'arbre devient lui-même trop grand ou compliqué, il va introduire un biais de surajustement (en anglais *over-fitting*). Ce processus signifie que l'algorithme ajuste les données parfaitement; cependant, cela signifie en plus qu'il ne va pas réussir à ajuster de nouvelles données. Il y a plusieurs façons d'éviter ce problème: nous utilisons l'élagage (en anglais *prunning*) et le classificateur des arbres aléatoires. Pendant l'élagage, les divisions de moindre importance sont rejetées pour rendre l'arbre plus simple et donc moins prédisposé au surajustement.

Le RFC consiste en plusieurs arbres de décision et agit sur eux comme un ensemble. La figure 1.12 montre un arbre aléatoire simple. Chaque arbre va classifier les données individuellement et puis le RFC va prendre la valeur la plus fréquente. Cette technique utilise le fait que les arbres ne sont pas corrélés les uns avec les autres : Ainsi, même si un arbre est incorrect, ce résultat n'affecte pas les autres arbres (p. ex. Breiman 2001; Breiman 1996; Breiman et al. 1984). De plus, les erreurs de chaque arbre ne sont pas partagées entre eux.

1.5.3. Réseau de neurones artificiel et convolutif

Un réseau de neurones artificiel (ANN, de l'anglais *Artificial Neural Networks*) est simplement un réseau multi-tranches de neurones (ou noeuds) qui nous permet de classifier, faire des prédictions, etc. Pour faciliter une discussion sur les ANNs, on inclut la figure 1.13.

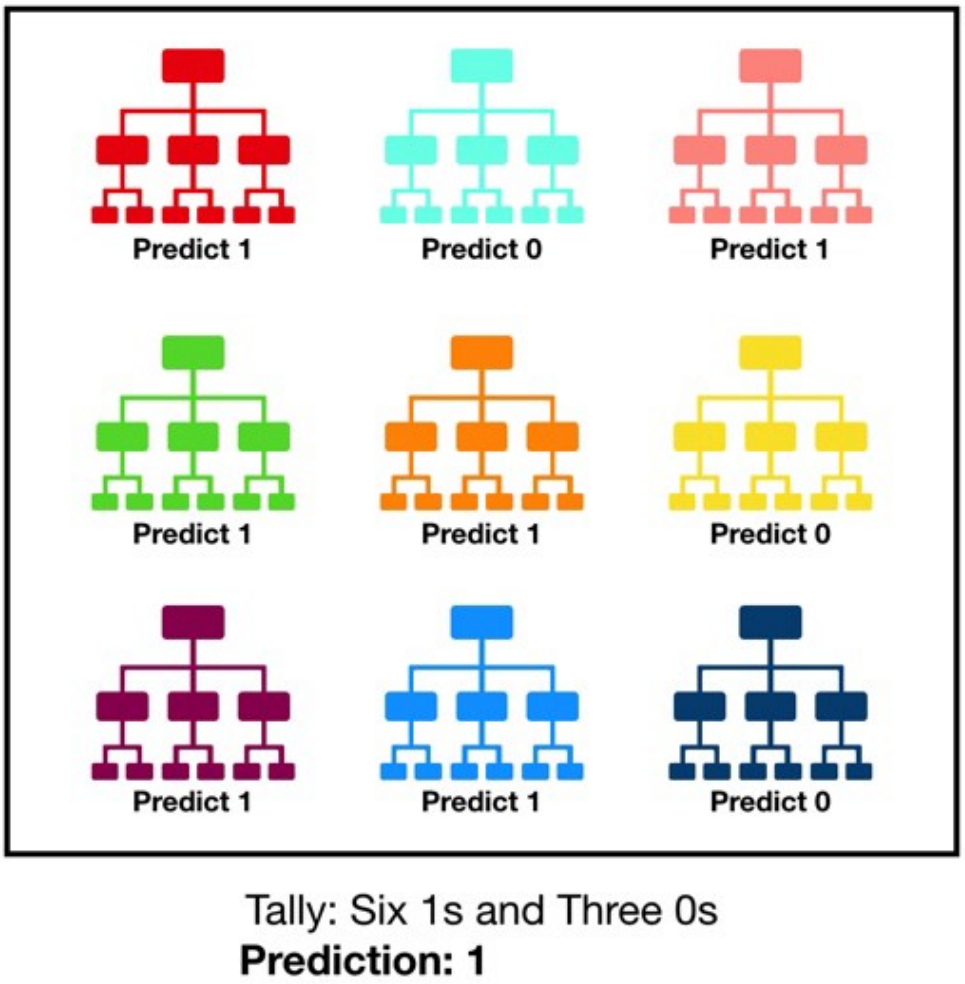

Fig. 1.12. Le graphique montre un arbre aléatoire comme un ensemble d'arbres de décision. On voit que l'arbre aléatoire choisit la valeur prédite par la plupart des arbres de décision individuelle. Source : TowardsDataScience

Un ANN consiste en un ensemble de noeuds qui appartiennent à une de trois tranches : une couche d'entrée, une couche de sortie et une couche cachée. Chaque trait qui connecte un noeud avec un autre porte une valeur qui s'appelle le poids (**W**) et chaque noeud porte une autre valeur qui s'appelle un biais (**B**). À chaque couche cachée, nous calculons un vecteur intermédiaire, **Z**, en utilisant nos vecteurs **W**, **B** et **X**. Ici, **X** représente le vecteur des *entrées*. L'équation est simple: $\vec{W} * \vec{X} + \vec{B} = \vec{Z}$. Après ce calcul, nous appliquons une fonction d'activation (comme une fonction sigmoïde) à **Z** pour calculer les sorties de neurones. Maintenant qu'on a une façon de nous déplacer dans un réseau, on peut explorer l'entraînement d'un réseau. Cette technique nous permet d'obtenir les bonnes réponses de chaque entrée et ainsi, nous pouvons comparer nos prédictions avec les résultats déjà connus. On utilise une fonction de coût pour quantifier cette valeur; telle que la fonction moyenne erreur standard (MSE, de l'anglais *Mean Squared Error*) qui est :

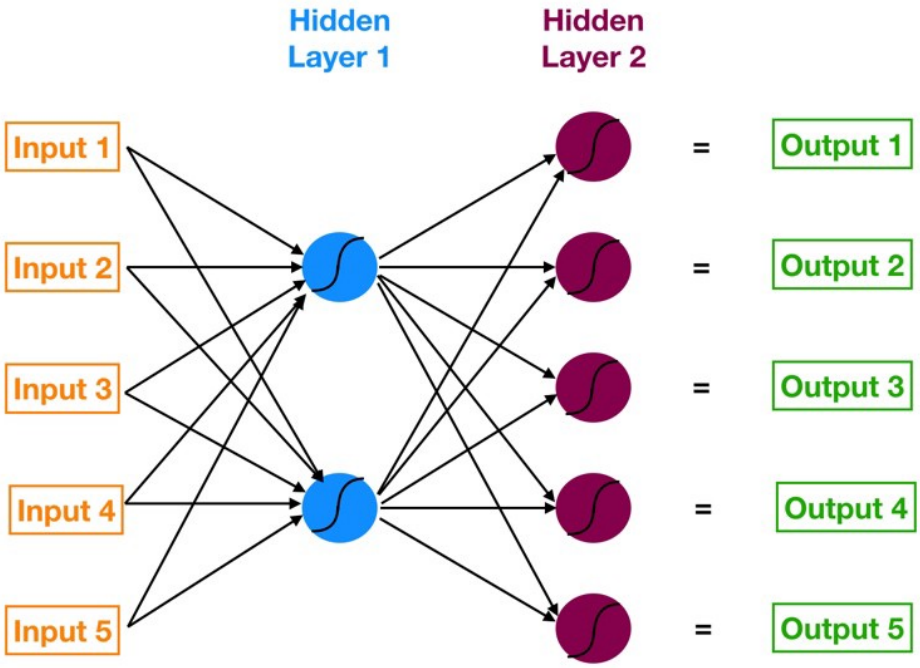

Fig. 1.13. Réseau de neurones artificiel avec deux couches cachées et sept noeuds au total. On voit que chaque couche cachée est entièrement connectée à la prochaine couche. Source: TowardsDataScience

$$MSE = \sum[(\text{Pred} - \text{True})^2](1/\text{num\_obs}) \tag{1.5.1}$$

où Pred est la valeur prédite, True est la valeur connue et num_obs est le nombre d'observations. Pendant l'étape d'entraînement, nous laissons les noeuds changer la valeur des poids pour minimiser notre fonction de coût. En faisant cette étape plusieurs fois, on peut trouver les valeurs de poids et biais qui permettent une bonne prédiction.

Un réseau de neurones convolutif utilise la structure d'un ANN et ajoute deux couches : une couche de convolution et une couche de mutualisation. La couche de convolution est utilisée pour extraire les caractéristiques importantes des entrées. Cette couche fait une convolution matricielle sous la forme d'un produit scalaire qui aboutit en une sortie plus petite que l'entrée initiale. La couche de mutualisation fait un autre processus qui réduit de nouveau la taille pour accélérer les calculs et diminuer le surajustement. Avec les deux couches supplémentaires, notre réseau de neurones est plus puissant et bien construit pour les spectres.

1.6. Télescopes

Pour étudier les phénomènes décrits dans §1.1, nous utilisons les télescopes et les instruments qui permettent d'explorer plusieurs régions et phénomènes astrophysiques. Dans cette section, nous allons explorer deux télescopes importants : le *Chandra X-ray Observatory* et le télescope Canada-France-Hawaii (CFHT).

1.6.1. Observatoire rayons X Chandra

Le vaste dépôt des données en rayons X n'aurait pas été possible sans le satellite *Chandra*, montré dans la figure 1.14. Nommé après le célèbre astrophysicien Subrahmanyan Chandrasekhar, l'observatoire *Chandra* a été déployé le 23 juillet 1999. En raison de son orbite elliptique, *Chandra* oscille entre 131 km et 9 600 km au-dessus de la surface de la Terre et chaque orbite prend plus de soixante heures[2]. Étant donné leur haute énergie, les photons rayons X doivent être réfléchit avant de pouvoir les accumuler. À partir de cette contrainte, l'équipe de *Chandra* a construit un système de 4 miroirs paraboliques imbriqués et 4 miroirs hyperboliques imbriqués pour canaliser les photons entrants sur un imageur standard et un système de dispositifs à transfert de charge (CCD, de l'anglais *Charge-Coupled Device*; p. ex. Howell 2006; Martinez and Klotz).

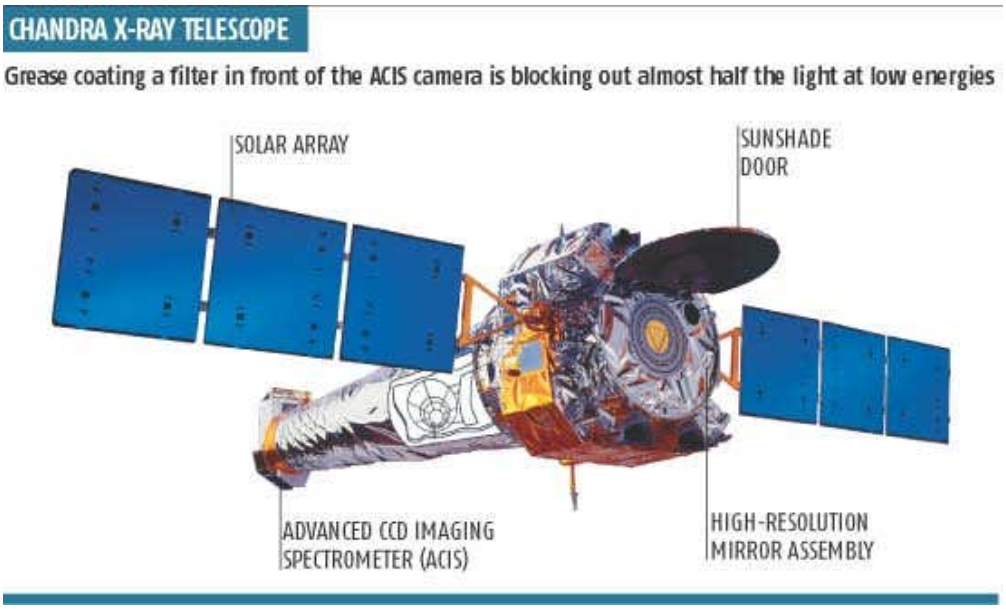

Fig. 1.14. Interprétation artistique du *Chandra X-ray Observatory* qui inclut les panneaux solaires. Source: NASA/CXC

Le système de miroirs s'appelle le HRMA (*High Resolution Mirror Assembly*) et une grande partie du succès du télescope est due à ce mécanisme d'accumulation des photons

[2]http://chandra.harvard.edu/about/science_instruments.html

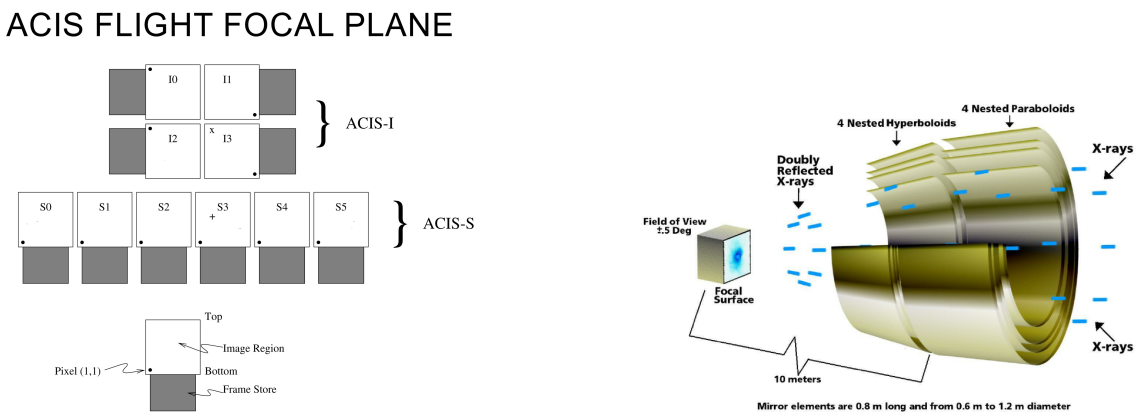

(a) Configurations de deux configurations de CCDs dans *Chandra*: ACIS-I et ACIS-S.

(b) Schématique des miroirs utilisés par *Chandra*.

Fig. 1.15. Chaque CCD dans l'ensemble ACIS (*Advanced CCD Imaging Spectrometer*) couvre 8.4‘ × 8.4‘. Source: NASA/CXC

(voir figure 1.15; Garmire et al. 2003). Au total, il y a plusieurs instruments: la caméra haute résolution (HRC, de l'anglais *High Resolution Camera*), l'ensemble de CCDs (ACIS, de l'anglais *Advanced CCD Imaging Spectrometer*, le spectromètre à réseau de transmission à haute énergie (HETGS, de l'anglais *High Energy Transmission Grating Spectrometer*) et le spectromètre à réseau de transmission à basse énergie (LETS, de l'anglais *Low Energy Transmission Grating Spectrometer*). Les spectromètres à réseau de diffraction sont moins utilisés que le HRC et l'ACIS qui sont situés sur le plan primaire du télescope. Cependant, ils nous permettent d'étudier les objets avec une meilleure résolution spectrale et sont toujours bien employés (p. ex. Lobban et al. 2011; Reynolds et al. 2020). Depuis le lancement du télescope, le domaine de l'astronomie en rayons X a changé énormément grâce à la performance de *Chandra*; pour la première fois, les scientifiques ont la capacité de résoudre les sources d'une taille d'environ 0.5 arcsecondes (p. ex. Weisskopf et al. 2000; Weisskopf et al. 2002).

Dans les articles présentés dans ce mémoire, nous utilisons uniquement les deux regroupements d'ACIS : nous le présentons donc en plus de détails ici et dans la figure 1.15. Les dix CCDs nous permettent de prendre des images à haute résolution avec des spectres d'une résolution sans précédent d'environ 150 eV (p. ex. Broos et al. 2010; Garmire et al. 2003; Li et al. 2004). Chaque CCD contient 1024 pixels par 1024 pixels. Ils contiennent un mélange de CCDs éclairés à dos (BI, de l'anglais *Back-Illuminated*; 6) et éclairés de front (FI, de l'anglais *Front-Illuminated*; 4). En général, le temps de lecture (*read-out time*) est de 3.2 secondes. Chaque photon qui frappe le détecteur est considéré comme un événement qui va être utilisé par le logiciel de réduction et de traitement des données. Le détecteur

attribue un grade à chaque photon détecté, ce qui nous permet de déterminer la qualité de chaque événement. Sur les vingt dernières années d'usage, la qualité des CCDs a lentement dégradé et ceux-ci fonctionnent mieux au-dessous de 2 keV (p. ex. Plucinsky et al. 2018).

L'usage de cet instrument est primordial pour obtenir les résultats qu'on a aujourd'hui. À partir du téléchargement de données brutes de l'archive de *Chandra*, l'utilisateur a plusieurs outils à sa disposition, grâce au travail de l'équipe de logiciel au centre rayons X de *Chandra* (*CXC*, de l'anglais *Chandra X-ray Center*). Pour retraiter les données, nous choisissons d'abord un CCD sans émission de notre objet, enlevons les sources ponctuelles en utilisant l'outil `VTPDETECT` et trouvons les temps où il y a eu un événement tel qu'une éruption solaire (*background flaring event*) avec `LC_SIGMA_CLIP`. Puis, nous enlevons les rayons cosmiques avec `DESTREAK`. Nous marquons tous les pixels dans les observations où il y a un problème en utilisant `ACIS_BUILD_BADPIX`. Ensuite, nous employons l'outil `ACIS_PROCESS_EVENTS`. À partir de cela, nous pouvons utiliser le nouveau fichier pour l'analyse photométrique et spectroscopique.

1.6.2. Télescope Canada-France-Hawaii

Le CFHT est situé au sommet de Mauna Kea sur l'île d'Hawaii et a débuté ses opérations en 1979. Avec le télescope de 3,6 mètres, les astronomes peuvent regarder le cosmos en visible et en infrarouge. Le CFHT possède cinq instruments: MegaCAM (un imageur optique de grand champ), WIRCam (un imageur infrarouge de grand champ), ESPaDOnS (un spectrographe et spectropolarimeter optique), SPIRou (un spectropolarimeter en proche infrarouge) et finalement SITELLE (Spectromètre Imageur à Transformée de Fourier pour l'Étude en Long et en Large de raies de l'émission). À partir du 7 juillet 2015, SITELLE a été disponible au CFHT. SITELLE est le successeur d'un instrument construit au Québec: SpiOMM. SITELLE est un interféromètre fortement inspiré de l'interféromètre de Michelson. L'imageur est montré dans la figure 1.16.

Grâce à la taille de ses pixels (0.32") et à la visibilité au sommet de Mauna Kea ($\sim$0.8"), SITELLE produit des spectres à haute résolution spatiale. Les détecteurs de SITELLE sont deux e2v CCDs de 2048 pixels par 2048 pixels chaque. Il y a neuf filtres disponibles qui couvrent une gamme de longueurs d'onde de 350 nm à 900 nm. L'impressionnant champ de vue de SITELLE, 11'$\times$11', est plus de 100 fois plus grand que l'IFU (*Integral Field Unit*) MUSE (p. ex. Drissen et al. 2014; Drissen et al. 2019). De plus, l'utilisateur a le choix d'une résolution spectrale entre 1 et 10 000.

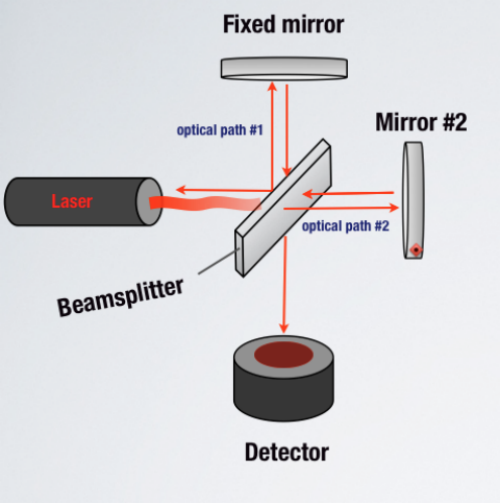

(a) L'appareil classique de Michelson

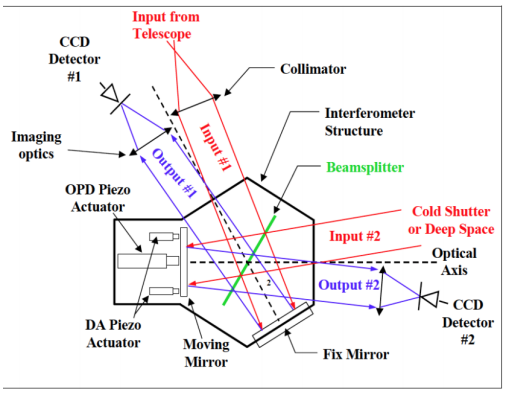

(b) Le schéma de SITELLE

Fig. 1.16. L'instrument SITELLE est basé sur l'appareil classique de Michelson avec plusieurs modifications qui lui permettent d'atteindre une plus haute résolution spectrale. Source: FTS-Primer

La résolution spectrale et spatiale étonnante de SITELLE rend les données complexes; chaque observation de SITELLE aboutit à un cube de données avec des dimensions 2048 pixels par 2048 pixels (spatial en x et y) multiplié par la résolution spectrale. Ainsi, on a plus de 4 000 000 pixels qui contiennent chacun un spectre. La figure 1.17 présente la complexité d'un cube de SITELLE. L'équipe de logiciel au CFHT, en collaboration avec l'Université Laval, a créé le logiciel nécessaire pour traiter et analyser ces données ; il y a trois modules Python pour faire les étapes différentes : `ORB` (Outils de réduction binoculaire), `ORBS` (Outil de réduction binoculaire pour SITELLE) et `ORCS` (Outil de réduction de cubes spectraux)[3].

1.7. Description de ce mémoire

Les trois chapitres de ce mémoire portent sur les amas de galaxies, le ICM et l'émission de gaz dans les galaxies individuelles. Il y a deux objectifs principaux dans ce mémoire: investiguer la raison derrière la formation stellaire élevée dans des amas à des décalages vers le rouge élevés (article 1) et explorer l'usage de l'apprentissage automatique pour les études observationnelles de galaxies et d'amas de galaxies (articles 2 et 3).

Dans le premier article, nous étudions SpARCS104922.6+564032.5, un amas de galaxies avec un décalage vers le rouge élevé qui présente une formation stellaire deux ordres de magnitude plus haute que prévu pour un amas à cette distance. De plus, la région de cette

[3]On peut trouver le code à ce site web : `https://github.com/thomasorb`

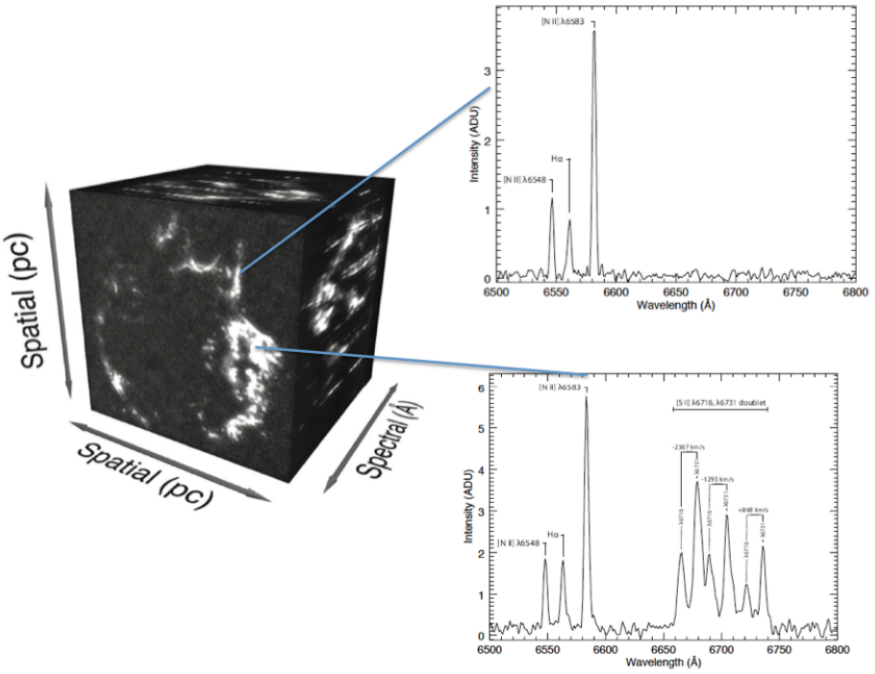

Fig. 1.17. Exemple d'un cube spectral de SITELLE. Cet exemple démontre la complexité des données prises par SITELLE puisqu'à chaque pixel spatial il y a un spectre entier. Source: FPS-Primer

formation élevée est située à plusieurs dizaines de kpc de la BCG. Dans cet article, nous présentons les premières données en rayons X prises de cet objet. Les observations ont été prises par *Chandra* en 2017 et à cause de la distance de l'amas, l'analyse s'est avéré difficile à traiter et à analyser. Les résultats montrent qu'il s'agit d'un amas de type CCC dont le coeur froid est décalé de la BCG dans la même direction que la formation stellaire.

Dans le deuxième article, nous utilisons encore une fois les rayons X pour étudier les amas de galaxies. Cependant, nous n'étudions pas un amas lointain, mais nous développons plutôt une nouvelle méthodologie pour mieux analyser leur émission. En particulier, nous voulions déterminer une meilleure façon de distinguer le nombre de composantes thermiques sous-jacentes dans un spectre. Pour régler ce problème, nous avons utilisé une combinaison d'algorithmes d'apprentissage automatique: l'analyse de composantes principales et un classificateur d'arbres aléatoires. Nos résultats nous indiquent que les techniques capturent bien la structure dans l'émission et prédisent bien le nombre de composantes.

Le troisième est une étude de l'utilisation de l'apprentissage automatique sur les spectres de l'instrument SITELLE. Ici, l'apprentissage automatique est utilisé pour estimer directement les paramètres de l'émission : la vitesse et la dispersion du gaz à partir des

spectres. Dans cet article, nous utilisons un réseau de neurones convolutif pour calculer les valeurs; après l'entraînement avec les spectres synthétiques, le réseau réussit à trouver ces paramètres avec précision.

Chacun des articles est déjà accepté ou soumis à une révision scientifique.

Dans le dernier chapitre, nous résumons les découvertes les plus importantes et les prochaines étapes à faire. Nous avons trois annexes dans lesquelles nous énumérons les publications à titre de co-auteur, les congrès dans lesquels j'ai présenté mes résultats et mes demandes de temps observationnelles. Tout ce qui est présenté dans ce mémoire a été accompli durant ma maîtrise.

1.8. Déclaration de l'étudiant

Je déclare que tout le travail fait dans ce mémoire a été effectué par l'auteur, Carter Rhea, sauf indication contraire. Dans cette section, j'esquisse le travail qui n'a pas été fait par moi; si le crédit n'est pas mentionné explicitement, le travail est l'oeuvre de l'auteur.

Au début de mes études, nous avions envisagé que je travaillerais uniquement sur le premier article, celui qui concerne SpARCS104922.6+564032.5. Cependant, après avoir produit les images montrant les résultats clés, la collaboration a décidé de soumettre l'article à Nature vu l'importance des résultats. Étant donné la nature compétitive de ce journal, Dr Hlavacek-Larrondo a pris la relève en tant que première auteur, mais nous avons tout de même inclut cet article dans le mémoire en raison de mes contributions majeures.

Au cours de la deuxième année, et suite à des discussions avec Dr Hlavacek-Larrondo, j'ai eu l'idée d'appliquer des techniques d'apprentissage automatique aux spectres rayons X des amas de galaxies. J'ai donc moi-même proposé et développé cette idée, en prenant les initiatives d'écrire le deuxième article présenté dans ce mémoire. Similairement, le troisième article est né d'une idée que j'ai proposé aux membres de l'équipe SITELLE. Ces exemples démontrent mes compétences pour la recherche, non seulement en ce qui concerne la proposition d'idées originales mais aussi ma capacité de mener rapidement des projets à terme.

En résumé, le premier article est une oeuvre accomplie principalement par Dr Hlavacek-Larrondo, ma directrice de recherche et moi-même. Dr Hlavacek-Larrondo a écrit la majorité du papier sauf la section § 2.1, qui a été écrit par Carter Rhea. Dr Hlavacek-Larrondo a créé les figures 1 et 2, tandis que l'auteur de ce mémoire a créé les figures 3 et 4. Dr

Hlavacek-Larrondo a dirigé l'interprétation des résultats. Carter Rhea a fait le traitement de données en rayons X et a calculé les quantités projetées. Toutefois, Dr McDonald a mené l'analyse des quantités deprojetées. Kyle Finner et James Jee ont fait le traitement de données et l'analyse des observations des lentilles gravitationnelles. Dr Webb est la chercheuse principale des observations faites avec le VLA; les données ont été réduites par Felix Valin. Dr Muzzin et Dr Wilson ont contribué activement au projet. Les autres auteurs nous ont donné des commentaires sur le manuscrit.

Le deuxième article a été entièrement écrit par l'étudiant, Carter Rhea. Dr Hlavacek-Larrondo a fourni des commentaires sur les aspects astronomiques. Dr Perreault-Levasseur m'a aidé avec la discussion des résultats de l'apprentissage automatique. Nous nous rencontrions pour discuter de l'apprentissage automatique et son aide a été essentielle. Dr Gendron-Marsolais a fourni des commentaires.

Le troisième article est le résultat du stage à Hawaii fait par l'étudiant. Pendant que j'étais en stage au CFHT en Waimea, Hawaii, j'ai travaillé avec Laurie Rousseau-Nepton et Simon Prunet, les scientifiques responsables de l'instrument SITELLE. Dr Rousseau-Nepton m'a fourni des commentaires et de l'aide avec la modélisation de données de SITELLE et elle a aussi écrit la majorité de l'introduction. Dr Prunet nous a envoyé des commentaires sur la première tentative et nous avons eu plusieurs discussions sur l'apprentissage automatique.

Références bibliographiques

M. A. Abramowicz and P. C. Fragile. Foundations of Black Hole Accretion Disk Theory. *Living Reviews in Relativity*, 16(1):1, Jan. 2013. ISSN 1433-8351. doi: 10.12942/lrr-2013-1. URL `https://doi.org/10.12942/lrr-2013-1`.

J. A. Baldwin, M. M. Phillips, and R. Terlevich. Classification parameters for the emission-line spectra of extragalactic objects. *Publications of the Astronomical Society of the Pacific*, 93:5, Feb. 1981. ISSN 0004-6280, 1538-3873. doi: 10.1086/130766. URL `http://iopscience.iop.org/article/10.1086/130766`.

N. M. Ball and R. J. Brunner. Data Mining and Machine Learning in Astronomy. *International Journal of Modern Physics D*, 19(07):1049–1106, July 2010. ISSN 0218-2718, 1793-6594. doi: 10.1142/S0218271810017160. URL `http://arxiv.org/abs/0906.2173`. arXiv: 0906.2173.

D. Baron. Machine Learning in Astronomy: a practical overview. *arXiv:1904.07248 [astro-ph]*, Apr. 2019. URL `http://arxiv.org/abs/1904.07248`. arXiv: 1904.07248.

N. Bennert, H. Falcke, H. Schulz, A. S. Wilson, and B. J. Wills. Size and Structure of the Narrow-Line Region of Quasars. *The Astrophysical Journal*, 574(2):L105–L109, Aug. 2002.

ISSN 0004637X, 15384357. doi: 10.1086/342420. URL https://iopscience.iop.org/article/10.1086/342420.

J. Binney and S. Tremaine. *Galactic Dynamics*. Princeton University Press, 1987. ISBN 978-0-691-08445-9. Google-Books-ID: 01yNf7mipb0C.

L. Birzan, D. A. Rafferty, B. R. McNamara, M. W. Wise, and P. E. J. Nulsen. A Systematic Study of Radio-Induced X-ray Cavities in Clusters, Groups, and Galaxies. *The Astrophysical Journal*, 607(2):800–809, June 2004. ISSN 0004-637X, 1538-4357. doi: 10.1086/383519. URL http://arxiv.org/abs/astro-ph/0402348. arXiv: astro-ph/0402348.

R. Blandford and R. Znajek. Electromagnetic extraction of energy from Kerr black holes. *MNRAS*, 179:433–456, 1977.

R. D. Blandford and D. G. Payne. Hydromagnetic flows from accretion discs and the production of radio jets. *Monthly Notices of the Royal Astronomical Society*, 199(4): 883–903, Aug. 1982. ISSN 0035-8711, 1365-2966. doi: 10.1093/mnras/199.4.883. URL https://academic.oup.com/mnras/article-lookup/doi/10.1093/mnras/199.4.883.

R. D. Blandford and M. J. Rees. FOR DOUBLE RADIO SOURCES. page 21, 1974.

H. Boehringer and N. Werner. X-ray Spectroscopy of Galaxy Clusters. *arXiv:0907.4277 [astro-ph]*, July 2009. URL http://arxiv.org/abs/0907.4277. arXiv: 0907.4277.

L. Breiman. Bagging predictors. *Machine Learning*, 24(2):123–140, Aug. 1996. ISSN 0885-6125, 1573-0565. doi: 10.1007/BF00058655. URL http://link.springer.com/10.1007/BF00058655.

L. Breiman. Random Forests. *Machine Learning*, 45:5–32, 2001.

L. Breiman, J. Friedman, R. Olshen, and C. Stone. *Classification and Regression Trees*. Wadsworth, 1984.

P. S. Broos, L. K. Townsley, E. D. Feigelson, K. V. Getman, F. E. Bauer, and G. P. Garmire. INNOVATIONS IN THE ANALYSIS OF *CHANDRA* -ACIS OBSERVATIONS. *The Astrophysical Journal*, 714(2):1582–1605, May 2010. ISSN 0004-637X, 1538-4357. doi: 10.1088/0004-637X/714/2/1582. URL http://stacks.iop.org/0004-637X/714/i=2/a=1582?key=crossref.6ea08ce0210b89154c790c259505eff8.

B. Carroll and D. Ostlie. *An introduction to modern astrophysics*. Peasron Addison-Wesley, San Fransisco, CA, USA, 6 edition, 2007.

A. Castro-Ginard, C. Jordi, X. Luri, F. Julbe, M. Morvan, L. Balaguer-Núñez, and T. Cantat-Gaudin. A new method for unveiling Open Clusters in Gaia: new nearby Open Clusters confirmed by DR2. *Astronomy & Astrophysics*, 618:A59, Oct. 2018. ISSN 0004-6361, 1432-0746. doi: 10.1051/0004-6361/201833390. URL http://arxiv.org/abs/1805.03045. arXiv: 1805.03045.

A. R. Choudhuri and P. o. P. A. R. Choudhuri. *The Physics of Fluids and Plasmas: An Introduction for Astrophysicists*. Cambridge University Press, Nov. 1998. ISBN 978-0-521-55543-2. Google-Books-ID: i_kufpYwkpQC.

E. Churazov, S. Sazonov, R. Sunyaev, W. Forman, C. Jones, and H. Böhringer. Supermassive black holes in elliptical galaxies: switching from very bright to very dim. *Monthly Notices of the Royal Astronomical Society: Letters*, 363(1):L91–L95, Oct. 2005. ISSN 1745-3925. doi: 10.1111/j.1745-3933.2005.00093.x. URL https://academic.oup.com/mnrasl/article/363/1/L91/952713. Publisher: Oxford Academic.

R. Cohen. The narrow-line region of intermediate Seyfert galaxies. *Astrophysical Journal*, 273:489–504, 1983. URL http://adsabs.harvard.edu/full/1983ApJ...273..489C.

G. De Lucia and J. Blaizot. The hierarchical formation of the brightest cluster galaxies. *Monthly Notices of the Royal Astronomical Society*, 375(1):2–14, Feb. 2007. ISSN 0035-8711, 1365-2966. doi: 10.1111/j.1365-2966.2006.11287.x. URL https://academic.oup.com/mnras/article-lookup/doi/10.1111/j.1365-2966.2006.11287.x.

M. Donahue, D. J. Horner, K. W. Cavagnolo, and G. M. Voit. Entropy Profiles in the Cores of Cooling Flow Clusters of Galaxies. *The Astrophysical Journal*, 643(2):730–750, June 2006. ISSN 0004-637X, 1538-4357. doi: 10.1086/503270. URL https://iopscience.iop.org/article/10.1086/503270.

L. Drissen, L. Rousseau-Nepton, S. Lavoie, C. Robert, T. Martin, P. Martin, J. Mandar, and F. Grandmont. Imaging FTS: A Different Approach to Integral Field Spectroscopy. *Advances in Astronomy*, 2014:1–15, 2014. ISSN 1687-7969, 1687-7977. doi: 10.1155/2014/293856. URL http://www.hindawi.com/journals/aa/2014/293856/.

L. Drissen, T. Martin, L. Rousseau-Nepton, C. Robert, R. P. Martin, M. Baril, S. Prunet, G. Joncas, S. Thibault, D. Brousseau, J. Mandar, F. Grandmont, H. Yee, and L. Simard. SITELLE: an Imaging Fourier Transform Spectrometer for the Canada–France–Hawaii Telescope. *Monthly Notices of the Royal Astronomical Society*, 485(3):3930–3946, May 2019. ISSN 0035-8711, 1365-2966. doi: 10.1093/mnras/stz627. URL https://academic.oup.com/mnras/article/485/3/3930/5372442.

J. Dubinski. The Origin of the Brightest Cluster Galaxies. *The Astrophysical Journal*, 502(1):141–149, July 1998. ISSN 0004-637X, 1538-4357. doi: 10.1086/305901. URL https://iopscience.iop.org/article/10.1086/305901.

A. C. Fabian. Cosmic Feedback from AGN. *Proceedings of the International Astronomical Union*, 5(S267):341–349, Aug. 2009. ISSN 1743-9213, 1743-9221. doi: 10.1017/S1743921310006691. URL http://arxiv.org/abs/0912.0880. arXiv: 0912.0880.

A. C. Fabian, J. S. Sanders, S. W. Allen, C. S. Crawford, K. Iwasawa, R. M. Johnstone, R. W. Schmidt, and G. B. Taylor. A deep Chandra observation of the Perseus cluster: shocks and ripples. *Monthly Notices of the Royal Astronomical Society*, 344(3):L43–L47, Sept. 2003. ISSN 0035-8711, 1365-2966. doi: 10.1046/j.1365-8711.2003.06902.x. URL http://arxiv.org/abs/astro-ph/0306036. arXiv: astro-ph/0306036.

A. C. Fabian, J. S. Sanders, S. W. Allen, R. E. A. Canning, E. Churazov, C. S. Crawford, W. Forman, J. GaBany, J. Hlavacek-Larrondo, R. M. Johnstone, H. R. Russell, C. S. Reynolds, P. Salomé, G. B. Taylor, and A. J. Young. A wide Chandra view of the core of the Perseus cluster: A wider view of the Perseus cluster. *Monthly Notices of the Royal Astronomical Society*, 418(4):2154–2164, Dec. 2011. ISSN 00358711. doi: 10.1111/j.1365-2966.2011.19402.x. URL https://academic.oup.com/mnras/article-lookup/doi/10.1111/j.1365-2966.2011.19402.x.

S. C. Gallagher and J. E. Everett. Stratified Quasar Winds: Integrating X-ray and Infrared Views of Broad Absorption Line Quasars. *arXiv:astro-ph/0701076*, Feb. 2007. URL http://arxiv.org/abs/astro-ph/0701076. arXiv: astro-ph/0701076.

Z. Gan, F. Yuan, J. P. Ostriker, L. Ciotti, and G. S. Novak. ACTIVE GALACTIC NUCLEUS FEEDBACK IN AN ISOLATED ELLIPTICAL GALAXY: THE EFFECT OF STRONG RADIATIVE FEEDBACK IN THE KINETIC MODE. *The Astrophysical Journal*, 789(2): 150, June 2014. ISSN 0004-637X, 1538-4357. doi: 10.1088/0004-637X/789/2/150. URL https://iopscience.iop.org/article/10.1088/0004-637X/789/2/150.

G. P. Garmire, M. W. Bautz, P. G. Ford, J. A. Nousek, and G. R. Ricker, Jr. Advanced CCD imaging spectrometer (ACIS) instrument on the Chandra X-ray Observatory. page 28, Waikoloa, Hawai'i, United States, Mar. 2003. doi: 10.1117/12.461599. URL http://proceedings.spiedigitallibrary.org/proceeding.aspx?doi=10.1117/12.461599.

F. Hamann, G. Chartas, S. McGraw, P. R. Hidalgo, J. Shields, D. Capellupo, J. Charlton, and M. Eracleous. Extreme-Velocity Quasar Outflows and the Role of X-ray Shielding. *Monthly Notices of the Royal Astronomical Society*, 435(1):133–148, Oct. 2013. ISSN 1365-2966, 0035-8711. doi: 10.1093/mnras/stt1231. URL http://arxiv.org/abs/1307.1173. arXiv: 1307.1173.

J. Hlavacek-Larrondo, A. C. Fabian, A. C. Edge, and M. T. Hogan. On the hunt for ultramassive black holes in brightest cluster galaxies. *Monthly Notices of the Royal Astronomical Society*, 424(1):224–231, July 2012. ISSN 00358711. doi: 10.1111/j.1365-2966.2012.21187.x. URL http://arxiv.org/abs/1204.5759. arXiv: 1204.5759.

J. Hlavacek-Larrondo, M. McDonald, B. A. Benson, W. R. Forman, S. W. Allen, L. E. Bleem, M. L. N. Ashby, S. Bocquet, M. Brodwin, J. P. Dietrich, C. Jones, J. Liu, C. L. Reichardt, B. R. Saliwanchik, A. Saro, T. Schrabback, J. Song, B. Stalder, A. Vikhlinin, and A. Zenteno. X-RAY CAVITIES IN A SAMPLE OF 83 SPT-SELECTED CLUSTERS OF GALAXIES: TRACING THE EVOLUTION OF AGN FEEDBACK IN CLUSTERS OF GALAXIES OUT TO $z = 1.2$. *The Astrophysical Journal*, 805(1):35, May 2015. ISSN 1538-4357. doi: 10.1088/0004-637X/805/1/35. URL http://stacks.iop.org/0004-637X/805/i=1/a=35?key=crossref.f300ddb3311d9d4ee0e536bea2a0b0cc.

P. F. Hopkins and M. Elvis. Quasar feedback: more bang for your buck. *Monthly Notices of the Royal Astronomical Society*, 401(1):7–14, Jan. 2010. ISSN 0035-8711. doi: 10.1111/

j.1365-2966.2009.15643.x. URL https://academic.oup.com/mnras/article/401/1/7/1000436. Publisher: Oxford Academic.

S. B. Howell. *Handbook of CCD Astronomy*. Cambridge University Press, Cambridge, 2006. ISBN 978-0-521-85215-9 978-0-511-80790-9 978-0-511-16105-6. OCLC: 859642197.

D. S. Hudson, R. Mittal, T. H. Reiprich, P. E. J. Nulsen, H. Andernach, and C. L. Sarazin. What is a cool-core cluster? a detailed analysis of the cores of the X-ray flux-limited *HIFLUGCS* cluster sample. *Astronomy and Astrophysics*, 513:A37, Apr. 2010. ISSN 0004-6361, 1432-0746. doi: 10.1051/0004-6361/200912377. URL http://www.aanda.org/10.1051/0004-6361/200912377.

I. T. Jolliffe and J. Cadima. Principal component analysis: a review and recent developments. *Philosophical Transactions of the Royal Society A: Mathematical, Physical and Engineering Sciences*, 374(2065):20150202, Apr. 2016. ISSN 1364-503X, 1471-2962. doi: 10.1098/rsta.2015.0202. URL https://royalsocietypublishing.org/doi/10.1098/rsta.2015.0202.

S. Kaspi, D. Maoz, H. Netzer, B. M. Peterson, M. Vestergaard, and B. T. Jannuzi. The Relationship between Luminosity and Broad-Line Region Size in Active Galactic Nuclei. *The Astrophysical Journal*, 629(1):61–71, Aug. 2005. ISSN 0004-637X, 1538-4357. doi: 10.1086/431275. URL https://iopscience.iop.org/article/10.1086/431275.

L. J. Kewley, B. Groves, G. Kauffmann, and T. Heckman. The Host Galaxies and Classification of Active Galactic Nuclei. *Monthly Notices of the Royal Astronomical Society*, 372(3):961–976, Nov. 2006. ISSN 0035-8711, 1365-2966. doi: 10.1111/j.1365-2966.2006.10859.x. URL http://arxiv.org/abs/astro-ph/0605681. arXiv: astro-ph/0605681.

S. Lea, J. Silk, E. Kellogg, and S. Murray. Thermal-Bremsstrahlung Interpretatino of Cluster X-ray Sources. *Astrophysical Journal*, 184, 1973.

J. Li, J. H. Kastner, G. Y. Prigozhin, N. S. Schulz, E. D. Feigelson, and K. V. Getman. *Chandra* ACIS Subpixel Event Repositioning: Further Refinements and Comparison between Backside- and Frontside-illuminated X-Ray CCDs. *The Astrophysical Journal*, 610(2):1204–1212, Aug. 2004. ISSN 0004-637X, 1538-4357. doi: 10.1086/421866. URL http://stacks.iop.org/0004-637X/610/i=2/a=1204.

A. P. Lobban, J. N. Reeves, L. Miller, T. J. Turner, V. Braito, S. B. Kraemer, and D. M. Crenshaw. Contemporaneous Chandra HETG and Suzaku X-ray observations of NGC 4051: A study of NGC 4051 with Chandra and Suzaku. *Monthly Notices of the Royal Astronomical Society*, 414(3):1965–1986, July 2011. ISSN 00358711. doi: 10.1111/j.1365-2966.2011.18513.x. URL https://academic.oup.com/mnras/article-lookup/doi/10.1111/j.1365-2966.2011.18513.x.

P. Martinez and A. Klotz. A Practical Guide to CCD Astronomy. page 7.

T. Matthews, W. Morgan, and M. Schmidt. A Discussion of Galaxies Identified with Radio Source. *Astrophysical Journal*, 140, 1964.

B. Maughan. Self-similar scaling and evolution in the galaxy cluster X-ray luminosity–temperature relation | Monthly Notices of the Royal Astronomical Society | Oxford Academic. *MNRAS*, 421(2):1583–1602, 2012. URL https://academic.oup.com/mnras/article/421/2/1583/1142210.

M. McDonald, B. R. McNamara, R. J. v. Weeren, D. E. Applegate, M. Bayliss, M. W. Bautz, B. A. Benson, J. E. Carlstrom, L. E. Bleem, M. Chatzikos, A. C. Edge, A. C. Fabian, G. P. Garmire, J. Hlavacek-Larrondo, C. Jones-Forman, A. B. Mantz, E. D. Miller, B. Stalder, S. Veilleux, and J. A. ZuHone. DEEP *CHANDRA* , *HST* -COS, AND MEGACAM OBSERVATIONS OF THE PHOENIX CLUSTER: EXTREME STAR FORMATION AND AGN FEEDBACK ON HUNDRED KILOPARSEC SCALES. *The Astrophysical Journal*, 811(2):111, Sept. 2015. ISSN 1538-4357. doi: 10.1088/0004-637X/811/2/111. URL http://stacks.iop.org/0004-637X/811/i=2/a=111?key=crossref.9d41090f62b59bb889c0fa6062baf12b.

R. C. McGurk, A. E. Kimball, and Ivezić. PRINCIPAL COMPONENT ANALYSIS OF SLOAN DIGITAL SKY SURVEY STELLAR SPECTRA. *The Astronomical Journal*, 139(3):1261–1268, Mar. 2010. ISSN 0004-6256, 1538-3881. doi: 10.1088/0004-6256/139/3/1261. URL http://stacks.iop.org/1538-3881/139/i=3/a=1261?key=crossref.32b7caa840bfd602083692ed6456c017.

B. McNamara and P. Nulsen. Mechanical feedback from active galactic nuclei in galaxies, groups and clusters. *New Journal of Physics*, 14, 2012.

B. R. McNamara and P. E. J. Nulsen. Heating Hot Atmospheres with Active Galactic Nuclei. *Annual Review of Astronomy and Astrophysics*, 45(1):117–175, Sept. 2007. ISSN 0066-4146, 1545-4282. doi: 10.1146/annurev.astro.45.051806.110625. URL http://arxiv.org/abs/0709.2152. arXiv: 0709.2152.

B. R. McNamara, P. E. J. Nulsen, M. W. Wise, D. A. Rafferty, C. Carilli, C. L. Sarazin, and E. L. Blanton. The heating of gas in a galaxy cluster by X-ray cavities and large-scale shock fronts. *Nature*, 433(7021):45–47, Jan. 2005. ISSN 1476-4687. doi: 10.1038/nature03202. URL https://www.nature.com/articles/nature03202. Number: 7021 Publisher: Nature Publishing Group.

J. Mohr, B. Mathiesen, and A. Evrard. Properties of the Intracluster Medium in an Ensemble of Nearby Galaxy Clusters. *Astrophysical Journal*, 517:627–649, 1999.

F. Murtagh and A. Heck. Principal Components Analysis. In *Multivariate Data Analysis*, volume 131 of *Astrophysics and Space Science Library*. Springer, Dordrecht, 1987. ISBN 978-90-277-2426-7. URL https://doi.org/10.1007/978-94-009-3789-5_2.

D. Nagai, A. V. Kravtsov, and A. Vikhlinin. Effects of Galaxy Formation on Thermodynamics of the Intracluster Medium. *The Astrophysical Journal*, 668(1):1–14, Oct. 2007. ISSN 0004-637X, 1538-4357. doi: 10.1086/521328. URL https://iopscience.iop.org/article/10.1086/521328.

M. Ntampaka, H. Trac, D. J. Sutherland, S. Fromenteau, B. Póczos, and J. Schneider. DYNAMICAL MASS MEASUREMENTS OF CONTAMINATED GALAXY CLUSTERS USING MACHINE LEARNING. *The Astrophysical Journal*, 831(2):135, Nov. 2016. ISSN 1538-4357. doi: 10.3847/0004-637X/831/2/135. URL http://stacks.iop.org/0004-637X/831/i=2/a=135?key=crossref.671245e938e94d6e6c9acec6946a910f.

M. Ntampaka, J. ZuHone, D. Eisenstein, D. Nagai, A. Vikhlinin, L. Hernquist, F. Marinacci, D. Nelson, R. Pakmor, A. Pillepich, P. Torrey, and M. Vogelsberger. A Deep Learning Approach to Galaxy Cluster X-ray Masses. *The Astrophysical Journal*, 876(1):82, May 2019. ISSN 1538-4357. doi: 10.3847/1538-4357/ab14eb. URL http://arxiv.org/abs/1810.07703. arXiv: 1810.07703.

M. Oey and R. Kennicutt. Abundances of HII regions in early-type spiral galaxies. *Astrophysical Journal*, 411:137–152, 1993.

D. Osterbrock and G. Ferland. *Astrophysics of gaseous nebulae and active galactic nuclei*. University Science Books, Sausalito, CA USA, 1 edition, 1989.

S. P. O'Sullivan and D. C. Gabuzda. Magnetic field strength and spectral distribution of six parsec-scale active galactic nuclei jets. *Monthly Notices of the Royal Astronomical Society*, 400(1):26–42, Nov. 2009. ISSN 0035-8711. doi: 10.1111/j.1365-2966.2009.15428.x. URL https://academic.oup.com/mnras/article/400/1/26/1066948. Publisher: Oxford Academic.

Z. J. Pace, C. Tremonti, Y. Chen, A. L. Schaefer, M. A. Bershady, K. B. Westfall, M. Boquien, K. Rowlands, B. Andrews, J. R. Brownstein, N. Drory, and D. Wake. Resolved and Integrated Stellar Masses in the SDSS-IV/MaNGA Survey. II. Applications of PCA-based Stellar Mass Estimates. *The Astrophysical Journal*, 883(1):83, Sept. 2019. ISSN 1538-4357. doi: 10.3847/1538-4357/ab3726. URL https://iopscience.iop.org/article/10.3847/1538-4357/ab3726.

J. R. Peterson and A. C. Fabian. X-ray Spectroscopy of Cooling Clusters. *Physics Reports*, 427(1):1–39, Apr. 2006. ISSN 03701573. doi: 10.1016/j.physrep.2005.12.007. URL http://arxiv.org/abs/astro-ph/0512549. arXiv: astro-ph/0512549.

E. M. d. G. D. Pino. The Role of Magnetic Fields on Astrophysical Jets. *AIP Conference Proceedings*, 784:183–194, 2005. ISSN 0094243X. doi: 10.1063/1.2077183. URL http://arxiv.org/abs/astro-ph/0505521. arXiv: astro-ph/0505521.

P. P. Plucinsky, A. Bogdan, H. L. Marshall, and N. W. Tice. The Complicated Evolution of the ACIS Contamination Layer over the Mission Life of the Chandra X-ray Observatory. *Space Telescopes and Instrumentation 2018: Ultraviolet to Gamma Ray*, page 226, July 2018. doi: 10.1117/12.2312748. URL http://arxiv.org/abs/1809.02225. arXiv: 1809.02225.

J. R. Quinlan. Induction of decision trees. *Machine Learning*, 1(1):81–106, Mar. 1986. ISSN 0885-6125, 1573-0565. doi: 10.1007/BF00116251. URL http://link.springer.com/10.

1007/BF00116251.

D. A. Rafferty, B. R. McNamara, P. E. J. Nulsen, and M. W. Wise. The Feedback-Regulated Growth of Black Holes and Bulges through Gas Accretion and Starbursts in Cluster Central Dominant Galaxies. *The Astrophysical Journal*, 652(1):216–231, Nov. 2006. ISSN 0004-637X, 1538-4357. doi: 10.1086/507672. URL http://arxiv.org/abs/astro-ph/0605323. arXiv: astro-ph/0605323.

C. S. Reynolds, M. C. D. Marsh, H. R. Russell, A. C. Fabian, R. N. Smith, F. Tombesi, and S. Veilleux. Astrophysical limits on very light axion-like particles from Chandra grating spectroscopy of NGC 1275. *The Astrophysical Journal*, 890(1):59, Feb. 2020. ISSN 1538-4357. doi: 10.3847/1538-4357/ab6a0c. URL http://arxiv.org/abs/1907.05475. arXiv: 1907.05475.

S. Ronen, A. Aragón-Salamanca, and O. Lahav. Principal component analysis of synthetic galaxy spectra. *Monthly Notices of the Royal Astronomical Society*, 303(2):284–296, Feb. 1999. ISSN 0035-8711, 1365-2966. doi: 10.1046/j.1365-8711.1999.02222.x. URL https://academic.oup.com/mnras/article-lookup/doi/10.1046/j.1365-8711.1999.02222.x.

V. Rubin. Dark Matter in Spiral Galaxies. *Scientific American*, 248(6):96–109, 1983.

A. J. R. Sanderson, E. O'Sullivan, T. J. Ponman, and). A statistically-selected Chandra sample of 20 galaxy clusters – II. Gas properties and cool-core/non-cool core bimodality. *Monthly Notices of the Royal Astronomical Society*, 395(2):764–776, May 2009. ISSN 00358711, 13652966. doi: 10.1111/j.1365-2966.2009.14613.x. URL http://arxiv.org/abs/0902.1747. arXiv: 0902.1747.

K. Schwarzschild. Über das Gravitationsfeld eines Massenpunktes nach der Einsteinschen Theorie. *Sitzungsberichte der Deutschen Akademie der Wissenschaften zu Berlin, Klasse fur Mathematik, Physik, und Technik*, page 189, 1916.

A. A. Sokolov and I. M. Ternov. Synchrotron radiation. *Akademia Nauk SSSR, Moskovskoie Obshchestvo Ispytatelei prirody. Sektsia Fiziki. Sinkhrotron Radiation, Nauka Eds., Moscow, 1966 (Russian title: Sinkhrotronnoie izluchenie), 228 pp.*, Aug. 1966. URL http://adsabs.harvard.edu/abs/1966siiz.book.....S.

P.-N. Tan, M. Steinbach, and V. Kumar. *Introduction to Data Mining*. Addison-Wesley Longman Publishing Co., Inc., Boston, Ma, USA, first edition, 2005.

L. M. Voigt and A. C. Fabian. Galaxy cluster mass profiles. *Monthly Notices of the Royal Astronomical Society*, 368(2):518–533, May 2006. ISSN 0035-8711, 1365-2966. doi: 10.1111/j.1365-2966.2006.10199.x. URL https://academic.oup.com/mnras/article-lookup/doi/10.1111/j.1365-2966.2006.10199.x.

A. Wandel. The Eddington ratio of active galactic nuclei in accretion-disk and dynamical models. *Astronomy & Astrophysics*, 241:5–14, 1991.

M. C. Weisskopf, H. D. Tananbaum, L. P. Van Speybroeck, and S. L. O'Dell. Chandra X-Ray Observatory (CXO):Overview. *arXiv:astro-ph/0004127*, pages 2–16, July 2000. doi: 10.1117/12.391545. URL http://arxiv.org/abs/astro-ph/0004127. arXiv: astro-ph/0004127.

M. C. Weisskopf, B. Brinkman, C. Canizares, G. Garmire, S. Murray, and L. P. Van Speybroeck. An Overview of the Performance and Scientific Results from the Chandra X-Ray Observatory (CXO). *Publications of the Astronomical Society of the Pacific*, 114(791):1–24, Jan. 2002. ISSN 0004-6280, 1538-3873. doi: 10.1086/338108. URL http://arxiv.org/abs/astro-ph/0110308. arXiv: astro-ph/0110308.

N. White and S. Holt. Accretion Disk Coronae. *Astrophysical Journal*, 257:318–337, 1982.

H.-Y. K. Yang and C. S. Reynolds. How AGN Jets Heat the Intracluster Medium – Insights from Hydrodynamic Simulations. *The Astrophysical Journal*, 829(2):90, Sept. 2016. ISSN 1538-4357. doi: 10.3847/0004-637X/829/2/90. URL http://arxiv.org/abs/1605.01725. arXiv: 1605.01725.

E. Zackrisson. Quasars and Low Surface Brightness Galaxies as Probes of Dark Matter, 2005. URL https://www.researchgate.net/publication/237788999_Quasars_and_Low_Surface_Brightness_Galaxies_as_Probes_of_Dark_Matte.

Chapitre 2

Evidence of runaway gas cooling in the absence of supermassive black hole feedback at the epoch of cluster formation

J. Hlavacek-Larrondo,[1] C.L. Rhea,[1] T. Webb,[2] M. McDonald,[3] A. Muzzin,[4] G. Wilson,[5] K. Finner,[6] F.Valin,[2] N. Bonaventura,[7] M. Cooper,[8] A.C. Fabian,[9], M.-L. Gendron-Marsolais,[10] J.M. Jee,[6 11] C. Lidman,[12] M. Mezcua,[13 14] A. Noble,[15] H.R. Russell,[9 16] J. Surace,[17] A. Trudeau,[18] H.K.C. Yee,[19]

[1] *Département de physique, Université de Montréal, C.P. 6128 Succ. Centre-ville, Montréal H3C 3J7, Canada*

[2] *Department of Physics, McGill University, Montréal, Québec, CA*

[3] *Kavli Institute for Astrophysics and Space Research, Massachusetts Institute of Technology, 77 Massachusetts Avenue, Cambridge, MA 02139, USA*

[4] *York University, 4700 Keele Street, Toronto, ON, M3J 1P3, Canada*

[5] *Department of Physics and Astronomy, University of California Riverside, 900 University Avenue, Riverside, CA 92521, USA*

[6] *Yonsei University, Department of Astronomy, Seoul, Korea*

[7] *Niels Bohr Institute, University of Copenhagen, Copenhagen 172100*

[8] *Center for Cosmology, Department of Physics & Astronomy, 4129 Reines Hall, University of California, Irvine, CA 92697, USA*

[9] *Institute of Astronomy, Madingley Road, Cambridge CB3 0HA*

[10] *European Southern Observatory, Alonso de Cordova 3107, Vitacura, Casilla 19001, Santiago, Chile*

[11] *Department of Physics, University of California, Davis, California, USA*

[12] *The Research School of Astronomy and Astrophysics, Australian National University, ACT 2601, Australia*

[13] *Institute of Space Sciences (ICE, CSCIC), Campus UAB, Carrer de Can Magrans, 08193, Barcelona, Spain*
[14] *Institut d'Estudis Espacials de Catalunya (IEEC), Gran Capita, 08034 Barcelona, Spain*
[15] *Arizona State University, School of Earth and Space Exploration, Tempe, AZ 871404, USA*
[16] *School of Physics and Astronomy, University of Nottingham, Nottingham NG7 2RD, UK*
[17] *Infrared Processing & Analysis Center, MS 100-22, California Institute of Technology, Pasadena, CA, 91125, USA*
[18] *Department of Physics & Astronomy, University of Victoria, 3800 Finnerty Road, Victoria, British Columbia, V8W 2Y2, Canada*
[19] *Department of Astronomy and Astrophysics, University of Toronto, 50 St George Street, Toronto, Ontario M5S 3H4, Canada*

Cet article a été accepté dans *The Astrophysical Journal Letters* (ApJL) le 10 Mai 2020. Il est aussi l'objet d'un communiqué de presse de la NASA.

Mots-clés: Milieu intra-amas, écoulement de refroidissement, rétroaction, lumière intra-amas

Abstract

Cosmological simulations, as well as mounting evidence from observations, have shown that supermassive black holes play a fundamental role in regulating the formation of stars throughout cosmic time. This has been clearly demonstrated in the case of galaxy clusters in which powerful feedback from the central black hole is preventing the hot intracluster gas from cooling catastrophically, thus reducing the expected star formation rates by orders of magnitude. These conclusions have however been almost entirely based on nearby clusters. Based on new Chandra X-ray observations, we present the first observational evidence for massive, runaway cooling occurring in the absence of supermassive black hole feedback in the high-redshift galaxy cluster SpARCS104922.6+564032.5 ($z = 1.709$). The hot intracluster gas appears to be fueling a massive burst of star formation (≈ 900 $M_{\odot}yr^{-1}$) that is offset by dozens of kpc from the central galaxy. The burst is co-spatial with the coolest intracluster gas but not associated with any galaxy in the cluster. In less than 100 million years, such runaway cooling can form the same amount of stars as in the Milky Way. Intracluster stars are therefore not only produced by tidal stripping and the disruption of cluster galaxies, but can also be produced by runaway cooling of hot intracluster gas at early times. Overall,

these observations show the dramatic impact when supermassive black hole feedback fails to operate in clusters. They indicate that in the highest overdensities such as clusters and proto-clusters, runaway cooling may be a new and important mechanism for fueling massive bursts of star formation in the early universe.

Keywords: Intra Cluster Medium, Cooling Flow, AGN Feedback, Intracluster Light

2.1. Introduction

Galaxy clusters are extremely massive structures that contain hundreds to thousands of galaxies, a substantial dark matter component and a large quantity of hot intracluster gas. At extreme temperatures of tens of millions of degrees, the central density of the hot gas in many clusters is so high, that it is expected to cool down to temperatures of ≈30 K in less than a few hundred million years (e.g. Peterson, Fabian 2006). Once cooled, this gas should deposit itself onto the central dominant galaxy, known as the brightest cluster galaxy (BCG), and extreme star formation rates (SFRs) of hundreds to thousands of solar masses per year are expected (e.g. Fabian 1994). However, observations have shown that the observed SFRs are orders of magnitude lower. We now understand that it is the supermassive black hole (SMBH) in the BCG that is preventing the hot intracluster gas from cooling by driving supersonic jets that carve out gigantic X-ray cavities (see a review by McNamara, Nulsen 2012), a process known as mechanical active galactic nucleus (AGN) feedback.

However, most of our understanding of AGN feedback in clusters has been based on nearby objects and it has remained observationnally challenging to determine if such feedback is also occurring in distant clusters (e.g. Hlavacek-Larrondo et al. 2012; Hlavacek-Larrondo et al. 2015; Bîrzan et al. 2017). This is due to the fact that nearby clusters are more easily studied given their proximity, but also because of the lack of well-understood samples of high-redshift clusters.

The situation has now dramatically changed with the advent of new cluster surveys. Combined with extensive follow-up Chandra observations, the 2500 deg^2 SPT cluster survey (Vanderlinde et al. 2010, Reichardt et al. 2013) has proven to be a key player for our understanding of cluster evolution at $z > 1$ (e.g. Rossetti et al. 2017; McDonald et al. 2017; McDonald et al. 2016a) and showed that powerful mechanical AGN feedback has been operating in at least some clusters since $z \approx 1$; Hlavacek-Larrondo et al. 2015).

The SpARCS cluster and Stellar Bump Sequence surveys have also discovered over 500 $z > 0.6$ clusters in the Spitzer SWIRE fields (e.g. Wilson et al. 2009; Muzzin et al. 2009; Muzzin et al. 2013). Webb et al. (2015b) showed that beyond z≈1, significant in situ star formation seems to be occurring at the cores of clusters. This is in direct contrast to what is seen in the local universe, in which the central AGN is preventing star formation from

occurring. Using the SPT sample, McDonald et al. (2016b) found a similar result. Both studies suggest that beyond z≈1, the star formation in BCGs may be driven by gas-rich major mergers instead of residual cooling flows. These conclusions were motivated by the change in slope of the specific SFR (sSFR) with redshift and one case study of an apparent gas-rich BCG merger in the cluster SpARCS104922.6+564032.5 (hereafter SpARCS1049; Webb et al. 2015a).

2.1.1. SpARCS104922.6+564032.5

SpARCS1049 was first identified in 2015 as an optically rich system located at $z = 1.709$ with 27 spectroscopically confirmed members (Webb et al. 2015a). It has a richness-estimated mass within 500 kpc of $3.8 \pm 1.2 \times 10^{14} M_{\odot}$, placing it at an extremely important epoch in which the most massive structures in the universe were forming.

A recent weak-lensing analysis of the cluster based on infrared Hubble Space Telescope (HST) observations confirms its high-mass of $3.5 \pm 1.2 \times 10^{14} M_{\odot}$ and suggests that the cluster has no significant substructure (Finner et al. 2020). The HST observations also revealed an unusual long (≈60 kpc) tidal-like feature in the core of the cluster that was thought to originate from a gas-rich major merger given its morphology and that it was found to coincide with an extreme infrared source ($L_{\rm IR} = 6.2 \pm 0.9 \times 10^{12} L_{\odot}$; Webb et al. 2015a). Spitzer infrared spectrograph observations found that the infrared source was also coincident with polycyclic aromatic hydrocarbons features at the redshift of the cluster (Farrah et al. 2007), indicating that the emission was dominated by star formation and not from an accreting SMBH. Overall, these observations showed that the cluster core appears to host an extreme starburst with a (AGN-corrected) SFR of 860 ± 130 $M_{\odot} yr^{-1}$ (Webb et al. 2015a; Webb et al. 2015b).

The only other cluster known to host such an extreme starburst at its core is SPT-CL J2344-4243, i.e. the Phoenix cluster located at $z = 0.597$ with a SFR of $500-800$ $M_{\odot} yr^{-1}$ (McDonald et al. 2012 and references therein). In this case, extreme AGN feedback is occurring (as seen from X-ray cavities, radio jets and a central quasar), but it appears to be insufficient to suppress cooling of the hot intracluster gas (McDonald et al. 2019).

However, in the case of SpARCS1049, the 24 micron Spitzer MIPS emission was unusual and appeared to be offset by ≈25 kpc from the central galaxy and not associated with any other cluster member (in direct contrast to the star formation occurring in the Phoenix cluster). Such features may have suggested that the intense star bursting occurring in SpARCS1049 is being driven by a merger-like event, but an extremely large molecular gas reservoir of $1.1 \pm 0.1 \times 10^{11}$ $M_{\odot}$ was also detected in the core (Webb et al. 2017) and showed no signs of multiple velocity peaks as would be expected in a major-merger event (Greve et al. 2005; Gao et al. 2001; Schulz et al. 2007). Recently, these features were also

interpreted as evidence of ram pressure stripping occurring in the cluster core (Castignani et al. 2020).

Here, we present the first X-ray observations of SpARCS1049 (PI Hlavacek-Larrondo). We show that X-rays provide a key missing piece of the puzzle: they reveal that the starburst is directly linked to the intracluster gas and consisted with being fueled by massive runaway cooling of a cool core. This is in direct contrast to what is seen in nearby clusters and indicates that runaway cooling may be a new and important mechanism for fueling massive bursts of star formation in the early universe for the highest overdensities. In Section 2, we present the observations. In Section 3, we discuss the results and in Section 4 their implications. Throughout this paper, we assume $H_0 = 70$ km s^{-1} Mpc^{-1}, $\Omega_m = 0.3$ and $\Omega_\Lambda = 0.7$. All errors are 1σ.

2.2. Observations and Data Reduction

2.2.1. Chandra X-ray Observations

The first X-ray observations of SpARCS1049 were obtained with ACIS onboard the Chandra X-ray Observatory (PI Hlavacek-Larrondo). The object was observed in 2018 for 170 ks (ObsIDs 20528, 20941, 20940 and 21129). All observations were centered on ACIS-I3. The data were reduced using CIAO v4.11. Due to the low counts and extended nature of the object, we did not follow the standard reduction pipeline. Instead, we constructed a level 2 event file while mimicking the steps of several other authors with the goal of maximizing the number of counts of our source (Broos et al. 2010; Weißmann et al. 2013). After correcting for the initial astrometric alignment, we used the task lc_sigma_clip to investigate the presence of major flares, but no event above 3σ was detected. We then used destreak to clear the event file of residual streaks. In creating the bad-pixel file, we used a custom bitflag which allowed us to retain more counts in the diffuse regions. In the final step, we executed the acis_process_events with check_vf_pha set to yes to further maximise the counts. An exposure map assuming a monoenergetic photon distribution at 1.53 keV, corresponding to the peak expected for a massive cluster at $z \approx 1.7$, was used to create the merged, background-subtracted and exposure-corrected image shown in Figure 2.1. We note that we also ran the standard reduction pipeline developed by the Chandra X-ray Center. The cluster is detected in both cases and the results of this paper remain unchanged, but our tailored pipeline allows us to maximize the cluster counts.

2.2.1.1. *Astrometric Corrections*

The HST frames were initially aligned for co-addition using the Drizzle package. Source Extractor was then used to extract sources in the HST images (7 stars were found) and a

script was built to match these sources to those in a reference catalog. We use Gaia as the reference catalog and found a systematic offset of the matched stars of RA$= 0.5 \pm 0.1$" and Dec$= -0.2 \pm 0.1$". The offset was applied to shift the WCS of the HST images. The accuracy depends on the reference frame, which in this case is ≈ 0.1". We then examined the Chandra X-ray images and found that half a dozen galaxies detected in the HST images had bright X-ray point sources associated with them (presumably from the central AGN). They were all systematically offset by $0.25''$ to the south east. We re-aligned the X-ray images and use these throughout this work.

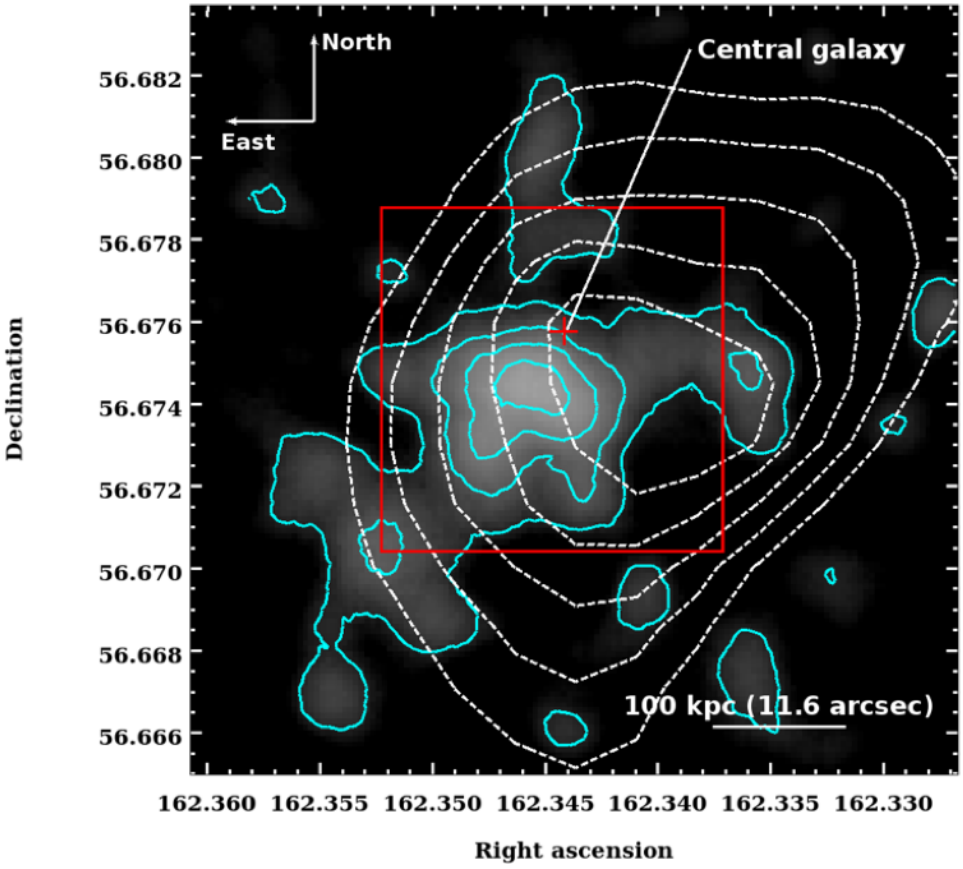

Fig. 2.1. Merged exposure-corrected, background-subtracted $0.5 - 7.0$ keV Chandra X-ray image of SpARCS1049. The image has not been binned, but smoothed with a Gaussian function of $\sigma = 5$ pixels. In cyan, there are 4 contours starting at 4σ where σ is the neighboring value outside the cluster. The BCG is also shown with the red cross symbol (see Webb et al. 2015a for method of identification). The X-ray emission is highly peaked and consistent with a compact cool core that is offset from the central galaxy. The white dashed contours show the weak lensing mass reconstruction (Finner et al. 2020). The red box is the zoomed-in region of Figure 2.4.

2.2.1.2. *Photometric and Spectroscopic Analysis*

The data were spectroscopically fit using Xspec v12.10.1, Sherpa v1, and python v3.5. Given the low count rate, we could not constrain the redshift of the X-ray source and assumed $z = 1.709$ (Webb et al. 2015a, Webb et al. 2017; see also Appendix A for evidence that the X-ray source is indeed associated with the cluster). We also could not constrain the metallicity and assumed a ratio of 0.3 (e.g. Anders, Grevesse 1989; Arnaud, Raymond 1992; Bulbul et al. 2012; Molendi et al. 2016; McDonald et al. 2016a). Note that we re-derived all quantities using a ratio of 0.2 and found consistent results. We used a fixed value of $n_H = 5.99 \times 10^{19}\mathrm{cm}^2$ (Kalberla et al. 2005). The background region was chosen to be off-chip at > 1 Mpc. We also considered a blank sky background and found consistent results. We fit each observation's source and background regions simultaneously. We modeled the background emission following the methods of Sun et al. (2009) and McDonald et al. (2017). Both methods replicate the soft and hard excesses observed in the cosmic X-ray background. We found consistent results and opted to use the McDonald model so that we can directly compare our results with theirs. This model includes a soft X-ray Galactic component (APEC, $kT = 0.18$keV, Z$= 0$) and a hard cosmic X-ray component (BREMSS, $kT = 40$keV). To account for the cluster emission, we considered the APEC and MEKAL models and found consistent results. All values quoted hereafter have been derived with APEC. Since we are in a low-count regime, we also use c-statistic and conduct all fits using a single count $0.6-5.0$ keV range. We find that the target has an integrated rest-frame $2-10$ ∼keV X-ray luminosity of $4.29\pm0.19\times10^{44}$ ∼erg/s and a temperature of 5.71 ± 1.57 ∼keV within 200 kpc of the peak X-ray emission. The overall morphology is compact and reminiscent of a relaxed galaxy cluster with a mild elongation in the north-west to south-east direction. The X-ray surface brightness concentration ($\mathrm{C_{SB}} = 0.19^{+0.07}_{-0.05}$), defined as the ratio between the energy flux within 40 kpc and within 400 kpc in the 0.5 to 2.0 keV band, indicates that SpARCS1049 has an overdense core (i.e. a cool core). It is one of the few known clusters with an overdense core at $z > 1.5$ (e.g. McDonald et al. 2017). In Figure 2.2, we show the deprojected density profile as a function of radius normalized by $\mathrm{R_{500}}$, compared to the high-redshift SPT clusters. Profiles were determined following the methods of Vikhlinin et al. (2006), Andersson et al. (2011), and McDonald et al. (2013). We refer the reader to these papers for the details. Following this method, we find $\mathrm{R_{500}}$ to be ≈450 kpc for SpARCS1049. This value is consistent with the expected $\mathrm{R_{500}}$ value from the weak-lensing mass estimate (≈600 kpc). Figure 2.2 shows that the deprojected density profile is highly peaked with a central density ($n_{e,0} = 0.07\mathrm{cm}^{-3}$) that is again indicative of a cool core. Here, central electron density divides cool cores and non cool cores at $\mathrm{n}_{e,0} = 0.015$ (e.g. Hudson et al. 2010; McDonald et al. 2013). We note that the profile beyond ≈ 50kpc follows a different slope compared to other clusters; implying that the outer parts of the cluster, usually driven by self-similar processes, may not yet be

well established in this cluster. Cool cores may therefore form before self-similar processes are established in the outer regions of clusters (e.g. Vikhlinin et al. 2006; Croston et al. 2008; Mantz et al. 2015), although deeper observations are needed to confirm this result. Figure 2.3 compares the sSFR in SpARCS1049 to the SPT clusters. Here, we extracted

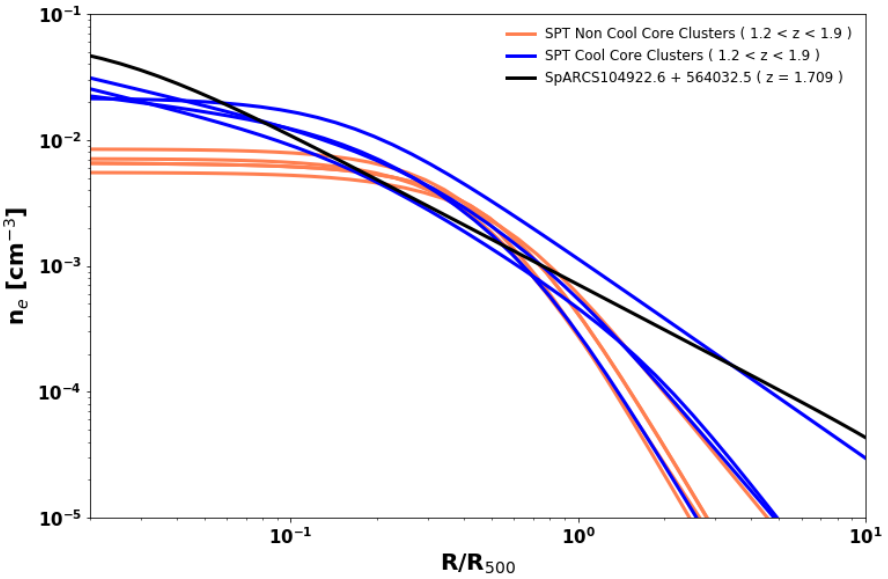

Fig. 2.2. Deprojected electron density profile of SpARCS1049 assuming spherical geometry and scaled for R_{500} (black curve). Profiles of the eight $1.2 < z < 1.9$ SPT clusters of galaxies that have Chandra X-ray observations are also shown (see McDonald et al. 2017 for details). The top 4 are cool core clusters as defined by they central electron density value. This figure shows that SpARCS1049 has an over dense core (i.e. a cool core).

the redshifts and positions of the BCGs from McDonald et al. (2016a). X-ray centroids were taken from McDonald et al. (2013). With these positions, we used astropy's separation function to calculate the projected offset between these two quantities. We then extracted all the available values for the SFR of the BCGs (UV, O[II], 24 microns). For sources with only detections, we proceeded to calculate the average of these values to have a representative value of the SFR. For systems with detections in one or multiple bands, but upper limits in the others, we only considered the average of the detections. Finally, for the sources with only upper limits, we calculated the average and treated this as an upper limit. To calculate the sSFR, we divided the SFR by the BCG stellar masses. We further subdivided the clusters according to the value of their central deprojected electron density ($n_{e,0}$). For SpARCS1049, the SFR and BCG stellar mass were taken from Webb et al. (2015a). The X-ray centroid was determined using the iterative procedure of Cavagnolo et al. (2009), and includes an statistical error based on the ciao tools.

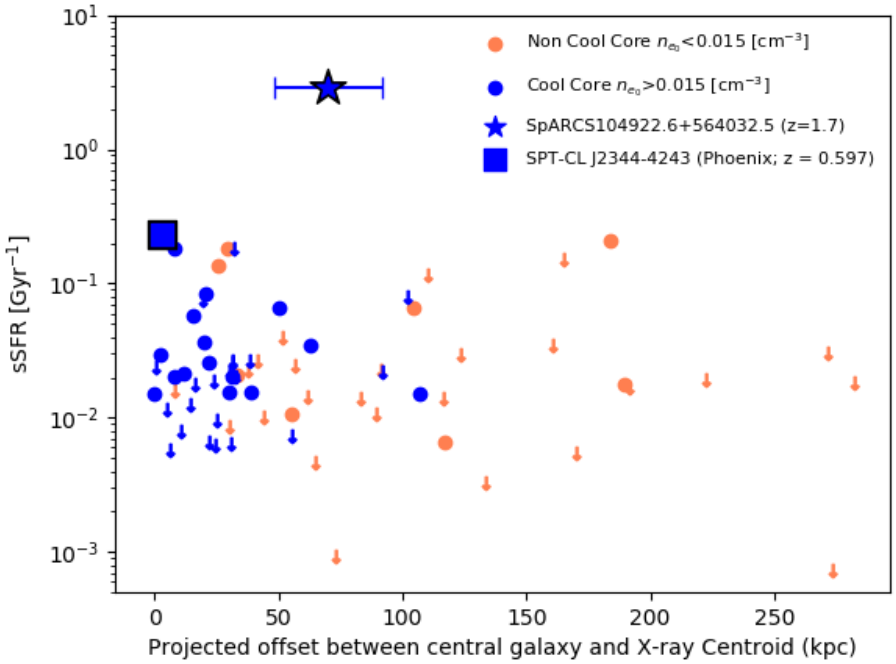

Fig. 2.3. Comparison of the star formation processes occurring in SpARCS1049 to those occurring in the SPT galaxy clusters. The plot shows the sSFR as a function of the projected distance between the BCG and the centroid of the cluster X-ray emission. The clusters are color-coded depending on the central value of their deprojected electron density profile.

2.2.2. VLA Observations

New Q-band observations with the the Very Large Array (VLA) were obtained in 2019 for SpARCS1049 (18B-177; PI Webb). These observations probe the redshifted CO(1-0) line. We briefly summarize the data reduction procedure (the details will be presented in Valin et al. in prep). The C-configuration was chosen to maximize the detection, while allowing for high enough spatial resolution to resolve the molecular gas (beam of $\approx 0.47'' \approx 4$ kpc). The observations were completed in optimal conditions and the data were reduced following the standard CASA procedure (v5.4.2-5). Figure 2.4 presents the resulting continuum image ranging from 42.456 GHz to 42.616 GHz obtained with tclean. Contours start at $2\sigma_{\rm rms}$, where $\sigma_{\rm rms} = 45.7$ μJy/beam.

2.3. Discussion

2.3.1. Runaway Gas Cooling as the Source of the Starburst

In Figure 2.4, we show contours highlighting the coolest intracluster gas detectable with Chandra ($0.7 - 1.0$ keV) starting at 4σ, where σ is the neighbouring value outside of the

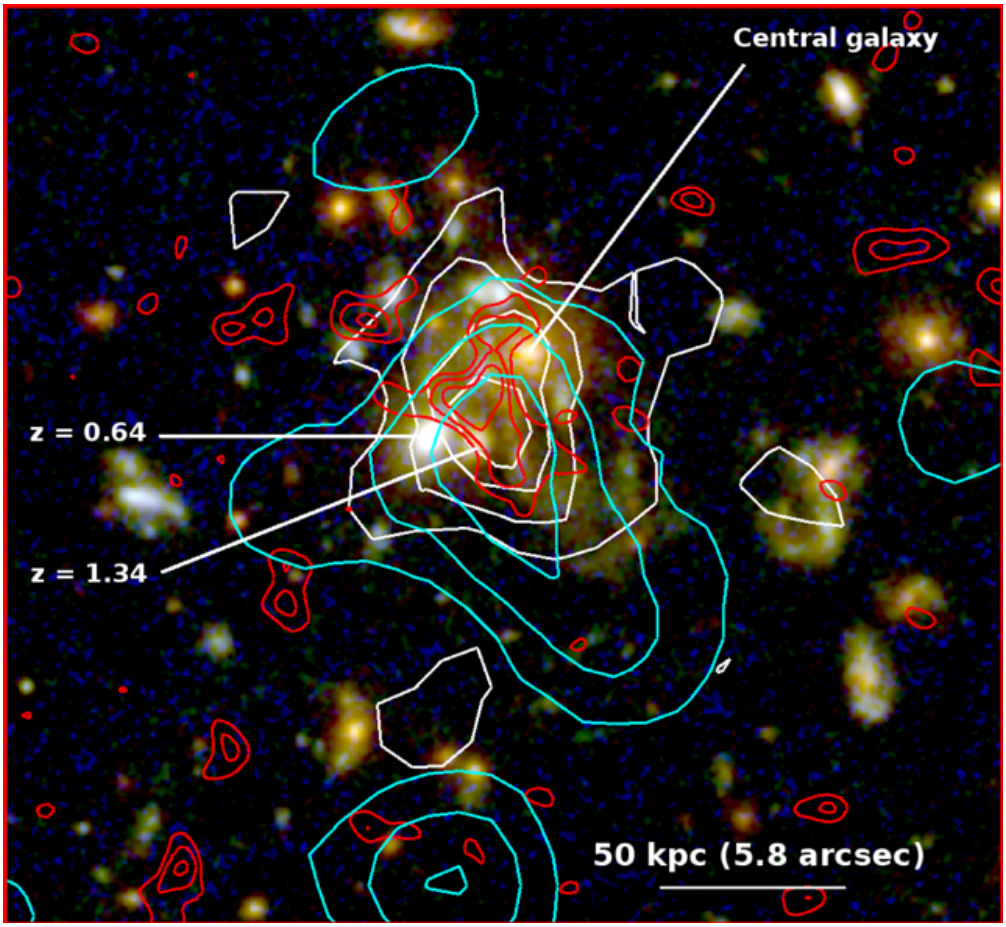

Fig. 2.4. HST color-composite image of the cluster core using the F160W, F150W and F814W filters (same region as the red square in Figure 2.1). The cyan contours show the $0.7 - 1.0$ keV X-ray emission of the cluster used to highlight the coolest X-ray gas that Chandra can detect, starting at 4σ. We show the new VLA CO (1-0) emission with the red contours and Spitzer MIPS 24 micron emission with white contours (Valin et al. in prep and Webb et al. 2015a). The MIPS emission peaks on the tidal-like feature seen in the HST images and is slightly extended along the direction of this tail. The MIPS emission is also consistent with the location of the coolest X-ray gas. This image shows that the location of the coolest intracluster gas is co-spatial with the location of the star formation in SpARCS1049.

cluster. This gas is located near the peak of the X-ray emission and is remarkably co-spatial with the large, ≈ 60 kpc tidal-like feature seen in the HST images (Webb et al. 2015a).

The tidal-like feature was initially thought to originate from a gas-rich major merger occurring in the cluster core given its morphology and that it was found to coincide with the starburst (860 ± 130 $M_{\odot}$ yr^{-1}; Webb et al. 2015a; Webb et al. 2015b). It was unusual given that the 24 micron MIPS centroid was significantly offset (≈ 25 kpc) from the BCG or any other cluster member (see Figure 2.4), indicating that the intense star formation was not associated with any galaxy. The narrow spectral signature of the large molecular gas

reservoir in the cluster core ($1.1 \pm 0.1 \times 10^{11}$ $M_{\odot}$; Webb et al. 2017) was also in direct contrast to what is expected from a major merger (e.g. Greve et al. 2005; Gao et al. 2001; Schulz et al. 2007). Instead, the velocity dispersion of the molecular gas matches the dispersion seen in nearby clusters of galaxies in which a small fraction of the intracluster gas is cooling (McNamara et al. 2014; Russell et al. 2014; Gonzalez et al. 2005).

Here, by imaging the cluster for the first time at X-ray wavelengths, we find that the cluster harbours a cool core and that the coolest intracluster gas is directly co-spatial with the HST tidal-like feature. Our new VLA observations also show that the HST tidal-like feature and cool X-ray gas are co-spatial with the CO (1-0) gas. This co-spatiality indicates that the intense infrared source, HST tidal-like feature and molecular gas reservoir must be intimately linked to the hot intracluster gas. We do not expect any merger event or ram pressure stripping event to also contain cool X-ray gas associated with the star formation. Instead, we interpret these results as evidence that the intense starburst occurring in the cluster core is likely being fueled by massive, runaway cooling of the intracluster gas. Only a moderate cool core would be required to fuel a starburst of $\approx 900 M_{\odot}$ yr^{-1} if allowed to cool completely (e.g. Fabian 1994).

At low-redshift, the SFR seen in the cores of cool core clusters are typically 1% of the expected rates (Peterson, Fabian 2006; O'Dea et al. 2008; McDonald et al. 2018). This is because the SMBH in the BCG is preventing these hot halos from cooling via powerful mechanical jetted outflows that inflate large X-ray cavities (McNamara, Nulsen 2012; Fabian 2012) and only allowing a small fraction of residual cooling to occur. In the case of SpARCS1049, there is no evidence that the SMBH in the BCG is actively accreting : the central galaxy is barely radio-detected and shows no evidence of jetted outflows (Trudeau et al. 2019); we find no evidence of an X-ray point source (indicating the presence of an accreting SMBH) coincident with the central galaxy; and the optical and infrared photometry of the central galaxy shows that it is quiescent. These observations are therefore consistent with runaway cooling of the hot halo occurring because of the absence of feedback from the central galaxy.

2.3.2. A Cool Core Offset from Its Central Galaxy

In Section 2.2.1.2, we showed that both the X-ray surface brightness coefficient and deprojected central electron density place the cluster in the cool core category.

The X-ray emission is however slightly elongated in the south-east to north-west direction (see Figure 2.1), indicating that the cluster may be undergoing a minor merger that has not destroyed the cool core (see e.g. A2146 for an example of a cool core that survived a bullet-like merger; Russell et al. 2012). A merger scenario could also explain the ≈ 25 kpc offset between the coolest intracluster gas and BCG and the ≈ 50 kpc offset between the X-ray

peak and BCG (Figures 2.1 and 2.4), although in nearby clusters of galaxies, such large offsets are usually associated with major mergers (Hudson et al. 2010; Rossetti et al. 2017).

Hamer et al. (2012) identified 3 systems (out of 77 nearby line-emitting BCGs) in which the soft X-ray peak was displaced from the BCG. The soft X-ray peak was also coincident with optical line emission, similar to what is occurring in SpARCS1049 although of very different scales. Indeed, the observed offset between the BCG and the peak H_α emission was at most $\approx$10 kpc versus $\approx$ 25 kpc in SpARCS1049. The authors argued that such displacements may be caused by a large event such as a major merger (see also Pasini et al. 2019 and Vantyghem et al. 2019). However, it is important to remember that SpARCS1049 is located at the epoch in which the most massive structures (such as SpARCS1049) are still forming and have not yet settled into equilibrium. It is therefore unclear if such direct comparisons to nearby clusters can be applied to clusters located at $z \approx 1.7$. Detailed simulations are required to determine if such displacements (and cool core survival) are possible in cluster mergers at the epoch of cluster formation.

2.4. Implications

2.4.1. The Failure of AGN Feedback

In nearby clusters of galaxies, it has been argued that AGN feedback might form a self-regulated loop in which the jetted outflows trigger instabilities which allow a fraction of the hot gas to cool and rain down onto the central SMBH, re-starting the feedback loop (e.g. Gaspari et al. 2013; Voit et al. 2015; Tremblay et al. 2016). This is consistent with the fact that at low-redshifts, the cool cores are usually centered on the BCGs and that these can directly fuel the central SMBH.

In SpARCS1049, the coolest X-ray gas (and starburst) is offset by $\approx$ 25 kpc from the BCG and the X-ray peak is offset by almost 50 kpc from the BCG. Given this displacement, the absence of feedback in SpARCS1049 might therefore be caused by a lack of gas supply onto the central SMBH. If gas can not be funnelled down to the central SMBH, then it implies that the central SMBH may not be accreting enough material to power a jet, let alone a jet powerful enough to offset cooling of a cool core. This is in agreement with the recent study of Trudeau et al. (2019) that found no evidence of radio jets associated with the BCG in SpARCS1049. If this is the reason why runaway gas cooling is occurring in SpARCS1049, our results imply that the self-regulated feedback loop *requires* cool cores to be spatially aligned with the BCG. It also implies that the central SMBH must be directly fueled by the hot halos.

2.4.2. Star Formation in High-redshift Clusters and Protoclusters

Figure 2.3 shows that the star formation occurring in the core of SpARCS1049 is orders of magnitude higher than what is seen at low-redshifts. Given that SpARCS1049 is located at the epoch of cluster formation, our results indicate that runaway cooling of intracluster gas can be an important process of star formation in the highest overdensities (i.e. clusters and proto-clusters) at high-redshift. At the very least, our results imply that some of the intense star formation occurring in newly identified clusters and proto-clusters at high-redshift (e.g. Capak et al. 2011; Chiang et al. 2017) may be driven by runaway gas cooling as opposed to galaxy merger processes.

2.4.3. A New Mechanism for Building Intracluster Stars

Our results show that runaway cooling can deposit a tremendous amount of newly formed stars in the cores of clusters. In fact, in less than 100 million years, this cooling can form the same amount of stars as in the Milky Way. Consequently, our results directly imply that intracluster stars are not only produced by tidal stripping and the disruption of cluster galaxies (Gregg, West 1998; Conroy et al. 2007), but can also be produced early on in the cluster life through massive cooling of the intracluster gas. This is consistent with recent studies suggesting the these stars are already in place at $z > 1$ (e.g. Ko, Jee 2018), implying that runaway cooling of the hot halos can account for part of the intracluster light in clusters (Lin, Mohr 2004; Conroy et al. 2007). Another consequence is that this process appears to be capable of depositing the newly formed stars over dozens of kpc, i.e. the entire cluster core. Runaway gas cooling can therefore easily distribute intracluster stars over large distances.

2.5. Concluding Remarks

Overall, our results directly illustrate the fate of hot X-ray halos when SMBH feedback fails to operate, a process thought to be commonly occurring at cosmic dawn when galaxies were first forming (e.g. Cattaneo et al. 2009). They directly imply that star formation processes in the early Universe may not only be driven by the classical merger and disc scenarios, but may also be driven by runaway gas cooling in the highest overdensities.

J. H.-L. acknowledges support from NSERC via the Discovery grant program, as well as the Canada Research Chair program. C. R. acknowledges financial support from the physics department of the Université de Montréal. GW acknowledges support from the National Science Foundation through grant AST-1517863, by HST program number GO-15294, and by grant number 80NSSC17K0019 issued through the NASA Astrophysics Data Analysis Program (ADAP). Support for program number GO-15294 was provided by NASA through a grant from the Space Telescope Science Institute, which is operated by the Association of

Universities for Research in Astronomy, Incorporated, under NASA contract NAS5-26555. We also greatly thank the anonymous referees that provided the first reports when submitted to the initial journal. AT is supported by the NSERC Postgraduate Scholarship-Doctoral Program.

Appendix A: Origin of the X-ray Emission

The X-ray source detected at the location of SpARCS1049 extends over 30" ($\approx$ 250 kpc at $z = 1.709$) in diameter as traced by the 4σ contours (see Fig. 2.1), entirely consistent with the X-ray emission originating from a $\approx 10^{14} M_{\odot}$ cluster located at $z \approx 1.7$. The X-ray luminosity and temperature of the source also fall right along the scaling relations expected for galaxy clusters (e.g. Anderson et al. 2015). The X-ray source cannot be X-ray emission originating from a population of X-ray binaries in the starbursting core as this emission would be two orders of magnitude lower for typical X-ray luminosity to star formation ratios, even in low-metallicity environments. If the X-ray emission originated from a background source, then the only structure that could explain the large X-ray luminosity of $\geq 10^{44}$ erg s^{-1}, extended morphology and high temperature would be another massive cluster located at $z >> 1.7$. It is statistically unlikely to have two large over densities overlap each other within such a small region. In addition, Webb et al. (2015) carried out a campaign of near-infrared (NIR) spectroscopy with MOSFIRE on Keck on the field in which SpARCS1049 is located. This was combined with a literature search for redshifts from other instruments. It was found that the most massive structure at $z \approx 1.3 - 2.0$ is the $z = 1.709$ cluster. Since then, new GMOS Gemini observations were obtained (PI Webb). These new grating observations trace the full redshift range in a single mask at $0.3 < z < 1.7$ within $2.5'$ of the X-ray detection. We probed the [OII] emission over the redshift range $0.3 < z < 1.7$ and placed slits on many tens of galaxies. In principle, if the X-rays were associated with a structure at lower redshift, based on the implied X-ray luminosity of the detected X-ray source, we would expect much more than 10 galaxies within this radius of the X-ray centroid to have concurrent redshifts. We targeted emission line galaxies for their efficiency at yielding redshifts. These data revealed no new structure peaks along the line of sight. We therefore conclude that the X-ray source identified at the location of SpARCS1049 must be associated with SpARCS1049.

References

Anders Edward, Grevesse Nicolas. Abundances of the elements: Meteoritic and solar // Geochimica et Cosmochimica Acta. I 1989. 53, 1. 197–214.

Anderson M. E., Gaspari M., White S. D. M., Wang W., Dai X. Unifying X-ray scaling relations from galaxies to clusters // Monthly Notices of the Royal Astronomical Society. IV 2015. 449, 4. 3806–3826.

Andersson K., Benson B. A., Ade P. A. R., Aird K. A., Armstrong B., Bautz M., Bleem L. E., Brodwin M., Carlstrom J. E., Chang C. L., Crawford T. M., Crites A. T., Haan T. de, Desai S., Dobbs M. A., Dudley J. P., Foley R. J., Forman W. R., Garmire G., George E. M., Gladders M. D., Halverson N. W., High F. W., Holder G. P., Holzapfel

W. L., Hrubes J. D., Jones C., Joy M., Keisler R., Knox L., Lee A. T., Leitch E. M., Lueker M., Marrone D. P., McMahon J. J., Mehl J., Meyer S. S., Mohr J. J., Montroy T. E., Murray S. S., Padin S., Plagge T., Pryke C., Reichardt C. L., Rest A., Ruel J., Ruhl J. E., Schaffer K. K., Shaw L., Shirokoff E., Song J., Spieler H. G., Stalder B., Staniszewski Z., Stark A. A., Stubbs C. W., Vanderlinde K., Vieira J. D., Vikhlinin A., Williamson R., Yang Y., Zahn O., Zenteno A. X-RAY PROPERTIES OF THE FIRST SUNYAEV-ZEL'DOVICH EFFECT SELECTED GALAXY CLUSTER SAMPLE FROM THE SOUTH POLE TELESCOPE // The Astrophysical Journal. IX 2011. 738, 1. 48.

Arnaud M, Raymond J. Iron Ionization and Recombination Rates and Ionization Equilibrium // Astrophysical Journal. 1992. 398. 394–406.

Broos Patrick S., Townsley Leisa K., Feigelson Eric D., Getman Konstantin V., Bauer Franz E., Garmire Gordon P. INNOVATIONS IN THE ANALYSIS OF *CHANDRA* - ACIS OBSERVATIONS // The Astrophysical Journal. V 2010. 714, 2. 1582–1605.

Bulbul G. Esra, Smith Randall K., Foster Adam, Cottam Jean, Loewenstein Michael, Mushotzky Richard, Shafer Richard. HIGH-RESOLUTION *XMM-NEWTON* SPECTROSCOPY OF THE COOLING FLOW CLUSTER A3112 // The Astrophysical Journal. III 2012. 747, 1. 32.

Bîrzan L., Rafferty D. A., Brüggen M., Intema H. T. A Study of High-redshift AGN Feedback in SZ Cluster Samples // Monthly Notices of the Royal Astronomical Society. X 2017. 471, 2. 1766–1787. arXiv: 1706.04775.

Capak Peter L., Riechers Dominik, Scoville Nick Z., Carilli Chris, Cox Pierre, Neri Roberto, Robertson Brant, Salvato Mara, Schinnerer Eva, Yan Lin, Wilson Grant W., Yun Min, Civano Francesca, Elvis Martin, Karim Alexander, Mobasher Bahram, Staguhn Johannes G. A massive proto-cluster of galaxies at a redshift of z {\approx} 5.3 // Nature. II 2011. 470, 7333. 233–235. arXiv: 1101.3586.

Castignani G., Combes F., Salomé P. Environmental processing in cluster core galaxies at $z = 1.7$ // Astronomy & Astrophysics. III 2020. 635. L10.

Cattaneo A., Faber S. M., Binney J., Dekel A., Kormendy J., Mushotzky R., Babul A., Best P. N., Brueggen M., Fabian A. C., Frenk C. S., Khalatyan A., Netzer H., Mahdavi A., Silk J., Steinmetz M., Wisotzki L. The role of black holes in galaxy formation and evolution // Nature. VII 2009. 460, 7252. 213–219. arXiv: 0907.1608.

AN ENTROPY THRESHOLD FOR STRONG Ha AND RADIO EMISSION IN THE CORES OF GALAXY CLUSTERS. // . 2009. 683. 4.

Chiang Yi-Kuan, Overzier Roderik A., Gebhardt Karl, Henriques Bruno. Galaxy Protoclusters as Drivers of Cosmic Star Formation History in the First 2 Gyr // The Astrophysical Journal. VII 2017. 844, 2. L23.

Conroy Charlie, Wechsler Risa H., Kravtsov Andrey V. The Hierarchical Build-Up of Massive Galaxies and the Intracluster Light since z=1 // The Astrophysical Journal. X 2007. 668,

2. 826–838. arXiv: astro-ph/0703374.

Croston J. H., Pratt G. W., Böhringer H., Arnaud M., Pointecouteau E., Ponman T. J., Sanderson A. J. R., Temple R. F., Bower R. G., Donahue M. Galaxy-cluster gas-density distributions of the representative *XMM-Newton* cluster structure survey (REXCESS) // Astronomy & Astrophysics. VIII 2008. 487, 2. 431–443.

Fabian A.C. Cooling Flows in Clusters of Galaxies // Annual Review of Astronomy and Astrophysics. 1994. 32. 277–318.

Fabian A.C. Observational Evidence of Active Galactic Nuclei Feedback // Annual Review of Astronomy and Astrophysics. 2012. 50, 1. 455–489. _eprint: https://doi.org/10.1146/annurev-astro-081811-125521.

Farrah D., Bernard-Salas J., Spoon H. W. W., Soifer B. T., Armus L., Brandl B., Charmandaris V., Desai V., Higdon S., Devost D., Houck J. High resolution mid-infrared spectroscopy of ultraluminous infrared galaxies // The Astrophysical Journal. IX 2007. 667, 1. 149–169. arXiv: 0706.0513.

Finner K., Jee J., Webb T., Wilson G., Perlmutter P. // Astrophysical Journal. 2020. Submitted.

Gao Yu, Lo K.Y., Lee S.-W., Lee T.-H. Molecular Gas and the Modest Star Formation Efficiency in the "Antennae" Galaxy: ARP 244=NCG4038/9 // Astrophysical Journal. 2001. 548. 172–189.

Gaspari M., Ruszkowski M., Oh S. Peng. Chaotic cold accretion onto black holes // Monthly Notices of the Royal Astronomical Society. VII 2013. 432, 4. 3401–3422. arXiv: 1301.3130.

Gonzalez Anthony H., Zabludoff Ann I., Zaritsky Dennis. Intracluster Light in Nearby Galaxy Clusters: Relationship to the Halos of Brightest Cluster Galaxies // The Astrophysical Journal. I 2005. 618, 1. 195–213.

Gregg Michael D., West Michael J. Galaxy Disruption as the Origin of Intracluster Light in the Coma Cluster // Nature. XII 1998. 396, 6711. 549–552. arXiv: astro-ph/9812033.

Greve T. R., Bertoldi F., Smail Ian, Neri R., Chapman S. C., Blain A. W., Ivison R. J., Genzel R., Omont A., Cox P., Tacconi L., Kneib J.-P. An interferometric CO survey of luminous submillimetre galaxies // Monthly Notices of the Royal Astronomical Society. V 2005. 359, 3. 1165–1183.

Hamer S. L., Edge A. C., Swinbank A. M., Wilman R. J., Russell H. R., Fabian A. C., Sanders J. S., Salomé P. The relation between line emission and brightest cluster galaxies in three exceptional clusters: evidence for gas cooling from the intracluster medium: Offset optical line emission in cluster cores // Monthly Notices of the Royal Astronomical Society. IV 2012. 421, 4. 3409–3417.

Hlavacek-Larrondo J., Fabian A. C., Edge A. C., Ebeling H., Sanders J. S., Hogan M. T., Taylor G. B. Extreme AGN feedback in the MAssive Cluster Survey: a detailed study of X-ray cavities at *z>0.3*: *X-ray cavities in the MACS cluster sample* // Monthly Notices

of the Royal Astronomical Society. IV 2012. 421, 2. 1360–1384.

Hlavacek-Larrondo J., McDonald M., Benson B. A., Forman W. R., Allen S. W., Bleem L. E., Ashby M. L. N., Bocquet S., Brodwin M., Dietrich J. P., Jones C., Liu J., Reichardt C. L., Saliwanchik B. R., Saro A., Schrabback T., Song J., Stalder B., Vikhlinin A., Zenteno A. X-RAY CAVITIES IN A SAMPLE OF 83 SPT-SELECTED CLUSTERS OF GALAXIES: TRACING THE EVOLUTION OF AGN FEEDBACK IN CLUSTERS OF GALAXIES OUT TO $z = 1.2$ // The Astrophysical Journal. V 2015. 805, 1. 35.

Hudson D. S., Mittal R., Reiprich T. H., Nulsen P. E. J., Andernach H., Sarazin C. L. What is a cool-core cluster? a detailed analysis of the cores of the X-ray flux-limited *HIFLUGCS* cluster sample // Astronomy and Astrophysics. IV 2010. 513. A37.

Kalberla P. M. W., Burton W. B., Hartmann Dap, Arnal E. M., Bajaja E., Morras R., Pöppel W. G. L. The Leiden/Argentine/Bonn (LAB) Survey of Galactic HI: Final data release of the combined LDS and IAR surveys withimproved stray-radiation corrections // Astronomy & Astrophysics. IX 2005. 440, 2. 775–782.

Ko Jongwan, Jee M. James. Evidence for the Existence of Abundant Intracluster Light at $z = 1.24$ // The Astrophysical Journal. VII 2018. 862, 2. 95.

Lin Yen-Ting, Mohr Joseph J. K-band Properties of Galaxy Clusters and Groups: Brightest Cluster Galaxies and Intracluster Light // The Astrophysical Journal. XII 2004. 617, 2. 879–895. arXiv: astro-ph/0408557.

Mantz Adam B., Allen Steven W., Morris R. Glenn, Schmidt Robert W., Linden Anja von der, Urban Ondrej. Cosmology and astrophysics from relaxed galaxy clusters – I. Sample selection // Monthly Notices of the Royal Astronomical Society. V 2015. 449, 1. 199–219.

McDonald M., Allen S. W., Bayliss M., Benson B. A., Bleem L. E., Brodwin M., Bulbul E., Carlstrom J. E., Forman W. R., Hlavacek-Larrondo J., Garmire G. P., Gaspari M., Gladders M. D., Mantz A. B., Murray S. S. The Remarkable Similarity of Massive Galaxy Clusters from z 0 to z 1.9 // The Astrophysical Journal. VI 2017. 843, 1. 28.

McDonald M., Bayliss M., Benson B. A., Foley R. J., Ruel J., Sullivan P., Veilleux S., Aird K. A., Ashby M. L. N., Bautz M., Bazin G., Bleem L. E., Brodwin M., Carlstrom J. E., Chang C. L., Cho H. M., Clocchiatti A., Crawford T. M., Crites A. T., Haan T. de, Desai S., Dobbs M. A., Dudley J. P., Egami E., Forman W. R., Garmire G. P., George E. M., Gladders M. D., Gonzalez A. H., Halverson N. W., Harrington N. L., High F. W., Holder G. P., Holzapfel W. L., Hoover S., Hrubes J. D., Jones C., Joy M., Keisler R., Knox L., Lee A. T., Leitch E. M., Liu J., Lueker M., Luong-Van D., Mantz A., Marrone D. P., McMahon J. J., Mehl J., Meyer S. S., Miller E. D., Mocanu L., Mohr J. J., Montroy T. E., Murray S. S., Natoli T., Padin S., Plagge T., Pryke C., Rawle T. D., Reichardt C. L., Rest A., Rex M., Ruhl J. E., Saliwanchik B. R., Saro A., Sayre J. T., Schaffer K. K., Shaw L., Shirokoff E., Simcoe R., Song J., Spieler H. G., Stalder B., Staniszewski

Z., Stark A. A., Story K., Stubbs C. W., Šuhada R., Engelen A. van, Vanderlinde K., Vieira J. D., Vikhlinin A., Williamson R., Zahn O., Zenteno A. A massive, cooling-flow-induced starburst in the core of a luminous cluster of galaxies // Nature. VIII 2012. 488, 7411. 349–352.

McDonald M., Benson B. A., Vikhlinin A., Stalder B., Bleem L. E., Lin H. W., Aird K. A., Ashby M. L. N., Bautz M. W., Bayliss M., Bocquet S., Brodwin M., Carlstrom J. E., Chang C. L., Cho H. M., Clocchiatti A., Crawford T. M., Crites A. T., Haan T. de, Desai S., Dobbs M. A., Dudley J. P., Foley R. J., Forman W. R., George E. M., Gettings D., Gladders M. D., Gonzalez A. H., Halverson N. W., High F. W., Holder G. P., Holzapfel W. L., Hoover S., Hrubes J. D., Jones C., Joy M., Keisler R., Knox L., Lee A. T., Leitch E. M., Liu J., Lueker M., Luong-Van D., Mantz A., Marrone D. P., McMahon J. J., Mehl J., Meyer S. S., Miller E. D., Mocanu L., Mohr J. J., Montroy T. E., Murray S. S., Nurgaliev D., Padin S., Plagge T., Pryke C., Reichardt C. L., Rest A., Ruel J., Ruhl J. E., Saliwanchik B. R., Saro A., Sayre J. T., Schaffer K. K., Shirokoff E., Song J., Suhada R., Spieler H. G., Stanford S. A., Staniszewski Z., Stark A. A., Story K., Engelen A. van, Vanderlinde K., Vieira J. D., Williamson R., Zahn O., Zenteno A. The Growth of Cool Cores and Evolution of Cooling Properties in a Sample of 83 Galaxy Clusters at $0.3 < z < 1.2$ Selected from the SPT-SZ Survey // The Astrophysical Journal. VIII 2013. 774, 1. 23. arXiv: 1305.2915.

McDonald M., Bulbul E., Haan T. de, Miller E. D., Benson B. A., Bleem L. E., Brodwin M., Carlstrom J. E., Chiu I., Forman W. R., Hlavacek-Larrondo J., Garmire G. P., Gupta N., Mohr J. J., Reichardt C. L., Saro A., Stalder B., Stark A. A., Vieira J. D. The Evolution of the Intracluster Medium Metallicity in Sunyaev-Zel'dovich-Selected Galaxy Clusters at $0 < z < 1.5$ // The Astrophysical Journal. VII 2016a. 826, 2. 124. arXiv: 1603.03035.

McDonald M., Gaspari M., McNamara B. R., Tremblay G. R. Revisiting the Cooling Flow Problem in Galaxies, Groups, and Clusters of Galaxies // The Astrophysical Journal. V 2018. 858, 1. 45. arXiv: 1803.04972.

McDonald M., McNamara B. R., Voit G. M., Bayliss M., Benson B. A., Brodwin M., Canning R. E. A., Florian M. K., Garmire G. P., Gaspari M., Gladders M. D., Hlavacek-Larrondo J., Kara E., Reichardt C. L., Russell H. R., Saro A., Sharon K., Somboonpanyakul T., Tremblay G. R., Weeren R. J. van. Anatomy of a Cooling Flow: The Feedback Response to Pure Cooling in the Core of the Phoenix Cluster // The Astrophysical Journal. X 2019. 885, 1. 63. arXiv: 1904.08942.

McDonald M., Stalder B., Bayliss M., Allen S. W., Applegate D. E., Ashby M. L. N., Bautz M., Benson B. A., Bleem L. E., Brodwin M., Carlstrom J. E., Chiu I., Desai S., Gonzalez A. H., Hlavacek-Larrondo J., Holzapfel W. L., Marrone D. P., Miller E. D., Reichardt C. L., Saliwanchik B. R., Saro A., Schrabback T., Stanford S. A., Stark A. A., Vieira J. D., Zenteno A. Star-Forming Brightest Cluster Galaxies at $0.25 < z < 1.25$:

A Transitioning Fuel Supply // The Astrophysical Journal. I 2016b. 817, 2. 86. arXiv: 1508.06283.

McNamara B. R., Nulsen P. E. J. Mechanical Feedback from Active Galactic Nuclei in Galaxies, Groups, and Clusters // New Journal of Physics. V 2012. 14, 5. 055023. arXiv: 1204.0006.

McNamara B. R., Russell H. R., Nulsen P. E. J., Edge A. C., Murray N. W., Main R. A., Vantyghem A. N., Combes F., Fabian A. C., Salome P., Kirkpatrick C. C., Baum S. A., Bregman J. N., Donahue M., Egami E., Hamer S., O'Dea C. P., Oonk J. B. R., Tremblay G., Voit G. M. A 10 ^{10} SOLAR MASS FLOW OF MOLECULAR GAS IN THE A1835 BRIGHTEST CLUSTER GALAXY // The Astrophysical Journal. III 2014. 785, 1. 44.

Molendi S., Eckert D., De Grandi S., Ettori S., Gastaldello F., Ghizzardi S., Pratt G. W., Rossetti M. A critical assessment of the metal content of the intracluster medium // Astronomy & Astrophysics. II 2016. 586. A32.

Muzzin Adam, Marchesini Danilo, Stefanon Mauro, Franx Marijn, McCracken Henry J., Milvang-Jensen Bo, Dunlop James S., Fynbo J. P. U., Brammer Gabriel, Labbe Ivo, Dokkum Pieter van. The Evolution of the Stellar Mass Functions of Star-Forming and Quiescent Galaxies to z = 4 from the COSMOS/UltraVISTA Survey // The Astrophysical Journal. X 2013. 777, 1. 18. arXiv: 1303.4409.

Muzzin Adam, Wilson Gillian, Yee H. K. C., Hoekstra Henk, Gilbank David, Surace Jason, Lacy Mark, Blindert Kris, Majumdar Subhabrata, Demarco Ricardo, Gardner Jonathan P., Gladders Mike, Lonsdale Carol. SPECTROSCOPIC CONFIRMATION OF TWO MASSIVE RED-SEQUENCE-SELECTED GALAXY CLUSTERS AT z 1.2 IN THE SpARCS-NORTH CLUSTER SURVEY // The Astrophysical Journal. VI 2009. 698, 2. 1934–1942.

AN INFRARED SURVEY OF BRIGHTEST CLUSTER GALAXIES. II. WHY ARE SOME BRIGHTEST CLUSTER GALAXIES FORMING STARS? // . 2008. 681, 2. 11.

Pasini Thomas, Gitti Myriam, Brighenti Fabrizio, Temi Pasquale, Amblard Alexandre, Hamer Stephen, Ettori Stefano, O'Sullivan Ewan, Gastaldello Fabio. A BCG with offset cooling: is the AGN feedback cycle broken in A2495? // The Astrophysical Journal. XI 2019. 885, 2. 111. arXiv: 1910.05363.

Peterson J. R., Fabian A. C. X-ray Spectroscopy of Cooling Clusters // Physics Reports. IV 2006. 427, 1. 1–39. arXiv: astro-ph/0512549.

Reichardt C. L., Stalder B., Bleem L. E., Montroy T. E., Aird K. A., Andersson K., Armstrong R., Ashby M. L. N., Bautz M., Bayliss M., Bazin G., Benson B. A., Brodwin M., Carlstrom J. E., Chang C. L., Cho H. M., Clocchiatti A., Crawford T. M., Crites A. T., Haan T. de, Desai S., Dobbs M. A., Dudley J. P., Foley R. J., Forman W. R., George E. M., Gladders M. D., Gonzalez A. H., Halverson N. W., Harrington N. L., High F. W., Holder G. P., Holzapfel W. L., Hoover S., Hrubes J. D., Jones C., Joy M., Keisler R., Knox L., Lee A. T., Leitch E. M., Liu J., Lueker M., Luong-Van D., Mantz A., Marrone

D. P., McDonald M., McMahon J. J., Mehl J., Meyer S. S., Mocanu L., Mohr J. J., Murray S. S., Natoli T., Padin S., Plagge T., Pryke C., Rest A., Ruel J., Ruhl J. E., Saliwanchik B. R., Saro A., Sayre J. T., Schaffer K. K., Shaw L., Shirokoff E., Song J., Spieler H. G., Staniszewski Z., Stark A. A., Story K., Stubbs C. W., Suhada R., Engelen A. van, Vanderlinde K., Vieira J. D., Vikhlinin A., Williamson R., Zahn O., Zenteno A. Galaxy clusters discovered via the Sunyaev-Zel'dovich effect in the first 720 square degrees of the South Pole Telescope survey // The Astrophysical Journal. I 2013. 763, 2. 127. arXiv: 1203.5775.

Rossetti M., Gastaldello F., Eckert D., Della Torre M., Pantiri G., Cazzoletti P., Molendi S. The cool core state of Planck SZ-selected clusters versus X-ray selected samples: evidence for cool core bias // Monthly Notices of the Royal Astronomical Society. VI 2017. 468, 2. 1917–1930. arXiv: 1702.06961.

Russell H. R., McNamara B. R., Edge A. C., Nulsen P. E. J., Main R. A., Vantyghem A. N., Combes F., Fabian A. C., Murray N., Salome P., Wilman R. J., Baum S. A., Donahue M., O'Dea C. P., Oonk J. B. R., Tremblay G. R., Voit G. M. Massive molecular gas flows in the Abell 1664 brightest cluster galaxy // The Astrophysical Journal. III 2014. 784, 1. 78. arXiv: 1309.0014.

Russell H. R., McNamara B. R., Sanders J. S., Fabian A. C., Nulsen P. E. J., Canning R. E. A., Baum S. A., Donahue M., Edge A. C., King L. J., O'Dea C. P. Shock fronts, electron-ion equilibration and ICM transport processes in the merging cluster Abell 2146 // Monthly Notices of the Royal Astronomical Society. VI 2012. 423, 1. 236–255. arXiv: 1202.5320.

Schulz A., Henkel C., Muders D., Mao R. Q., Roellig M., Mauersberger R. The interstellar medium of the Antennae Galaxies // Astronomy & Astrophysics. V 2007. 466, 2. 467–479. arXiv: astro-ph/0702341.

Sun M., Voit G. M., Donahue M., Jones C., Forman W., Vikhlinin A. CHANDRA STUDIES OF THE X-RAY GAS PROPERTIES OF GALAXY GROUPS // The Astrophysical Journal. III 2009. 693, 2. 1142–1172.

Tremblay Grant R., Oonk J. B. Raymond, Combes Françoise, Salomé Philippe, O'Dea Christopher P., Baum Stefi A., Voit G. Mark, Donahue Megan, McNamara Brian R., Davis Timothy A., McDonald Michael A., Edge Alastair C., Clarke Tracy E., Galván-Madrid Roberto, Bremer Malcolm N., Edwards Louise O. V., Fabian Andrew C., Hamer Stephen L., Li Yuan, Maury Anaëlle, Russell Helen R., Quillen Alice C., Urry C. Megan, Sanders Jeremy S., Wise Michael. Cold, clumpy accretion onto an active supermassive black hole // Nature. VI 2016. 534, 7606. 218–221. arXiv: 1606.02304.

Trudeau Ariane, Webb Tracy, Hlavacek-Larrondo Julie, Noble Allison, Gendron-Marsolais Marie-Lou, Lidman Christopher, Mezcua Mar, Muzzin Adam, Wilson Gillian, Yee H. K. C. Multiwavelength radio observations of a Brightest Cluster Galaxy at z=1.71:

Detection of a modest Active Galactic Nucleus and evidence for extended star formation // Monthly Notices of the Royal Astronomical Society. VII 2019. 487, 1. 1210–1217. arXiv: 1905.05875.

Vanderlinde K., Crawford T. M., Haan T. de, Dudley J. P., Shaw L., Ade P. A. R., Aird K. A., Benson B. A., Bleem L. E., Brodwin M., Carlstrom J. E., Chang C. L., Crites A. T., Desai S., Dobbs M. A., Foley R. J., George E. M., Gladders M. D., Hall N. R., Halverson N. W., High F. W., Holder G. P., Holzapfel W. L., Hrubes J. D., Joy M., Keisler R., Knox L., Lee A. T., Leitch E. M., Loehr A., Lueker M., Marrone D. P., McMahon J. J., Mehl J., Meyer S. S., Mohr J. J., Montroy T. E., Ngeow C.-C., Padin S., Plagge T., Pryke C., Reichardt C. L., Rest A., Ruel J., Ruhl J. E., Schaffer K. K., Shirokoff E., Song J., Spieler H. G., Stalder B., Staniszewski Z., Stark A. A., Stubbs C. W., Engelen A. van, Vieira J. D., Williamson R., Yang Y., Zahn O., Zenteno A. Galaxy Clusters Selected with the Sunyaev-Zel'dovich Effect from 2008 South Pole Telescope Observations // The Astrophysical Journal. X 2010. 722, 2. 1180–1196. arXiv: 1003.0003.

Vantyghem A. N., McNamara B. R., Russell H. R., Edge A. C., Nulsen P. E. J., Combes F., Fabian A. C., McDonald M., Salomé P. An Enormous Molecular Gas Flow in the RX J0821+0752 Galaxy Cluster // The Astrophysical Journal. I 2019. 870, 2. 57.

Vikhlinin A., Kravtsov A., Forman W., Jones C., Markevitch M., Murray S. S., Van Speybroeck L. Chandra sample of nearby relaxed galaxy clusters: mass, gas fraction, and mass-temperature relation // The Astrophysical Journal. IV 2006. 640, 2. 691–709. arXiv: astro-ph/0507092.

Voit G. M., Donahue M., Bryan G. L., McDonald M. Regulation of star formation in giant galaxies by precipitation, feedback, and conduction // Nature. III 2015. 519, 7542. 203–206. arXiv: 1409.1598.

Webb Tracy, Noble Allison, DeGroot Andrew, Wilson Gillian, Muzzin Adam, Bonaventura Nina, Cooper Mike, Delahaye Anna, Foltz Ryan, Lidman Chris, Surace Jason, Yee H. K. C., Chapman Scott, Dunne Loretta, Geach James, Hayden Brian, Hildebrandt Hendrik, Huang Jiasheng, Pope Alexandra, Smith Matthew W. L., Perlmutter Saul, Tudorica Alex. AN EXTREME STARBURST IN THE CORE OF A RICH GALAXY CLUSTER AT $z = 1.7$ // The Astrophysical Journal. VIII 2015a. 809, 2. 173.

Webb Tracy M. A., Lowenthal James, Yun Min, Noble Allison G., Muzzin Adam, Wilson Gillian, Yee H. K. C., Cybulski Ryan, Aretxaga I., Hughes D. H. Detection of a Substantial Molecular Gas Reservoir in a Brightest Cluster Galaxy at $z = 1.7$ // The Astrophysical Journal. VII 2017. 844, 2. L17.

Webb Tracy M. A., Muzzin Adam, Noble Allison, Bonaventura Nina, Geach James, Hezevah Yashar, Lidman Chris, Wilson Gillian, Yee H. K. C., Surace Jason, Shupe David. THE STAR FORMATION HISTORY OF BCGs TO $z = 1.8$ FROM THE SpARCS/SWIRE

SURVEY: EVIDENCE FOR SIGNIFICANT IN SITU STAR FORMATION AT HIGH REDSHIFT // The Astrophysical Journal. VI 2015b. 814, 2. 96.

Weißmann A., Böhringer H., Šuhada R., Ameglio S. Studying the properties of galaxy cluster morphology estimators // Astronomy & Astrophysics. I 2013. 549. A19.

Wilson Gillian, Muzzin Adam, Yee H. K. C., Lacy Mark, Surace Jason, Gilbank David, Blindert Kris, Hoekstra Henk, Majumdar Subhabrata, Demarco Ricardo, Gardner Jonathan P., Gladders Michael D., Lonsdale Carol. SPECTROSCOPIC CONFIRMATION OF A MASSIVE RED-SEQUENCE-SELECTED GALAXY CLUSTER AT $z = 1.34$ IN THE SpARCS-SOUTH CLUSTER SURVEY // The Astrophysical Journal. VI 2009. 698, 2. 1943–1950.

Chapitre 3

A Novel Machine Learning Approach to Disentangle Multi-Temperature Regions in Galaxy Clusters

C.L. Rhea,[1] J. Hlavacek-Larrondo,[1] L. Perreault-Levasseur,[1] M.-L. Gendron-Marsolais,[2] Ralph Kraft, [3]

[1]*Département de physique, Université de Montréal, C.P. 6128 Succ. Centre-ville, Montréal H3C 3J7, Canada*
[2]*European Southern Observatory, Alonso de Córdova 3107, Vitacura, Casilla 19001, Santiago, Chile*
[3]*Smithsonian Astrophysical Observatory, Cambridge, MA 02138, USA*

Cet article a été soumis à la revue *The Astrophysical Journal* (ApJ) le 15 Mai 2020.
Des corrections mineures ont été demandées le 8 juillet.

Mots-clés: Spectres en rayons X, milieu intra-amas, amas de galaxies, analyse de composantes principales, forêt aléatoire.

Abstract

The hot intra-cluster medium (ICM) surrounding the heart of galaxy clusters is a complex medium comprised of various emitting components. Although previous studies of nearby galaxy clusters, such as the Perseus, the Coma, or the Virgo cluster, have demonstrated the need for multiple thermal components when spectroscopically fitting the ICM's X-ray

emission, no systematic methodology for calculating the number of underlying components currently exists. In turn, underestimating or overestimating the number of components can cause systematic errors in the emission parameter estimations. In this paper, we present a novel approach to determining the number of components using an amalgam of machine learning techniques. Synthetic spectra containing a various number of underlying thermal components were created using well-established tools available from the *Chandra* X-ray Observatory. The dimensions of the training set was initially reduced using the Principal Component Analysis and then categorized based on the number of underlying components using a Random Forest Classifier. Our trained and tested algorithm was subsequently applied to *Chandra* X-ray observations of the Perseus cluster. Our results demonstrate that machine learning techniques can efficiently and reliably estimate the number of underlying thermal components in the spectra of galaxy clusters, regardless of the thermal model (MEKAL versus APEC). We also confirm that the core of the Perseus cluster contains a mix of differing underlying thermal components. We emphasize that although this methodology was trained and applied on *Chandra* X-ray observations, it is readily portable to other current (e.g. XMM-Newton, eROSITA) and upcoming (e.g. Athena, Lynx, XRISM) X-ray telescopes. The code is publicly available at `https://github.com/XtraAstronomy/Pumpkin`.

Keywords: X-ray Spectra, Intra-Cluster Medium, Galaxy Cluster, Principal Component Analysis, Random Forest

3.1. Introduction

Galaxy clusters are massive structures that contain hundreds to thousands of galaxies. These environments accommodate extremely large reservoirs of hot gas ($\sim 10^7 - 10^8$K) which constitute the intra-cluster medium (ICM; e.g. Sarazin 1986; Mushotzky 1998). Due to its elevated temperature, the ICM is a highly ionized plasma that emits primarily in the X-ray regime through the process of thermal bremmstrahlung (e.g. Markevitch, Vikhlinin 1997; Ettori, Fabian 1998; Sarazin et al. 1999; Markevitch et al. 1998). While bremmstrahlung – along with bound-free atomic transitions and the collisional excitation of hydrogen – accounts for the continuum emission, several other mechanisms contribute to the total spectra. Many prominent emission lines, such as the Fe K-α, Silicon, and Sulfer lines, are created through recombination and excitation mechanisms (e.g. see a review by Peterson, Fabian 2006). Together, the continuum and descrete line emissions create a spectrum rich in information that can be studied to better understand the properties of hot astrophysical plasmas.

The first X-ray observations of the ICM were taken fifty years ago of the Virgo, Perseus, and Coma clusters (Bradt et al. 1967; Gursky et al. 1971; Gursky 1973). Over the following thirty years, the study of extragalactic X-ray spectra was developed through the use of

orbital X-ray satellites such as *Uhuru* (e.g. Sarazin 1986), the *Einstein Observatory* (e.g. Forman et al. 1978), *EXOSAT* (e.g. Giacconi et al. 1979), and *RXTE* (e.g. Bradt et al. 1993). Since the X-rays probe the hot plasma and are emitted primarily through thermal mechanisms, X-ray spectral analysis allows us to investigate the thermodynamic parameters of the ICM. Following the launch of the *Chandra* X-ray Observatory and *XMM-Newton*, our ability to map out thermodynamic properties improved dramatically due to the increased angular, spectral resolution and effective area (e.g. Wilman, Fabian 1999; Schindler 1999; Markevitch et al. 2000; Vikhlinin et al. 2002; Mazzotta et al. 2001; Forman et al. 2002a; Forman et al. 2002b). Recent surveys using these telescopes have revealed evolution in the temperature and pressure structure of galaxy clusters which hint at a change in the galactic environment over cosmological times while revealing a lack of evolution in the metalicity(e.g. McDonald et al. 2014; Cavagnolo et al. 2008; Bocquet et al. 2015; Vikhlinin et al. 2002). In addition to learning more about the cluster environment and its evolution, understanding the plasma's thermodynamic properties allow us to put stronger constraints on cosmology such as the galactic velocity dispersion - cluster X-ray mass, X-ray Luminosity - X-ray mass, and σ_8-Ω_m (e.g. Allen et al. 2003; Allen et al. 2007; Rosati 1997; Horner et al. 1999; Tozzi, Norman 2001; Bocquet et al. 2015).

In order to access the parameters from the spectra (e.g. temperature, metallicity, pressure), researchers rely on fitting different thermal models which are dependent on the plasma's thermodynamics (e.g. David et al. 1990; Markevitch, Vikhlinin 1997; Markevitch et al. 1999). While several models have been developed to represent the X-ray emission of galaxy clusters, there are two predominant models in the literature: `APEC` (Smith et al. 2001) and `MEKAL` (Kaastra, Mewe 1993). The models primarily differ in their background database of atomic line transitions which is used during the fitting procedure. Despite their differences, it is agreed that both work well and yield similar goodness-of-fit values (e.g. Brickhouse et al. 2000; Fabian et al. 2006; Sanders et al. 2010). Additionally, recent observations have shown that different regions in a cluster may contain multiple components at different temperatures thus necessitating the use of several thermal models in the fitting procedure (e.g. Tamura et al. 2001; Kaastra et al. 2004; Plaa de et al. 2004; Frank et al. 2013 Boute 2000; Rasia et al. 2008; Lovisari, Reiprich 2019).

However, no systematic technique exists to determine the number of underlying thermal components in a given emission region. The current methodology requires users to fit multiple thermal components and accept that with the best reduced fit (e.g. Churazov et al. 2003; Fabian et al. 2006; Sanders, Fabian 2007; Fabian et al. 2011; Zhuravleva et al. 2014). While the generally accepted method – fitting more components until the fit goodness-estimator is significantly reduced – likely results in good estimates, the initial authors of the `APEC` model warn against using too many or too few components as doing so will skew the metallicity

results; this is largely because the lower temperature components will dominate the metallicity measurement since they are more line driven than the hotter components (Raymond, Smith 1977; Smith et al. 2001). Additionally, obtaining an incorrect temperature estimate due to an incorrect number of assumed underlying components leads to systematic errors in all subsequently calculated values such as the cooling time and pressure. Moreover, determining the appropriate number of underlying thermal components necessary to model the multi-phase gas allows us to probe the underlying physics accurately (e.g. Sanders, Fabian 2007; Kaastra et al. 2004).

In this paper, we present a novel method for categorizing X-ray ICM emission through the use of two machine learning techniques: principal component analysis (PCA) and random forest classification. Using these techniques, we demonstrate they can be applied to emission spectra in order to classify the number of underlying thermal components. In § 4.2, we describe the PCA method and the creation of synthetic X-ray emission spectra. The primary results of this method are reported in § 3.3 in which we thoroughly test the algorithm on the synthetic spectra. A discussion of potential limitations of the algorithm are explored in § 3.4. In § 3.5, the methodology is applied to *Chandra* X-ray observations of the Perseus cluster. We discuss the impplications of this methodology to the larger X-ray galaxy cluster community in § 3.6. We also include a short discourse on the tutorials and software packaged created so that others can adapt our techniques for their own needs in § 3.7. Throughout this paper, we adopt a standard ΛCDM cosmology defined by $H_0 = 67$ km s^{-1}Mpc^{-1} and $\Omega_M = 0.3$. We have made the code public at `https://github.com/XtraAstronomy/Pumpkin`.

3.2. Methodology and Data Reduction

3.2.1. Principal Component Analysis

PCA is a popular statistical data reduction technique that breaks down complicated relations amongst variables into their primary components (e.g. Jolliffe, Cadima 2016; Lever et al. 2017; Bro, Smilde 2014; Wold et al. 1987; Shlens 2014). More precisely, PCA is a rotation of the data to a new, orthonormal basis in which the first coordinate contains a projection of the data which maximizes the variance (the first principal component), the second contains the second greatest variance (the second principal component), and so on. This technique is akin to calculating the eigenvalues/states which is ubiquitous in other multivariate statistical techniques such as Singular Value Decomposition (SVD) or Canonical Correlation Analysis (CCA). PCA has been used extensively in the scientific literature to create lower-dimensional representations of data by projecting the initial data into a subset of the PCA components. These components account for the majority of the variance of the data and retain the structures of interest. It is a linear transformation which is often used

as a preprocessing to facilitate data classification or analysis.

$$\vec{x_i} = \vec{\mu} + \sum_{j=1}^{N} a_{ij}\vec{v_j} \tag{3.2.1}$$

Equation 3.2.1 governs the principal component analysis (see appendix A for the mathematical details). Since our work focuses on emission spectra, we describe the variables in terms of spectra. $\vec{x_i}$ represents a given spectrum, $\vec{\mu}$ represents the dataset's mean spectrum, while each $a_{ij}\vec{v_j}$ represent the eigenvalue and eigenvector (eigen-spectrum) of the decomposition (Yip et al. 2004). Most relevant to our work, several authors have applied PCA to both stellar and galactic spectra (e.g. Ronen et al. 1999; McGurk et al. 2010; Pace et al. 2019). These works have demonstrated the success of machine learning techniques in extracting emission parameters from spectra. Here, our goal is to do the same for X-ray spectra of galaxy clusters.

3.2.2. Decision Tree and Random Forest Classifier

In addition to PCA, we use the random forest classifier which builds upon the more fundamental decision tree model. These form a class of machine learning methods which are especially well-suited to classification tasks. In classification problems, data is fed into an algorithm to produce an output of interest (the class the input data belongs to). The parameters of this algorithm are learnt through a process called 'training', where the data for which the correct class is known are shown to the algorithm. During training, the values of these parameters are found by minimizing a distance, or 'cost function', between the output and the correct class.

We now discuss the training process in the specific case of the decision tree algorithm. Starting with the root data set, the algorithm must first decide how to split the root node into sub-nodes. Generally, we employ a greedy algorithm that recursively calculates the cost of a split associated with each attribute in the data set (e.g. Quinlan 1986; Tan et al. 2005; Barros et al. 2012). The algorithm then determines the split by taking the attribute-split that best minimizes the cost function. There are several cost functions available; however, they all have the same goal to create homogeneous branches (branches that have similar features). We use the Gini cost function which reduces the standard deviation within a proposed sub-node (Breiman et al. 1984). Left unchecked, this process will create unwieldy trees that overfit the data. In order to inhibit this behavior, we either set a minimum number of inputs to be placed in each leaf and/or define a maximum recursion depth. Additionally, we can prune the tree and discard nodes that have minimal importance (e.g. Mingers 1989; Song, Lu 2015). Although decision trees are easy to implement and useful in classification problems, they can suffer due to issues in the tree's variance or bias. One way to mitigate these effects is to build a random forest classifier.

Building upon the decision tree algorithm, a random forest classifier takes many individual decision trees and treats them as an ensemble. The guiding principal of the random forest classification is to create a large number of individual uncorrelated trees in order to make predictions. Classically, either a bagging – bootstrap aggregation – and/or a feature randomness algorithm are used to ensure the trees are relatively uncorrelated (e.g. Breiman 1996; Breiman 2001). For a detailed discussion of decision trees and random forest classifiers, we direct the reader to Biau (2012), Denil et al. (2014), and Fawagreh et al. (2014).

In order to properly analyse the spectra of galaxy clusters and determine the underlying physical conditions of the hot gas, it is important to calculate how many temperature components are present in a given spectra. This problem naturally translates into a poly-modal classification problem that has been explored in the scientific community using machine learning algorithms. Typical classification algorithms include support vector machines, neural networks, and the decision tree – and by extension random forest classifiers – among others. Random forest classifiers have been used successfully in recent astronomy papers (e.g. Uzeirbegovic et al. 2020; Zhang et al. 2019; Beitia-Antero et al. 2018). Therefore, we opted to utilize the standard random forest algorithm implemented in `SKLEARN`.

Although the random forest algorithm is designed to handle a single input, we must adapt it since we will often have multiple spectra of the same region. This occurs when exposures are taken at different epochs – a technique commonly employed in observational astronomy. In order to apply a random forest classifier to several spectra at once, we apply the classifier to each spectrum individually. We then leverage the definition of the classifier and sum the probabilities over the ensemble. The final classification is the class with the highest summed probability. Since each spectrum's classifier is independent, there is no notion of "simultaneous" adjustment. The author's note that having a simultaneous random forest classifier (also known as a Joint Random Forest Classifier) could be preferable; the technique is currently under development (e.g. Petralia et al. 2016).

3.2.3. Synthetic Chandra Spectra

Since our ultimate goal is to devise a systematic method to determine the number of underlying temperature components in a given X-ray spectrum, we must train our algorithm with emission spectra that contain multiple temperature components. Since this value is unknown for real observations, we construct a well-rounded set of synthetic spectra with differing emission parameters. Moreover, we choose to create synthetic *Chandra* X-ray Observatory spectra because of the telescopes un-paralleled spatial resolution which will allow us to probe smaller regions in which the number of temperature components may change. Additionally, *Chandra*'s spectral resolution provides an adequate number of emission features to train the algorithm. Although *Chandra* was chosen for this study, our application can

be ported to other missions such as *XMM-Newton* and eventually *Athena*. Finally, several observations of nearby galaxy clusters with a complex temperature structure, such as M87, Perseus, and Coma, have been completed by *Chandra*.

Synthetic spectra were created using `SHERPA's FAKE_PHA` tool. The tool requires the use of a chosen response matrix file (rmf) and ancillary response file (arf). The *Chandra* detectors have been steadily degrading each year which has lead to a consitent change in the reponse matrix. Since the observations used later in this article (see §3.5) were taken during cycle 03, we use an rmf and arf file from the same epoch. Following a discussion with the *Chandra* X-ray Obersvatory Helpdesk (private communications), we adopt the responses matrices from one of the observations of the Perseus cluster explored in later sections: ObsID 3209. The rmf and arf files were created using the `specextract` tool. The region over which we calculated the response matrix is defined in §3.5. We note that, for the present moment, in order to extend this work to other epochs, the synthetic spectra must be reconstructed and thus the algorithms must be retrained. In a future paper, we will explore the variations of responses matrices further.

We constructed temperature emission profiles with various numbers of underlying thermal components using an absorbed thermal emission model taken from the `XSPEC` package: `PHABS*APEC`, `PHABS*(APEC1+APEC2)`, `PHABS*(APEC1+APEC2+APEC3)`, `PHABS*(APEC1+APEC2+APEC3+APEC4)` where `PHABS` absorption represents galactic absorption. We use `APEC v3.0.9` in order to model the thermal emission. We chose not to include more than 4 thermal components since most of the literature does not include more (e.g. Fabian et al. 2006; Sanders, Fabian 2007). We created 25,000 spectra for each number of underlying thermal components; thus, we have a total of 100,000 spectra. In order to avoid any potential bias in the ordering of the spectra, we randomly selected with replacement 100,000 spectra from our sample, meaning we potentially select the same spectrum more than once; this commonly used method is known as bootstrapping. Allowing 90% of our synthetic spectra to be placed in the training set, we used the remaining 10% for the test set. This division of data is standard in machine learning applications (e.g. Breiman 2001). We run a random grid cross-validation (RGCV) search on the training set to tune the random forest hyper-parameters. At test time, the hyper-parameters are static and set to the optimal results from the RGCV search.

The algorithm outline is as follows:

(1) Construct synthetic spectra for single-, double-, triple-, and quadruple-temperature models.
(2) Create co-variance/projection matrices from PCA analysis on the training set.
(3) Train the random forest algorithm using the principal components of our synthetic data to classify spectra by their number of underlying thermal components.

(4) Project the test set into the principal component basis and verify the viability of the trained algorithm on the projected test set.

In order to verify that our algorithm works with real observations, we use *Chandra* observations of the Perseus cluster. Perseus was chosen since it is a massive, nearby cool-core galaxy cluster for which there exists a vast literature on the X-ray emission (e.g. Fabian et al. 2003; Fabian et al. 2006; Fabian et al. 2011; Sanders, Fabian 2007). Although we chose the Perseus cluster, our methodology could be readily tested on other nearby galaxy clusters such as Coma or Virgo. With a test cluster defined, we select emission parameters which coincide with the Perseus cluster. Unless otherwise noted, we adopted a column density, $n_H = 0.14 \times 10^{22} \mathrm{cm}^2$ (Kalberla et al. 2005), and a redshift equal to 0.018, chosen to coincide with the Perseus cluster (e.g. Gudehus 1991; Hudson et al. 1997; Hicken et al. 2009). In order to demonstrate the feasibility of the algorithm for any nearby galaxy cluster, we also tested lower redshift values: 0.01 and 0.005. Equivalently, the chosen column density closely corresponds to that in the direction of the Perseus cluster (Kalberla et al. 2005). The temperature values were randomly sampled between $0.1 - 4.0$ keV since the majority of nearby galaxy cluster thermal emission is within this range, the range contains both soft and hard emission lines which are critical in fitting procedures, and is well within the observing band of *Chandra* (e.g. Henriksen, Mushotzky 1985; Fabian et al. 2003; Peterson, Fabian 2006; Böhringer, Werner 2010; Mushotzky 1984; Mohr et al. 1999; Loewenstein 2003; O'Dell et al. 2000). No minimum temperature separation between componants was imposed. The ramifications of this are explored in section § 3.4.2. We also varied the metallicity between $0.2 - 1.0$ $\mathrm{Z}_{\odot}$ – a standard range adopted for ICM (e.g. Allen, Fabian 1998; Mushotzky 1998; Peterson, Fabian 2006). We choose a target signal-to-noise value equal to 150 or approximately 22,000 counts. Although this value is high, we want the algorithm to learn to recognize the most important emission lines. Moreover, This value coincides with that used in studies of the Perseus cluster (e.g. Fabian et al. 2003; Fabian et al. 2006; Sanders, Fabian 2007). In order to demonstrate the robustness of the algorithm to lower signal-to-noise values, we also tested its performance on data with a signal-to-noise value of 50 (2500 counts) in § 3.4.1.3.

3.2.4. Chandra Observations of the Perseus Cluster

The Perseus cluster has been observed for over 1.4 mega seconds with the *Chandra* X-ray Observatory. Although the majority of the observations focus on the cluster's core (which is believed to contain multi-temperature regions according to, for example, Sanders et al. 2010), we select ObsID 3209 (81.4 ks) and ObsID 4289 (90.4 ks). These two observations were selected for several reasons: they were taken at approximately the same time and each contain a significant number of counts. In both observations the front-illuminated ACIS-S2, ACIS-I1, and ACIS-I3 chips were activated. Starting with the level I event file provided

by the *Chandra* X-ray Observatory (CXC) team, we followed a standard cleaning and reduction technique using `CIAO V4.12, CALDB V4.9.0, PYTHON V3.5.1`. We first removed point-sources detected by `VTPDETECT` from a background CCD (ACIS-I1) and then applied the `LC_SIGMA_CLIP` script with a 2σ threshold to removed time intervals exhibiting background flares. We proceeded to apply time-dependent and charge-transfer gain corrections, destreak, and process the data using the `CHANDRA_REPRO` tool with `VFAINT=TRUE`. An exposure corrected, background subtracted, merged image between 0.5-7.0 keV was created using the `merge_obs` tool. Spectroscopic fits using `SHERPA V4.12.0` and `XSPEC V12.10.1` are described in §3.5.

3.3. Results on the Synthetic Spectra

Before applying our methodology to real data, we tested it against synthetic data. These results lay the foundation of our future results.

3.3.1. Principal Component Analysis

We apply the `SKLEARN` implementation of the PCA method as described in §3.2.1 to the 36000 synthetic spectra that comprise our training set. Figure 3.1 shows the mean spectra and the eigen-spectra of our training set. The eigen-spectra are the principal components projected onto the original domain (they are the $\vec{v_j}$ in equation 3.2.1). We note that the primary variations in all components are visible in the soft X-ray regime (0.5-2.0 keV). This trend is expected since we are primarily modeling the diffuse hot gas which emits mainly in this regime. The first two eigen-spectra can be interpreted physically as follows. The first eigen-spectra, component 1 in Figure 3.1, captures the difference in the ultra soft (0.5-1.0 keV) and soft diffuse emission (1.0-2.0 keV). The second eigen-spectra, component 2 in Figure 3.1, captures the Fe-L/Ne and Mg emission lines. The remaining principal components do not have a clear physical interpretation. This is often an issue in principal component analysis (e.g. Jolliffe, Cadima 2016).

In order to determine how many principal components we need to include, we study the overall variance retained versus the number of principal components. We find that, in order to capture 99% of the variance in our synthetic data, 25 principal components are required. After 25 principal components, the variance plateaus. Hence, we adopt 25 as the optimal number of principal components.

Figure 3.2 visualizes the projection of our training set (36000 spectra) onto the principal component basis (the a_{ij} values in equation 3.2.1). The principal component vectors represent the eigen-spectra which can be added linearly to reconstruct 99% of the variance in a given spectrum. We will use these components as the inputs for our random forest classifier since

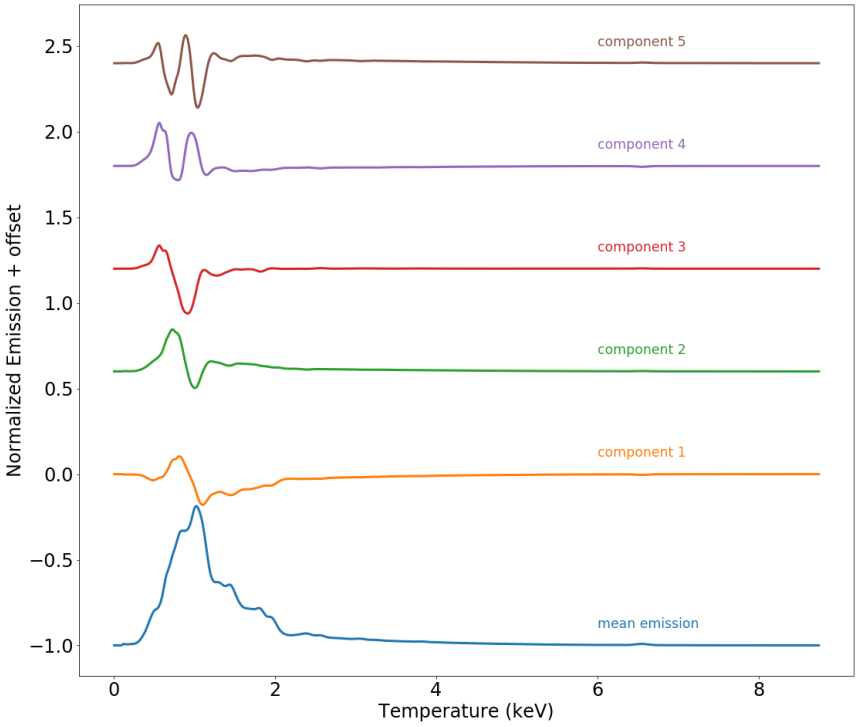

Fig. 3.1. The Principal Component Analysis (PCA) effectively reduces a higher dimensional problem into a linear combination of eigen-vectors (eigen-spectra) and a mean emission profile – see equation 3.2.1. In this graphic, we visualize the mean emission spectra, as determined by the PCA, and the first five eigen-spectra.

they capture the variance in the spectra in a lower-dimensional set compared to the unadulterated spectra. The random forest classifier will be used to determine the number of underlying temperature components in a spectra given its principal components.

Although the data does not segregate itself into different regions in each component, we can see that certain trends exists for the different temperature bins which allow for easier classification in later stages of our methodology. For example, in Figure 3.2 (a), spectra with four components follow a tight negative trend until component one is approximately 3 and then abruptly changes to a positive trend. Thus, if the first and second principal components of a spectrum do not lie on this trend, the spectra will not be classified as having four underlying thermal components.

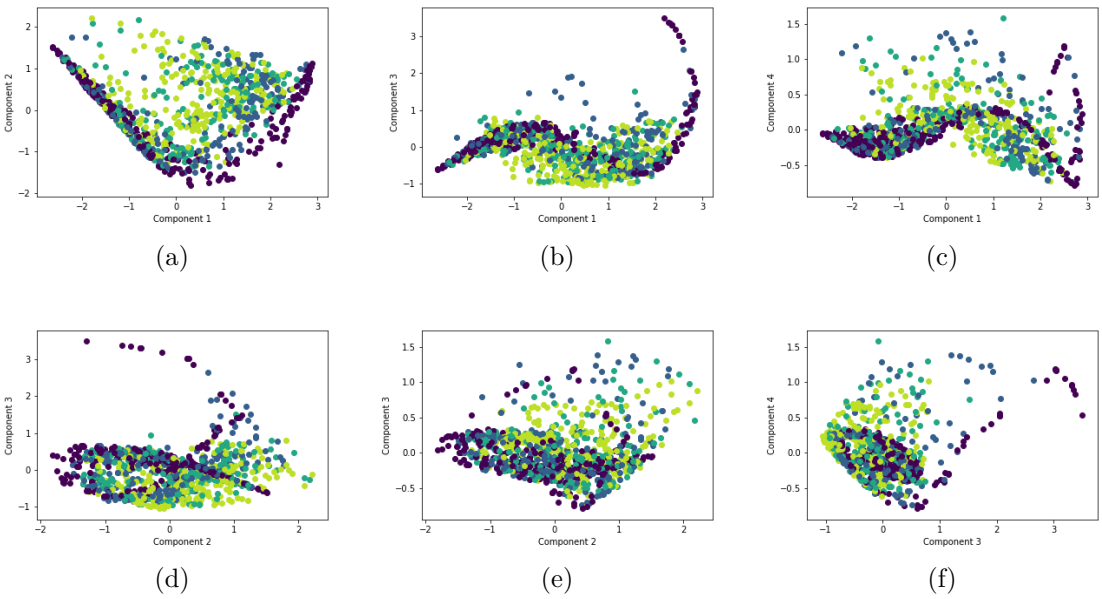

Fig. 3.2. Principal Component Analysis (PCA) Comparison Plots for 1000 randomly selected training spectra. The number of underlying thermal components are color coded in the following fashion: Single, Double, Triple, Quadruple. (a) Component 1 vs 2, (b) Component 1 vs 3, (c) Component 1 vs 4, (d) Component 2 vs 3, (e) Component 2 vs 4, (f) Component 3 vs 4.

3.3.2. Random Forest Classification

Once the projection matrix is calculated from the spectra in the training set, we apply it to obtain the 25 first principal components of every spectra in the training set, and use those to train our random forest classifier. After the training of our decision tree, we will be able to apply it to other spectra by using our pre-calculated projection matrix to reproject the new spectrum into the principal component basis and applying the pre-trained random forest classification algorithm. We define training to be successful if we can achieve higher than 50% accuracy in our test set. We use confusion matrices to validate the results; confusion matrices are frequently used in the machine learning community to visualize the accuracy of the predictions against a validation set (Kohavi, Provost 1998). An optimal algorithm will have all the values along the diagonal – this indicates that the algorithm's predictions match the ground truth values which are in our case the number of underlying spectral components.

Figure 3.3 demonstrates the efficacy of this model for estimating the number of thermal components in synthetic X-ray spectra since the matrix is mainly diagonal. A diagonal covariance matrix indicates that the method is properly categorizing the number of underlying thermal components. For example, the algorithm correctly predicts that a spectrum has

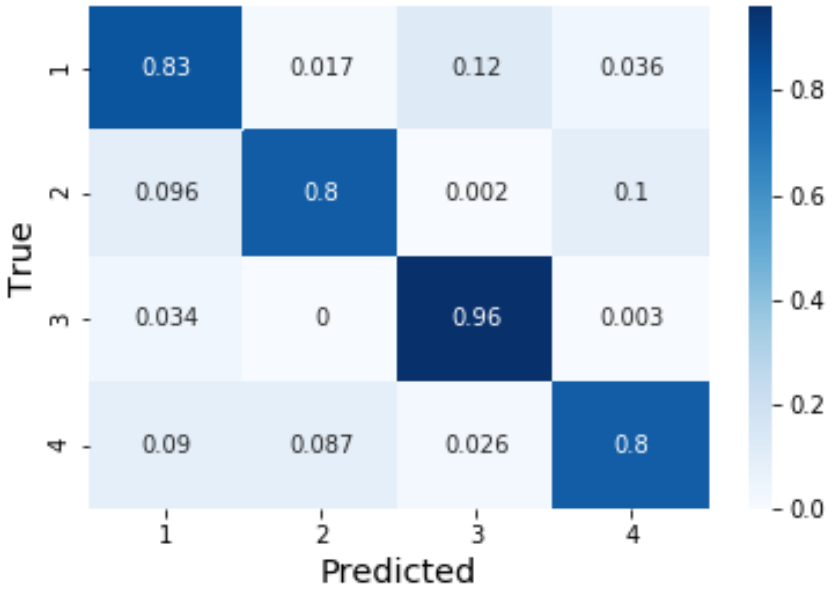

Fig. 3.3. Random forest confusion matrix evaluated on the test set consisting of 8,000 spectra. The X and Y axis represent the number of underlying thermal components predicted and actually present in the spectra. The majority of counts are bundled along the diagonal, indicating the relatively-high predictive accuracy of the method. Values are normalized by the total number of counts per row.

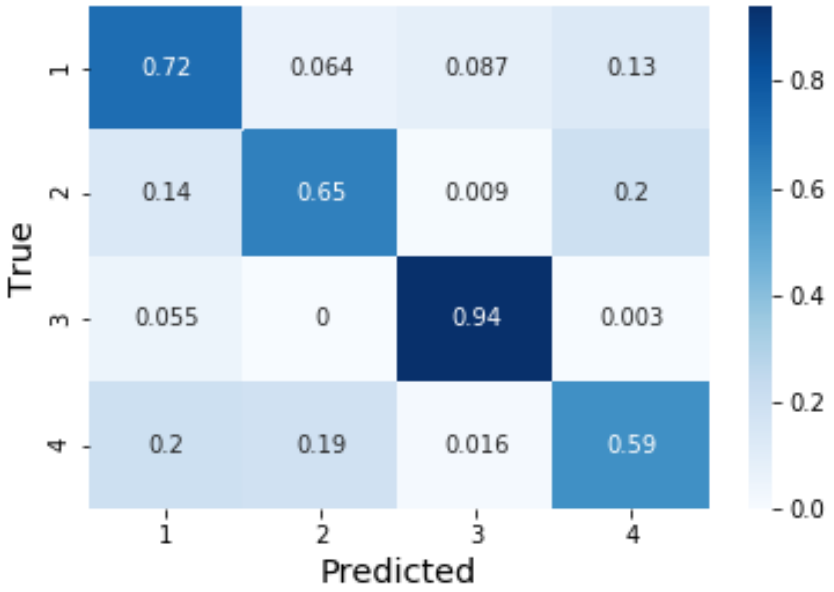

Fig. 3.4. Confusion Matrix created by omitting the principal component analysis and running the random forest directly on the spectra themselves.

three underlying components 95% of the time. The third row also indicates that the algorithm incorrectly predicts the three-component spectrum as having one component 4.6%, two components 0.1%, and four components 0.7% of the time. The graphic also notes the weak points in the algorithm: primarily distinguishing between two and four thermal components. We repeated the same machine learning algorithm neglecting the PCA step (i.e. running our random forest directly on the spectra). A comparison of Figure 3.3 (PCA) and Figure 3.4 (no PCA) reveals the power of using principal component analysis to extract the crucial spectral features.

3.4. Discussion

3.4.1. Limitations

As with the development of any new method, it is important to understand its limitations. The following section explores many ways in which we attempted to "break" our algorithm and the resulting conclusions.

3.4.1.1. *Application to More Components*

In order to determine how the methodology handles regions with more than four underlying thermal components, we created 100 synthetic spectra with five thermal components: `PHABS*(APEC1+APEC2+APEC3+APEC4+APEC5)`. We then applied our methodology to this set. As readily seen in figure 3.5, the algorithm heavily favors a four-component model.

This indicates that the algorithm is able to accurately realize that there are at least four thermal components. As such, we recommend using a classification as four-component as a lower limit for the number of underlying thermal components. While beyond the scope of this paper, it would be worthwhile to explore an algorithm extending up to higher numbers of components. We strongly suggest users do not use the random forest trained as such to classify more than four components since the extrapolation abilities of such methods are limited.

3.4.1.2. *Model Dependence: `APEC` vs. `MEKAL`*

As noted, we created our synthetic spectra using the `APEC` model. However, the observational X-ray astronomy community still debates the advantages of the `APEC` model over its predecessor, the `MEKAL` model. In order to demonstrate that our methodology is thermal-model agnostic, we asked two questions: does the algorithm work as well for synthetic spectra built from the `MEKAL` model and can the algorithm accurately classify `MEKAL` spectra if trained on an `APEC` model and vice-versa? We once again created 10,000 synthetic spectra for single, double, triple, and quadruple temperature components (totaling 40,000 spectra), but

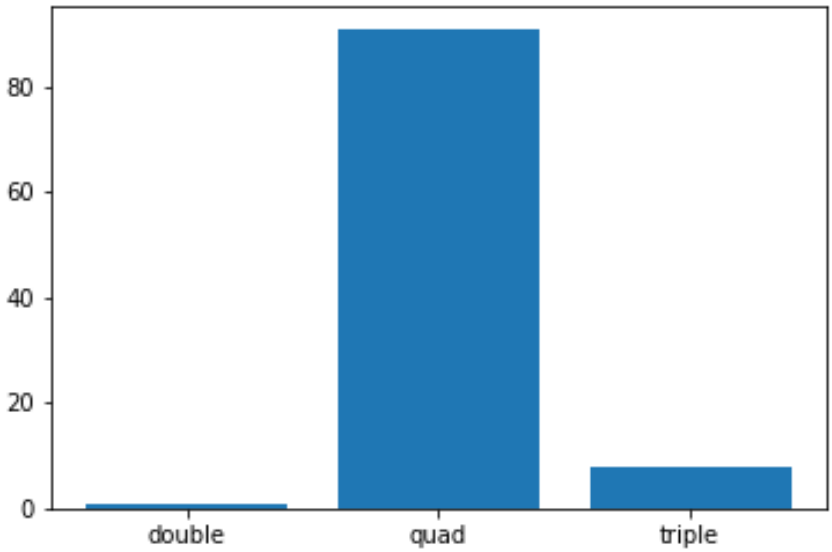

Fig. 3.5. Using our 100 spectra with five underlying thermal components, we applied our methodology. On the y-axis, we can see the number of spectra categorized by the algorithm as either double (2 components), triple (3 components), or quad (4 components).

this time using the `MEKAL` model: `PHABS*MEKAL`. We use the `MEKAL` model realization in the `CIAO` package. We then trained and tested our algorithm in an identical manner. Figure 3.6 demonstrates that the random forest performs equally as well for the `MEKAL` model as the `APEC` model. Additionally, we tested if an algorithm trained on data created using the `APEC` model could accurately categorize data created using the `MEKAL` model and vice-versa. Unfortunately, under these conditions, our algorithm does slightly better than random choice. Thus, it is important that, for real observations, the `APEC`-trained and `MEKAL`-trained models return the same predictions since it is still debated whether the `APEC` or `MEKAL` model is more appropriate.

3.4.1.3. *Signal to Noise Constraints*

Our initial set of synthetic spectra were created assuming a signal-to-noise ratio of 150. Here, we explore the dependence of our algorithm predictive powers on the signal-to-noise of the test spectra. Using our pre-trained algorithm, we predicted the number of thermal-emission components in synthetic spectra with a signal-to-noise ratio of 50. A signal-to-noise value of 50 was chosen since it is a commonly chosen value in the literature because it ensures that the spectra will have enough data to constrain the thermodynamic parameters (e.g. Diehl, Statler 2006; Schenck et al. 2014; Datta et al. 2014). We can see from figure 3.7 that the algorithm continues to perform well on lower signal-to-noise data than its initial

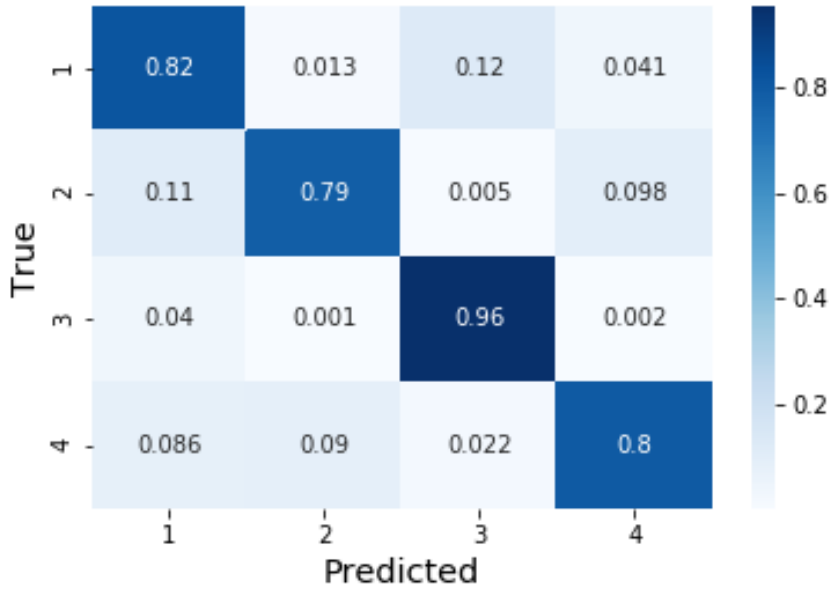

Fig. 3.6. Confusion matrix for an algorithm trained and verified on synthetic spectra generated using the `MEKAL` thermal model. We note consistent results regardless of the training set's thermal model.

training set. This is important because it allows us to use this technique on exposures that are shallower than that of the Perseus cluster.

3.4.1.4. *Relative Abundance of Thermal Components*

An often overlooked question when fitting multiple thermal components is the relative strength of the different components. Physically this could be due to either the relative density differences or amount of the plasma in that state in a given region. Relative strengths of the components were randomly varied and normalized to the sum to 1[1]. We created 15,000 synthetic spectra from each number of temperature components resulting in a total of 60,000 synthetic spectra with varying relative strengths. No changes were seen in the confusion matrix, and so we note that changes to the relative strengths of thermal components does not affect the reliability of our methodology. **Throughout the remainder of the paper, we make the assumption that each thermal component contributes equally to the overall spectrum.**

[1]As an example, if we have a spectra with two underlying components, we allow the strength of the first thermal component to be 30% and the strength of the second component to be 70%.

3.4.2. Minimal Separation between Thermal Components

As mentioned in § 3.2.3, we imposed no minimum separation of the temperature of each component in spectra with multiple underlying thermal components. In order to asses whether or not this negatively affected our classifications, we studied the spectra that were mis-classified by the random forest. If the lack of a minimum separation was responsible for the mis-classifications, we would expect the mean separation in temperatures of the different components in the mis-classified spectra to be small. When calculated, we find the mean temperature separation between components to be approximately 1.3 keV (with a variance of approximately 0.3 keV) which is consistent given the uniform distribution over the chosen range of temperatures (0.1 - 4.0 keV) used to construct the spectra. We conclude that mis-classifications are not due to components having near-identical temperatures in the training set; therefore, the accuracy of the method would not benefit from imposing a minimum separation between thermal components. The well-classified data has approximately the same mean separation and mean variance in the separation. Morever, the goal of this work is not to distinguish between minimally separated thermal components, but rather to determine the number of primary thermal components necessary to describe the emission.

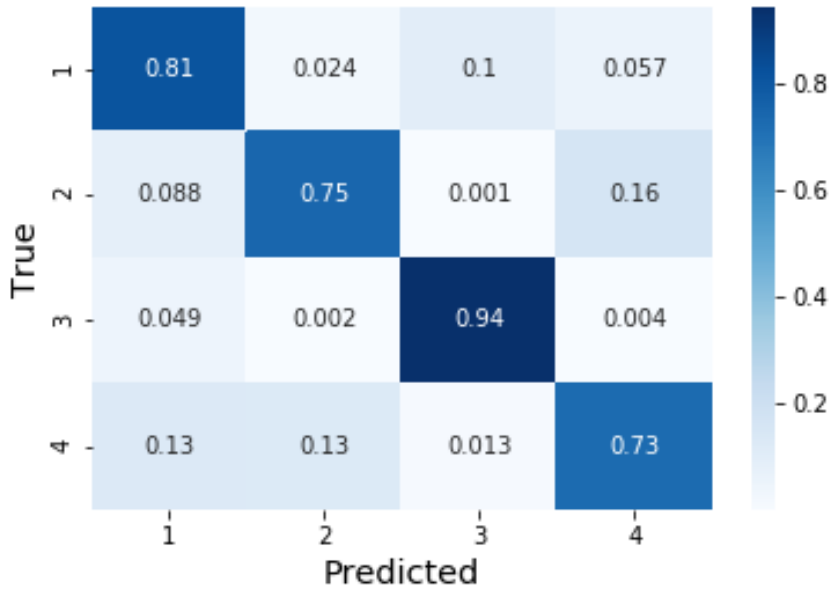

Fig. 3.7. We used the algorithm trained on a signal-to-noise ratio of 150 and applied it to spectra with a signal-to-noise ratio of 50. Though the random forest loses some of its predictive power, it still estimates the correct number of parameters the majority of the time in all cases. This is likely due to the effects of the increased noise.

3.4.3. Necessity and Meaning of Multiple Components

As outlined in §4.1, it is critical that the appropriate number of underlying thermal components is chosen so that the physics of the system can be understood. Although the X-ray spectra is undoubtedly a results of a continuum of thermal emission components, there exist peaks in this distribution (e.g. Kaastra et al. 2004). When we apply procedures to search for multi-phase gas, we are indeed searching for the temperature peaks in the distribution. In addition for the need to categorize the gas correctly in order to accurately describe the plasma's physics, underestimating the number of underlying thermal components has implications for the efficacy of fits. In order to quantify these implications, we consider a plasma with two underlying components. We generate a mock *Chandra* spectrum assuming a SNR of 150 which is comprised of two `APEC` models at redshift z=0 with $Z_{met} = 0.3\mathrm{M}_{\odot}$ with temperatures set to 4 keV and 8 keV. We bin the data at 50 counts per bin. We attempt to fit a single `APEC` model to the mock spectra. The model finds a best-fit temperature of 5.3 keV. However, the fit statistic ($\chi^2 = 2.3$) and q-value ($q \sim 10^{-42}$) indicate that the fit is unacceptable. Thus we are confident that a single thermal component does not adequately describe a spectrum with two underlying thermal components.

3.5. Perseus Cluster Observations

In Fig. 3.8, we show the Chandra X-ray observations of the Perseus cluster used to test our machine learning approach. Our goal is to apply our techniques outlined in Section 4.2 and determine the number of thermal emission components in a given region of the Perseus cluster. To do this, we first applied the weighted voronoi tessellation (WVT) algorithm to the reduced X-ray data described in section §3.2.4. The bin map resulting from the WVT algorithm is routinely used to study the structure of ICM X-ray emission (e.g. Cappellari, Copin 2003; Diehl, Statler 2006). The WVT algorithm works by binning the merged image into self-similar signal-to-noise regions initially using a simple bin accretion algorithm. These regions are used as an initial guess for the true WVT algorithm which minimizes a scale length, defined *a-priori*, so that the pixels are grouped into final, optimized bins. Thus, the final product is an image of binned pixels which indicate the underlying signal-to-noise structure[2]. Setting the target signal-to-noise ratio of 150 (22,000 counts) results in 916 binned regions for the cluster core (see magenta box in Fig. 3.8). Having completed the binning map, we proceeded to create a corresponding spectrum for each region using the `CIAO` tool `SPECEXTRACT` for each ObsID; additionally, we use a background region created from a blanksky file created with the `BLANKSKY` script.

[2]Our implementation of this technique can be found at https://github.com/crhea93/AstronomyTools under the Weighted Voronoi Tessellation directory which contains further documentation and testing.

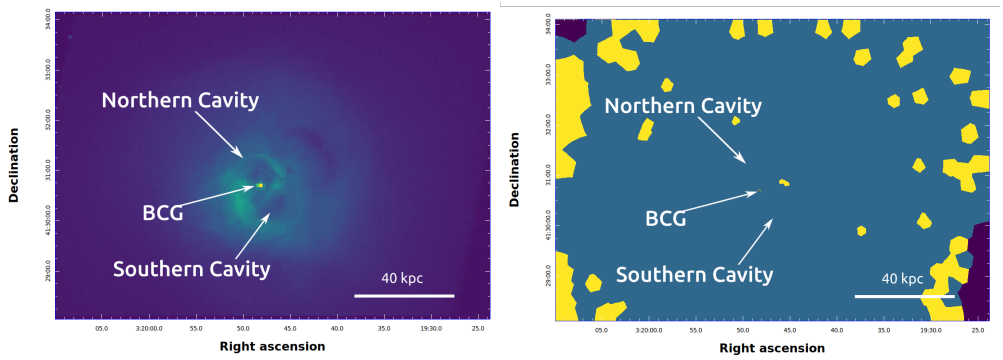

Fig. 3.8. Left: Background-subtracted, exposure-corrected, and smoothed image of the core of the Perseus cluster. The emission shown is between 0.1-8 keV. Right: A weighted voronoi tessellation map of the Perseus cluster using a signal-to-noise value of 150. We have a total of 1271 bins. The bins are color-coded in order to reveal the number of underlying temperature-components hidden in the spectra as classified by our random forest algorithm in the following manner: Single, Double, Triple, Quadruple. The image clearly demonstrates the necessity of multiple components when modeling the hot plasma's X-ray emission captured by *Chandra*.

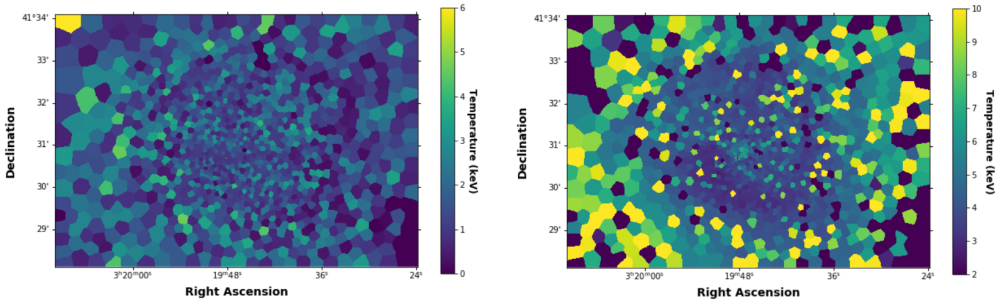

Fig. 3.9. Temperature Maps of the Perseus cluster in regions designated as containing two or more underlying thermal components. The first component is shown on the left, while the second component is shown on the right. The figure demonstrates that the two temperature components are well separated. We only show regions for which the fits recovered acceptable reduced chi statistics ($0.8 < \chi^2 < 1.2$).

Using the spectral files for each region, we applied our methodology as follows. We first employed our principal component analysis decomposition on each combined spectrum in order to project the spectrum to the PCA-space. We then used our trained[3] random forest classifier to predict the number of underlying thermal components in each region's spectrum. This was done for both ObsIDs: 3209 and 4289. We then selected the final classification as the output with the highest aggregate probablity after combining the results of the two independent classifiers (see § 3.2.2). The results can be seen in Figure 3.8. As suspected, the ICM in the Perseus cluster cannot be classified as a single-temperature plasma, but

[3]We trained the algorithm twice: once with the `APEC` model and once with the `MEKAL` model. We report that both algorithms result in the same underlying temperature map.

rather, our methodology has revealed that several thermal components are necessary to properly model it; this is congruent with studies using traditional methods (Fabian et al. 2006; Sanders, Fabian 2007; Fabian et al. 2011). Moreover, the algorithm reveals that the majority of the ICM has two underlying components. A map showing the confidence with which each region is assigned a number of underlying thermal components is shown in appendix C.

Additionally we calculate temperature maps for the regions containing two underlying thermal components. Temperature maps were calculated following standard fitting procedures outlined by the *Chandra* X-ray Observatory (e.g. Fabian et al. 2006; Sanders et al. 2004). We use `Sherpa v4.12.1` to simultaneously fit the spectra of regions defined by our weighted voronoi tessellation map for each observation with an absorbed thermal model (`PHABS*APEC`). Similar to the procedure in § 3.2.3, we adopted a redshift of 0.0179 and column density,n_H, equal to $0.14{\times}10^{22}\mathrm{cm}^2$. We model the background X-ray emission with a soft X-ray Galactic component (APEC) with a temperature of 0.18keV and metallicity Z=1 and a hard cosmic X-ray component (BREMSS) with a temperature of $kT = 40$keV. The data were binned at 50 counts. The temperature maps for each component are shown in figure 3.9. Similar to the results show in figure 12 of Sanders et al. (2004), we find that the two principal thermal components in the central regions of the cluster are characterized by a cooler ($\approx$ 2keV) and hotter ($\approx$ 4keV) gas.

While we do not explore in detail the thermodynamic properties of the Perseus cluster in this paper, we have demonstrated not only the applicability, but also the virtue and potency, of our methodology when adapted to real observations. We also note that we do not compare the number of underlying thermal components determined by our algorithm to the number expected using the standard method since the standard method contains inherent issues.

3.6. Implications for the X-ray Community

We emphasize that despite the fact that this article focuses on data obtained by the *Chandra* X-ray Observatory, this technique can be applied to other X-ray missions such as *XMM-Newton*, *Athena* or *XRISM*. Moreover, this technique will allow for the fast and unbiased – in the sense that it requires no human intervention – categorization of galaxy cluster spectra which will be important in upcoming X-ray survey missions such as eROSITA (e.g. Merloni et al. 2012). With the advent of X-ray telescopes that have a higher spectral resolution, such as the Athena Space X-ray Observatory (e.g. Barret et al. 2020), we can expect this classification methodology to perform even more accurately since there will be more emission features to use in the classification. However, a change in either the spectral resolution or instrument will require retraining the algorithm. Doing so will ensure that the algorithm is learning the proper response matrices and guiding spectral lines/ratios.

We also note that, with the proper training set, this methodology can be applied to other astrophysical phenomenon that emit in the X-rays such as AGN and supernovae remnants.

Although the algorithm performs well on test data and real observations, an additional complication arises when applying the algorithm to a different time epoch (i.e. a *Chandra* cycle other than cycle 03). As discussed, the CCD cameras have been degrading over time, thus the response matrices change from cycle to cycle. In a future paper, we will explore different techniques to design the machine learning methodology presented here cycle-agnostic. In a separate follow-up paper, we will also explore the applicability of machine learning methods to the prediction of spectral emission parameters such as temperature and metallicity using *Chandra* X-ray spectra.

3.7. Conclusions

This paper has explored the efficacy of principal component analysis coupled with a random forest classifier for classifying the number of underlying thermal-emission components in the X-ray spectra of hot gas in galaxy clusters. The python code package, Pumpkin, created for this analysis is readily available at the following github address: `https://github.com/XtraAstronomy/Pumpkin`.

We have included several examples in the form of jupyter notebooks in order to facilitate the reproducability of our results and to make our code more accessible to the community. To address potential issues regarding our training set (i.e. choice of redshift, column density, and temperature range), we have included a tutorial on creating synthetic spectra and training the random forest algorithm so that our methodology can be easily applied to galaxy clusters and groups at different epochs. We have also included a tutorial on applying the pre-trained PCA and random forest algorithms directly to observations.

Our primary conclusions are as follows:

- We report the success of our methodology in estimating the number of thermal components on both synthetic and real X-ray observations of galaxy clusters. A comparison with the literature revealed concurrent results in the case of the Perseus cluster.
- We explored the effects of different temperature models, `MEKAL` and `APEC`, on the algorithm. There are no discernible effects dependant on the chosen model. However, the algorithm does not reliably predict the number of underlying thermal components if trained on one temperature model then tested on the other.
- We note that a slight decrease in signal-to-noise (150 to 50) does not drastically affect the accuracy of the predictiosns
- The redshift and column density were uniformly sampled from a realistic range in order to demonstrate that the algorithm is not negatively affected by natural heterogeneity in the parameter space.

- We confirm that the core of the Perseus cluster is best categorized by several thermal emission components rather than by a single component.
- We developed several tutorials for the use and adaptability of our algorithm.

The following paper in this series will focus on the feasibility of using machine learning to better understand the temperature parameter of X-ray spectra.

C. R. acknowledges financial support from the physics department of the Université de Montréal. J. H.-L. acknowledges support from NSERC via the Discovery grant program, as well as the Canada Research Chair program. We would like to thank Farbod Jarandar for the enlightening discussions on machine learning techniques for spectral analysis.

The progamming aspects of this paper were completed thanks to the following packages of the python programming language (Van Rossum, Drake 2009): `numpy` (Walt van der et al. 2011, `scipy` (Virtanen et al. 2020), `matplotlib` (Hunter 2007), `pandas` (McKinney 2010), `seaborn` (Waskom et al. 2017), `astropy` (Collaboration et al. 2018; Robitaille et al. 2013), `sherpa` (Freeman et al. 2001).

Appendix

3.7.1. Principal Component Analysis

We outline the standard PCA procedure following the seminal work by Murtagh, Heck (1987). Mathematically, PCA is an orthogonal transformation which transforms the data from a basis of variables in which the data is correlated, to a basis in which the data is linearly uncorrelated. Any new data can then be projected onto this new basis. Consider a set of N spectra covering the same energy range where each spectrum is represented as an M-dimensional vector, X; together, these N vectors span an M-dimensional space, Sthus, they generate a M-dimensional vector space, S. The first principal component, X_0, is defined to be in the direction of maximum variance in S. Subsequently, the i^{th} component is in the direction of the i^{th} highest variance in the perpendicular subspace spanned by the first $i-1$ principal components. There are a total of M principal components. Defining r_{ij} as the initial spectra measurements, where i represents the spectrum's number and j represents the wavelength bin, we can develop the necessary equations:

$$X_{ij} = r_{ij} - \bar{r}_i \tag{3.7.1}$$

$$\bar{r}_i = \frac{1}{N}\sum_{i=1}^{N} r_{ij} \tag{3.7.2}$$

A covariance matrix, C, is constructed in the following fashion,

$$C_{jk} = \frac{1}{N}\sum_{i=1}^{N} X_{ij}X_{jk} \tag{3.7.3}$$

where $1 \leq j,k \leq M$. The first principal component is defined by the following form:

$$\mathbf{Ce_1} = \lambda_1 \mathbf{e_1} \tag{3.7.4}$$

in which $\mathbf{e_1}$ and λ_1 represent the first (thus numerically largest) eigenvector-eigenvalue pair. In the context of ICM spectra, these components represent the parameters corresponding to the primary emission variables (temperature, column density, redshift, etc.) or some combination of them. In this work, eigenspectra are calculated using the `SKLEARN.DECOMPOSITION.PCA` package which uses SVD to decompose the spectra into its principal components.

3.7.2. Weighted Voronoi Tessellation Map of Perseus

This section includes the weighted voronoi tessellation map of the Perseus cluster and a brief discussion on the signal-to-noise statistics. We see that the WVT bins follow no particular structure as expected. Furthermore, the signal-to-noise of the bins follows a Gaussian distribution with a mean about the target signal-to-noise ratio.

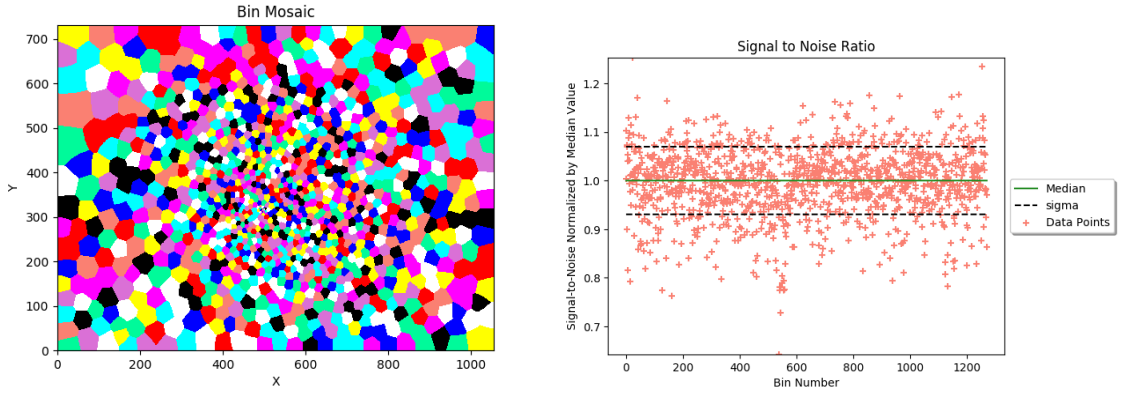

(a) (b)

Fig. 3.10. Left: Final bin mosaic of the Perseus cluster. The figure has 1271 separate bins. Each bin is randomly colored from a selection of 10 colors. The X and Y axes are in physical coordinates. Right: Normalized signal-to-noise plot for each bin in the WVT mosaic. We see that the signal-to-noise is tightly constrained around the target signal-to-noise value (150).

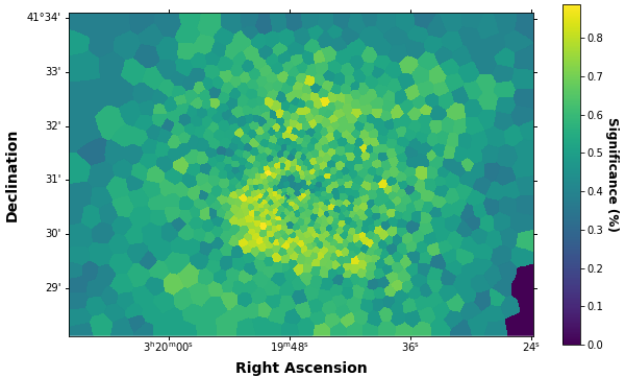

Fig. 3.11. Component significance map of the Perseus Cluster. The value assigned to each pixel represents the probability with which each region was assigned a given number of underlying thermal components. The mean significance is approximately %70.

3.7.3. Component Significance Map

In this section, we provide the component significance map which shows the relative probabilities of containing x-number thermal components determined by the random forest classifier. We note that the strongest regions of confidence follow the thermal contour shown in figure 3.9. The existence of this thermal contour has been explored thoroughly in several other papers (e.g. Sanders et al. 2004; Sanders et al. 2010; Fabian et al. 2011).

References

Allen S. W., Fabian A. C. The relationship between cooling flows and metallicity measurements for X-ray-luminous clusters // Monthly Notices of the Royal Astronomical Society. VII 1998. 297, 3. L63–L68.

Allen S. W., Rapetti D. A., Schmidt R. W., Ebeling H., Morris G., Fabian A. C. Improved constraints on dark energy from Chandra X-ray observations of the largest relaxed galaxy clusters // Monthly Notices of the Royal Astronomical Society. XII 2007. 383, 3. 879–896. arXiv: 0706.0033.

Allen S. W., Schmidt R. W., Fabian A. C., Ebeling H. Cosmological constraints from the local X-ray luminosity function of the most X-ray luminous galaxy clusters // Monthly Notices of the Royal Astronomical Society. VI 2003. 342, 1. 287–298. arXiv: astro-ph/0208394.

Barret Didier, Decourchelle Anne, Fabian Andy, Guainazzi Matteo, Nandra Kirpal, Smith Randall, Herder Jan-Willem den. The Athena space X-ray Observatory and the astrophysics of hot plasma // Astronomische Nachrichten. II 2020. 341, 2. 224–235. arXiv: 1912.04615.

Barros Rodrigo Coelho, Basgalupp Márcio Porto, Carvalho André C. P. L. F. de, Freitas Alex A. A Survey of Evolutionary Algorithms for Decision-Tree Induction // IEEE Transactions on Systems, Man, and Cybernetics, Part C (Applications and Reviews). V 2012. 42, 3. 291–312.

Beitia-Antero L., Yáñez J., Castro A. I. Gómez de. On the Use of Logistic Regression for stellar classification. An application to colour-colour diagrams // Experimental Astronomy. VIII 2018. 45, 3. 379–395. arXiv: 1805.09551.

Biau Gerard. Analysis of a Random Forests Model // Journal of Machine Learning Research. 2012. 13. 1063–1095.

Bocquet S., Saro A., Mohr J. J., Aird K. A., Ashby M. L. N., Bautz M., Bayliss M., Bazin G., Benson B. A., Bleem L. E., Brodwin M., Carlstrom J. E., Chang C. L., Chiu I., Cho H. M., Clocchiatti A., Crawford T. M., Crites A. T., Desai S., Haan T. de, Dietrich J. P., Dobbs M. A., Foley R. J., Forman W. R., Gangkofner D., George E. M., Gladders M. D., Gonzalez A. H., Halverson N. W., Hennig C., Hlavacek-Larrondo J., Holder G. P., Holzapfel W. L., Hrubes J. D., Jones C., Keisler R., Knox L., Lee A. T., Leitch E. M., Liu J., Lueker M., Luong-Van D., Marrone D. P., McDonald M., McMahon J. J., Meyer S. S., Mocanu L., Murray S. S., Padin S., Pryke C., Reichardt C. L., Rest A., Ruel J., Ruhl J. E., Saliwanchik B. R., Sayre J. T., Schaffer K. K., Shirokoff E., Spieler H. G., Stalder B., Stanford S. A., Staniszewski Z., Stark A. A., Story K., Stubbs C. W., Vanderlinde K., Vieira J. D., Vikhlinin A., Williamson R., Zahn O., Zenteno A. Mass Calibration and Cosmological Analysis of the SPT-SZ Galaxy Cluster Sample Using Velocity Dispersion

σ_v and X-ray $Y_\textrm{X}$ Measurements // The Astrophysical Journal. I 2015. 799, 2. 214. arXiv: 1407.2942.

Boute D. A. Iron Gradients in Cooling Flow Galaxies and Groups // Astrophysical Journal. 2000. 539. 172–186.

Bradt H., Mayer W., Naranan S., Rappaport S., Spada G. Evidence for X-Radiation from the Radio Galaxy M87 // The Astrophysical Journal. XII 1967. 150. L199.

Bradt H., Rothschild R.E., Swank J.H. X-ray timing explorer mission // Astronomy and Astrophysics Supplement Series. 1993. 97. 355–360.

Breiman L. Random Forests // Machine Learning. 2001. 45. 5–32.

Breiman L., Friedman J.H., Olshen R.A., Stone C.J. Classification and Regression Trees. 1984.

Breiman Leo. Bagging predictors // Machine Learning. VIII 1996. 24, 2. 123–140.

Brickhouse N.S., Smith R.K., Raymond J.C., Liedahl D.A. 2000.

Bro Rasmus, Smilde Age K. Principal component analysis // Anal. Methods. 2014. 6, 9. 2812–2831.

Böhringer Hans, Werner Norbert. X-ray spectroscopy of galaxy clusters: studying astrophysical processes in the largest celestial laboratories // The Astronomy and Astrophysics Review. II 2010. 18, 1-2. 127–196.

Cappellari M., Copin Y. Adaptive spatial binning of integral-field spectroscopic data using Voronoi tessellations // Monthly Notices of the Royal Astronomical Society. VI 2003. 342, 2. 345–354.

AN ENTROPY THRESHOLD FOR STRONG Ha AND RADIO EMISSION IN THE CORES OF GALAXY CLUSTERS. // . 2008. 683. 4.

Churazov E., Forman W., Jones C., Bohringer H. XMM-Newton Observations of the Perseus Cluster. I. The Temperature and Surface Brightness Structure // The Astrophysical Journal. VI 2003. 590, 1. 225–237.

Collaboration The Astropy, Price-Whelan A. M., Sipőcz B. M., Günther H. M., Lim P. L., Crawford S. M., Conseil S., Shupe D. L., Craig M. W., Dencheva N., Ginsburg A., VanderPlas J. T., Bradley L. D., Pérez-Suárez D., Val-Borro M. de, Aldcroft T. L., Cruz K. L., Robitaille T. P., Tollerud E. J., Ardelean C., Babej T., Bachetti M., Bakanov A. V., Bamford S. P., Barentsen G., Barmby P., Baumbach A., Berry K. L., Biscani F., Boquien M., Bostroem K. A., Bouma L. G., Brammer G. B., Bray E. M., Breytenbach H., Buddelmeijer H., Burke D. J., Calderone G., Rodríguez J. L. Cano, Cara M., Cardoso J. V. M., Cheedella S., Copin Y., Crichton D., DÁvella D., Deil C., Depagne É, Dietrich J. P., Donath A., Droettboom M., Earl N., Erben T., Fabbro S., Ferreira L. A., Finethy T., Fox R. T., Garrison L. H., Gibbons S. L. J., Goldstein D. A., Gommers R., Greco J. P., Greenfield P., Groener A. M., Grollier F., Hagen A., Hirst P., Homeier D., Horton A. J., Hosseinzadeh G., Hu L., Hunkeler J. S., Ivezić Ž, Jain A., Jenness T., Kanarek

G., Kendrew S., Kern N. S., Kerzendorf W. E., Khvalko A., King J., Kirkby D., Kulkarni A. M., Kumar A., Lee A., Lenz D., Littlefair S. P., Ma Z., Macleod D. M., Mastropietro M., McCully C., Montagnac S., Morris B. M., Mueller M., Mumford S. J., Muna D., Murphy N. A., Nelson S., Nguyen G. H., Ninan J. P., Nöthe M., Ogaz S., Oh S., Parejko J. K., Parley N., Pascual S., Patil R., Patil A. A., Plunkett A. L., Prochaska J. X., Rastogi T., Janga V. Reddy, Sabater J., Sakurikar P., Seifert M., Sherbert L. E., Sherwood-Taylor H., Shih A. Y., Sick J., Silbiger M. T., Singanamalla S., Singer L. P., Sladen P. H., Sooley K. A., Sornarajah S., Streicher O., Teuben P., Thomas S. W., Tremblay G. R., Turner J. E. H., Terrón V., Kerkwijk M. H. van, Vega A. de la, Watkins L. L., Weaver B. A., Whitmore J. B., Woillez J., Zabalza V. The Astropy Project: Building an inclusive, open-science project and status of the v2.0 core package // The Astronomical Journal. VIII 2018. 156, 3. 123. arXiv: 1801.02634.

Datta Abhirup, Schenck David E., Burns Jack O., Skillman Samuel W., Hallman Eric J. How Much Can We Learn From A Merging Cold Front Cluster? : Insights From X-ray Temperature and Radio Maps of Abell 3667 // The Astrophysical Journal. IX 2014. 793, 2. 80. arXiv: 1408.5123.

David L. P., Arnaud K. A., Forman W., Jones C. Einstein observations of the Hydra A cluster and the efficiency of galaxy formation in groups and clusters // The Astrophysical Journal. VI 1990. 356. 32.

Denil Misha, Matheson David, Freitas Nando de. Narrowing the Gap: Random Forests In Theory and In Practice // JMLR. 32. Beijing China: A&CP, 2014.

Diehl S., Statler T. S. Adaptive binning of X-ray data with weighted Voronoi tessellations // Monthly Notices of the Royal Astronomical Society. V 2006. 368, 2. 497–510.

Ettori S., Fabian A. C. Coulomb interactions in the intracluster medium // Monthly Notices of the Royal Astronomical Society. I 1998. 293, 1. L33–L36. arXiv: astro-ph/9710236.

Fabian A. C., Sanders J. S., Allen S. W., Canning R. E. A., Churazov E., Crawford C. S., Forman W., GaBany J., Hlavacek-Larrondo J., Johnstone R. M., Russell H. R., Reynolds C. S., Salomé P., Taylor G. B., Young A. J. A wide Chandra view of the core of the Perseus cluster: A wider view of the Perseus cluster // Monthly Notices of the Royal Astronomical Society. XII 2011. 418, 4. 2154–2164.

Fabian A. C., Sanders J. S., Allen S. W., Crawford C. S., Iwasawa K., Johnstone R. M., Schmidt R. W., Taylor G. B. A deep Chandra observation of the Perseus cluster: shocks and ripples // Monthly Notices of the Royal Astronomical Society. IX 2003. 344, 3. L43–L47. arXiv: astro-ph/0306036.

Fabian A. C., Sanders J. S., Taylor G. B., Allen S. W., Crawford C. S., Johnstone R. M., Iwasawa K. A very deep Chandra observation of the Perseus cluster: shocks, ripples and conduction // Monthly Notices of the Royal Astronomical Society. II 2006. 366, 2. 417–428.

Fawagreh Khaled, Gaber Mohamed Medhat, Elyan Eyad. Random forests: from early developments to recent advancements // Systems Science & Control Engineering. XII 2014. 2, 1. 602–609.

Forman W., Jones C., Markevitch M., Vikhlinin A., Churazov E. Chandra Observations of the Components of Clusters, Groups, and Galaxies and their Interactions // arXiv:astro-ph/0111526. 2002a. 51–62. arXiv: astro-ph/0111526.

Forman W., Jones C., Markevitch M., Vikhlinin A., Churazov E. Galaxy Clusters with Chandra // arXiv:astro-ph/0207165. VII 2002b. arXiv: astro-ph/0207165.

Forman W., Jones C., Murray S., Giacconi R. The detection of large X-ray halos in clusters // The Astrophysical Journal. X 1978. 225. L1.

Frank K. A., Peterson J. R., Andersson K., Fabian A. C., Sanders J. S. CHARACTERIZATION OF INTRACLUSTER MEDIUM TEMPERATURE DISTRIBUTIONS OF 62 GALAXY CLUSTERS WITH XMM-NEWTON // The Astrophysical Journal. I 2013. 764, 1. 46.

Sherpa: a mission-independent data analysis application. // . XI 2001. 4477. 76–87. Conference Name: Astronomical Data Analysis Place: eprint: arXiv:astro-ph/0108426.

Giacconi R., Branduardi G., Briel U., Epstein A., Fabricant D., Feigelson E., Forman W., Gorenstein P., Grindlay J., Gursky H., Harnden F. R., Henry J. P., Jones C., Kellogg E., Koch D., Murray S., Schreier E., Seward F., Tananbaum H., Topka K., Van Speybroeck L., Holt S. S., Becker R. H., Boldt E. A., Serlemitsos P. J., Clark G., Canizares C., Markert T., Novick. R. , Helfand D., Long K. The Einstein /HEAO 2/ X-ray Observatory // The Astrophysical Journal. VI 1979. 230. 540.

Gudehus Donald H. Systematic bias in cluster galaxy data, affecting galaxy distances and evolutionary history // The Astrophysical Journal. XI 1991. 382. 1.

Gursky H., Kellogg E., Murray S., Leong C., Tananbaum H., Giacconi R. A Strong X-Ray Source in the Coma Cluster Observed by UHURU // The Astrophysical Journal. VIII 1971. 167. L81.

Gursky Herbert. The X-Ray Emission from Rich Clusters of Galaxies // Publications of the Astronomical Society of the Pacific. X 1973. 85. 493.

Henriksen M. J., Mushotzky R. F. The physical implications of an isothermal model for the hot intracluster medium // The Astrophysical Journal. V 1985. 292. 441.

Hicken Malcolm, Wood-Vasey W. Michael, Blondin Stephane, Challis Peter, Jha Saurabh, Kelly Patrick L., Rest Armin, Kirshner Robert P. IMPROVED DARK ENERGY CONSTRAINTS FROM 100 NEW CfA SUPERNOVA TYPE Ia LIGHT CURVES // The Astrophysical Journal. VIII 2009. 700, 2. 1097–1140.

Horner Donald J., Mushotzky Richard F., Scharf Caleb A. Observational Tests of the Mass-Temperature Relation for Galaxy Clusters // The Astrophysical Journal. VII 1999. 520, 1. 78–86. arXiv: astro-ph/9902151.

Hudson M. J., Lucey J. R., Smith R. J., Steel J. Galaxy clusters in the Perseus-Pisces region – II. The peculiar velocity field // Monthly Notices of the Royal Astronomical Society. XI 1997. 291, 3. 488–504.

Hunter John D. Matplotlib: A 2D Graphics Environment // Computing in Science Engineering. V 2007. 9, 3. 90–95. Conference Name: Computing in Science Engineering.

Jolliffe Ian T., Cadima Jorge. Principal component analysis: a review and recent developments // Philosophical Transactions of the Royal Society A: Mathematical, Physical and Engineering Sciences. IV 2016. 374, 2065. 20150202.

Kaastra J. S., Tamura T., Peterson J. R., Bleeker J. A. M., Ferrigno C., Kahn S. M., Paerels F. B. S., Piffaretti R., Branduardi-Raymont G., Böhringer H. Spatially resolved X-ray spectroscopy of cooling clusters of galaxies // Astronomy & Astrophysics. I 2004. 413, 2. 415–439.

Kaastra J.S., Mewe R. X-ray emission from thin plasmas. I - Multiple Auger ionisation and fluorescence processes for Be to Zn // Astronomy and Astrophysics Supplement Series. 1993. 97, 2. 443–482.

Kalberla P. M. W., Burton W. B., Hartmann Dap, Arnal E. M., Bajaja E., Morras R., Poppel W. G. L. The Leiden/Argentine/Bonn (LAB) Survey of Galactic HI: Final data release of the combined LDS and IAR surveys with improved stray-radiation corrections // Astronomy & Astrophysics. IX 2005. 440, 2. 775–782. arXiv: astro-ph/0504140.

Kohavi R., Provost F. On Applied Research in Machine Learning // Editorial for the Special Issue on Applications of Machine Learning and the Knowledge Discovery Process. 1998. 30.

Lever Jake, Krzywinski Martin, Altman Naomi. Principal component analysis // Nature Methods. VII 2017. 14, 7. 641–642.

Loewenstein Michael. Chemical Composition of the Intracluster Medium // arXiv:astro-ph/0310557. X 2003. arXiv: astro-ph/0310557.

Lovisari Lorenzo, Reiprich Thomas. The Non-Uniformity of Galaxy Cluster Metallicity Profiles // Monthly Notices of the Royal Astronomical Society. II 2019. 483, 1. 540–557. arXiv: 1811.05987.

Markevitch M., Ponman T. J., Nulsen P. E. J., Bautz M. W., Burke D. J., David L. P., Davis D., Donnelly R. H., Forman W. R., Jones C., Kaastra J., Kellogg E., Kim D.-W., Kolodziejczak J., Mazzotta P., Pagliaro A., Patel S., VanSpeybroeck L., Vikhlinin A., Vrtilek J., Wise M., Zhao P. Chandra Observation of Abell 2142: Survival of Dense Subcluster Cores in a Merger // The Astrophysical Journal. X 2000. 541, 2. 542–549. arXiv: astro-ph/0001269.

Markevitch M., Sarazin C. L., Vikhlinin A. Physics of the Merging Clusters Cygnus A, A3667, and A2065 // The Astrophysical Journal. VIII 1999. 521, 2. 526–530. arXiv: astro-ph/9812005.

Markevitch Maxim, Forman William R., Sarazin Craig L., Vikhlinin Alexey. The Temperature Structure of 30 Nearby Clusters Observed with *ASCA* : Similarity of Temperature Profiles // The Astrophysical Journal. VIII 1998. 503, 1. 77–96.

Markevitch Maxim, Vikhlinin Alexey. Comparison of ASCA and ROSAT Cluster Temperatures: A2256, A3558 and AWM7 // The Astrophysical Journal. I 1997. 474, 1. 84–90. arXiv: astro-ph/9605026.

Mazzotta P., Markevitch M., Vikhlinin A., Forman W. R. Chandra Observations of Cold Fronts in Cluster of Galaxies // arXiv:astro-ph/0109420. IX 2001. arXiv: astro-ph/0109420.

McDonald M., Benson B. A., Vikhlinin A., Aird K. A., Allen S. W., Bautz M., Bayliss M., Bleem L. E., Bocquet S., Brodwin M., Carlstrom J. E., Chang C. L., Cho H. M., Clocchiatti A., Crawford T. M., Crites A. T., Haan T. de, Dobbs M. A., Foley R. J., Forman W. R., George E. M., Gladders M. D., Gonzalez A. H., Halverson N. W., Hlavacek-Larrondo J., Holder G. P., Holzapfel W. L., Hrubes J. D., Jones C., Keisler R., Knox L., Lee A. T., Leitch E. M., Liu J., Lueker M., Luong-Van D., Mantz A., Marrone D. P., McMahon J. J., Meyer S. S., Miller E. D., Mocanu L., Mohr J. J., Murray S. S., Padin S., Pryke C., Reichardt C. L., Rest A., Ruhl J. E., Saliwanchik B. R., Saro A., Sayre J. T., Schaffer K. K., Shirokoff E., Spieler H. G., Stalder B., Stanford S. A., Staniszewski Z., Stark A. A., Story K. T., Stubbs C. W., Vanderlinde K., Vieira J. D., Williamson R., Zahn O., Zenteno A. The Redshift Evolution of the Mean Temperature, Pressure, and Entropy Profiles in 80 SPT-Selected Galaxy Clusters // The Astrophysical Journal. IX 2014. 794, 1. 67. arXiv: 1404.6250.

McGurk Rosalie C., Kimball Amy E., Ivezić Željko. PRINCIPAL COMPONENT ANALYSIS OF SLOAN DIGITAL SKY SURVEY STELLAR SPECTRA // The Astronomical Journal. III 2010. 139, 3. 1261–1268.

McKinney Wes. Data Structures for Statistical Computing in Python // Proceedings of the 9th Python in Science Conference. 2010. 56–61. Conference Name: Proceedings of the 9th Python in Science Conference.

Merloni A., Predehl P., Becker W., Böhringer H., Boller T., Brunner H., Brusa M., Dennerl K., Freyberg M., Friedrich P., Georgakakis A., Haberl F., Hasinger G., Meidinger N., Mohr J., Nandra K., Rau A., Reiprich T. H., Robrade J., Salvato M., Santangelo A., Sasaki M., Schwope A., Wilms J., Consortium the German eROSITA. eROSITA Science Book: Mapping the Structure of the Energetic Universe // arXiv:1209.3114 [astro-ph]. IX 2012. arXiv: 1209.3114.

Mingers John. An Empirical Comparison of Pruning Methods for Decision Tree Induction // Machine Learning. 1989. 4. 227–243.

Mohr J.J., Mathiesen B., Evrard A.E. Properties of the Intracluster Medium in an ensemble of Nearby Galaxy Clusters // Astrophysical Journal. 1999. 517. 627–649.

Murtagh F., Heck A. Principal Components Analysis // Multivariate Data Analysis. 131. Dordrecht: Springer, 1987. (Astrophysics and Space Science Library).

Mushotzky R. X-ray emission from clusters and groups of galaxies // Proceedings of the National Academy of Sciences. I 1998. 95, 1. 72–77.

Mushotzky R.F. X-ray Emission for Clusters of Galaxies // Physica Scripta. 1984. 1984, 157.

Radiation environment of the Chandra X-Ray Observatory. // . San Diego, CA, USA, XII 2000. 99.

Pace Zachary J., Tremonti Christy, Chen Yanmei, Schaefer Adam L., Bershady Matthew A., Westfall Kyle B., Boquien Médéric, Rowlands Kate, Andrews Brett, Brownstein Joel R., Drory Niv, Wake David. Resolved and Integrated Stellar Masses in the SDSS-IV/MaNGA Survey. II. Applications of PCA-based Stellar Mass Estimates // The Astrophysical Journal. IX 2019. 883, 1. 83.

Peterson J. R., Fabian A. C. X-ray Spectroscopy of Cooling Clusters // Physics Reports. IV 2006. 427, 1. 1–39. arXiv: astro-ph/0512549.

Petralia Francesca, Song Won-Min, Tu Zhidong, Wang Pei. New Method for Joint Network Analysis Reveals Common and Different Coexpression Patterns among Genes and Proteins in Breast Cancer // Journal of Proteome Research. III 2016. 15, 3. 743–754.

Plaa J. de, Kaastra J. S., Tamura T., Pointecouteau E., Mendez M., Peterson J. R. X-ray spectroscopy on Abell 478 with XMM-Newton // Astronomy & Astrophysics. VIII 2004. 423, 1. 49–56.

Quinlan J. R. Induction of decision trees // Machine Learning. III 1986. 1, 1. 81–106.

Rasia E., Mazzotta P., Bourdin H., Borgani S., Tornatore L., Ettori S., Dolag K., Moscardini L. X-MAS2: Study Systematics on the ICM Metallicity Measurements // The Astrophysical Journal. II 2008. 674, 2. 728–741.

Raymond J. C., Smith B. W. Soft X-ray spectrum of a hot plasma // The Astrophysical Journal Supplement Series. XII 1977. 35. 419.

Robitaille Thomas P., Tollerud Erik J., Greenfield Perry, Droettboom Michael, Bray Erik, Aldcroft Tom, Davis Matt, Ginsburg Adam, Price-Whelan Adrian M., Kerzendorf Wolfgang E., Conley Alexander, Crighton Neil, Barbary Kyle, Muna Demitri, Ferguson Henry, Grollier Frédéric, Parikh Madhura M., Nair Prasanth H., Günther Hans M., Deil Christoph, Woillez Julien, Conseil Simon, Kramer Roban, Turner James E. H., Singer Leo, Fox Ryan, Weaver Benjamin A., Zabalza Victor, Edwards Zachary I., Bostroem K. Azalee, Burke D. J., Casey Andrew R., Crawford Steven M., Dencheva Nadia, Ely Justin, Jenness Tim, Labrie Kathleen, Lim Pey Lian, Pierfederici Francesco, Pontzen Andrew, Ptak Andy, Refsdal Brian, Servillat Mathieu, Streicher Ole. Astropy: A community Python package for astronomy // Astronomy & Astrophysics. X 2013. 558. A33. Publisher: EDP Sciences.

Ronen Shai, Aragón-Salamanca Alfonso, Lahav Ofer. Principal component analysis of synthetic galaxy spectra // Monthly Notices of the Royal Astronomical Society. II 1999. 303, 2. 284–296.

THE ROSAT DEEP CLUSTER SURVEY: THE X-RAY LUMINOSITY FUNCTION OUT TO z 0.8. // . 1997. 492. 4.

Sanders J. S., Fabian A. C. A deeper X-ray study of the core of the Perseus galaxy cluster: the power of sound waves and the distribution of metals and cosmic rays // Monthly Notices of the Royal Astronomical Society. XI 2007. 381, 4. 1381–1399.

Sanders J. S., Fabian A. C., Allen S. W., Schmidt R. W. Mapping small-scale temperature and abundance structures in the core of the Perseus cluster // Monthly Notices of the Royal Astronomical Society. IV 2004. 349, 3. 952–972. Publisher: Oxford Academic.

Sanders J. S., Fabian A. C., Frank K. A., Peterson J. R., Russell H. R. Deep high-resolution X-ray spectra from cool-core clusters: Deep X-ray spectra from cool-core clusters // Monthly Notices of the Royal Astronomical Society. II 2010. 402, 1. 127–144.

Sarazin C. L., Koekemoer A. M., Baum S. A., O'Dea C. P., Owen F. N., Wise M. W. X-ray Properties of B2 1028+313: A Quasar at the Center of the Abell Cluster A1030 // The Astrophysical Journal. I 1999. 510, 1. 90–103. arXiv: astro-ph/9806372.

Sarazin Craig L. X-ray emission from clusters of galaxies // Reviews of Modern Physics. I 1986. 58, 1. 1–115.

Schenck David E., Datta Abhirup, Burns Jack O., Skillman Sam. X-RAY OBSERVATIONS OF COMPLEX TEMPERATURE STRUCTURE IN THE COOL-CORE CLUSTER A85 // The Astronomical Journal. VII 2014. 148, 1. 23.

Schindler Sabine. Distant clusters of galaxies: X-ray properties and their relations // arXiv:astro-ph/9908130. VIII 1999. arXiv: astro-ph/9908130.

Shlens Jonathon. A Tutorial on Principal Component Analysis // arXiv:1404.1100 [cs, stat]. IV 2014. arXiv: 1404.1100.

Smith Randall K., Brickhouse Nancy S., Liedahl Duane A., Raymond John C. Collisional Plasma Models with APEC/APED: Emission Line Diagnostics of Hydrogen-like and Helium-like Ions // The Astrophysical Journal. VIII 2001. 556, 2. L91–L95. arXiv: astro-ph/0106478.

Song Yan-yan, Lu Ying. Decision tree methods: applications for classification and prediction // Shanghai Archives of Psychiatry. IV 2015. 27, 2. 130–135.

Tamura T., Bleeker J. A. M., Kaastra J. S., Ferrigno C., Molendi S. XMM-Newton observations of the cluster of galaxies Abell 496: Measurements of the elemental abundances in the intracluster medium // Astronomy & Astrophysics. XI 2001. 379, 1. 107–114.

Tan P.-N., Steinbach M., Kumar V. Introduction to Data Mining. Boston, Ma, USA: Addison-Wesley Longman Publishing Co., Inc., 2005. First.

Tozzi Paolo, Norman Colin. The Evolution of X-ray Clusters and the Entropy of the Intra Cluster Medium // The Astrophysical Journal. I 2001. 546, 1. 63–84. arXiv: astro-ph/0003289.

Uzeirbegovic Emir, Geach James E., Kaviraj Sugata. Eigengalaxies: describing galaxy morphology using principal components in image space // arXiv:2004.06734 [astro-ph]. IV 2020. arXiv: 2004.06734.

Van Rossum Guido, Drake Fred L. Python 3 Reference Manual. Scott's Valley, CA: Create Soace, 2009.

Vikhlinin A., VanSpeybroeck L., Markevitch M., Forman W. R., Grego L. Evolution of the cluster X-ray scaling relations since z>0.4 // The Astrophysical Journal. X 2002. 578, 2. L107–L111. arXiv: astro-ph/0207445.

Virtanen Pauli, Gommers Ralf, Oliphant Travis E., Haberland Matt, Reddy Tyler, Cournapeau David, Burovski Evgeni, Peterson Pearu, Weckesser Warren, Bright Jonathan, Walt Stéfan J. van der, Brett Matthew, Wilson Joshua, Millman K. Jarrod, Mayorov Nikolay, Nelson Andrew R. J., Jones Eric, Kern Robert, Larson Eric, Carey C. J., Polat İlhan, Feng Yu, Moore Eric W., VanderPlas Jake, Laxalde Denis, Perktold Josef, Cimrman Robert, Henriksen Ian, Quintero E. A., Harris Charles R., Archibald Anne M., Ribeiro Antônio H., Pedregosa Fabian, Mulbregt Paul van, Contributors SciPy 1 0. SciPy 1.0–Fundamental Algorithms for Scientific Computing in Python // Nature Methods. III 2020. 17, 3. 261–272. arXiv: 1907.10121.

Walt Stefan van der, Colbert S. Chris, Varoquaux Gael. The NumPy Array: A Structure for Efficient Numerical Computation // Computing in Science Engineering. III 2011. 13, 2. 22–30. Conference Name: Computing in Science Engineering.

Waskom Michael, Botvinnik Olga, O'Kane Drew, Hobson Paul, Lukauskas Saulius, Gemperline David C, Augspurger Tom, Halchenko Yaroslav, Cole John B., Warmenhoven Jordi, Ruiter Julian de, Pye Cameron, Hoyer Stephan, Vanderplas Jake, Villalba Santi, Kunter Gero, Quintero Eric, Bachant Pete, Martin Marcel, Meyer Kyle, Miles Alistair, Ram Yoav, Yarkoni Tal, Williams Mike Lee, Evans Constantine, Fitzgerald Clark, Brian , Fonnesbeck Chris, Lee Antony, Qalieh Adel. mwaskom/seaborn: v0.8.1 (September 2017). IX 2017.

Wilman R. J., Fabian A. C. Fitting the spectrum of the X-ray background: the effects of high metallicity absorption // Monthly Notices of the Royal Astronomical Society. XI 1999. 309, 4. 862–870. arXiv: astro-ph/9907204.

Wold S., Esbensen K., Geladi P. Principal Component Analysis // Chemometrics and Intelligent Laboratory Systems. 1987. 2. 37–52.

Yip C. W., Connolly A. J., Berk D. E. Vanden, Ma Z., Frieman J. A., SubbaRao M., Szalay A. S., Richards G. T., Hall P. B., Schneider D. P., Hopkins A. M., Trump J., Brinkmann J. Spectral Classification of Quasars in the Sloan Digital Sky Survey: Eigenspectra;

Redshift and Luminosity Effects // The Astronomical Journal. XII 2004. 128, 6. 2603–2630. arXiv: astro-ph/0408578.

Zhang Yanxia, Zhang Jingyi, Jin Xin, Zhao Yongheng. A New Strategy for Estimating Photometric Redshifts of Quasars // arXiv:1906.08907 [astro-ph]. XI 2019. arXiv: 1906.08907.

Zhuravleva I., Churazov E., Schekochihin A. A., Allen S. W., Arevalo P., Fabian A. C., Forman W. R., Sanders J. S., Simionescu A., Sunyaev R., Vikhlinin A., Werner N. Turbulent Heating in Galaxy Clusters Brightest in X-rays // Nature. XI 2014. 515, 7525. 85–87. arXiv: 1410.6485.

Chapitre 4

A Machine Learning Approach to Sitelle Spectral Analysis: I. H II Region Kinematics

C.L. Rhea,[1] L. Rousseau-Nepton,[2] Simon Prunet,[2] J. Hlavacek-Larrondo,[1] Sébastian Fabbro, [3,4]

[1]*Département de physique, Université de Montréal, C.P. 6128 Succ. Centre-ville, Montréal H3C 3J7, Canada*
[2]*Canada-France-Hawaii Telescope, Kamuela, HI, United States*
[3]*NRC Herzberg Astronomy and Astrophysics, 5071 West Saanich Road, Victoria, BC, V9E 2E7, Canada*
[4]*Department of Physics and Astronomy, University of Victoria, Victoria, BC, V8P 5C2, Canada*

Cet article a été accepté dans *The Astrophysical Journal* (ApJ) le 18 août 2020. Il est aussi l'objet d'un communiqué de presse du CFHT.

Mots-clés: SITELLE, SIGNALS, région H II, réseau neuronale convolutif

Abstract

SITELLE is a novel integral field unit spectroscopy instrument that has an impressive spatial (11 by 11 arcmin) and spectral coverage (R$\sim$1000-10000). SIGNALS is anticipated to obtain deep observations (down to $3.6 \times 10^{-17} ergs s^{-1} cm^{-2}$) of 40 galaxies, each needing complex and substantial time to extract spectral information. We present a method that uses Convolution Neural Networks (CNN) for estimating emission line parameters in optical

spectra obtained with SITELLE as part of the SIGNALS large program. Our algorithm is trained and tested on synthetic data representing typical emission spectra for H II regions based on Mexican Million Models database (3MdB) BOND simulations. The network's activation map demonstrates its ability to extract the dynamical (broadening and velocity) parameters from a set of 5 emission lines (e.g. Hα, N[II] doublet, and S[II] doublet) in the SN3 (651-685 nm) filter of SITELLE. Once trained, the algorithm was tested on real SITELLE observations in the SIGNALS program of one of the South West fields of M33. The CNN recovers the dynamical parameters with an accuracy better than $5\,\mathrm{km\,s^{-1}}$ in regions with a signal-to-noise ratio greater than 15 over the Hα line. More importantly, our CNN method reduces calculation time by over an order of magnitude on the spectral cube with native spatial resolution when compared with standard fitting procedures. These results clearly illustrate the power of machine learning algorithms for the use in future IFU-based missions. Subsequent work will explore the applicability of the methodology to other spectral parameters such as the flux of key emission lines.

Keywords: SITELLE, SIGNALS, H II regions, Convolutional Neural Network

4.1. Introduction

H II regions lay the foundation of many studies from star-formation in galaxies, to galactic evolution and cosmology, and are one of the main drivers of observational extra-galactic astronomy (e.g. French 1980; Weedman et al. 1981; Veilleux, Osterbrock 1987). H II regions form when the gaseous clumps are irradiated by an interior young and hot star or cluster of stars causing the gas to become partially or completely ionized (e.g. Osterbrock, Ferland 1989; Shields 1990; Franco et al. 2000). They are primarily composed of Hydrogen and Helium, but contain non-negligible amounts of metals and their ionized counterparts (e.g. Shields, Tinsley 1976; Oey, Kennicutt 1993; Kennicutt, Oey 1993; Garnett, Shields 1987). The characteristic bright emission lines coming from recombination and collision between the free electrons and the different atoms/ions in the nebulae are observed at large distances and allow the study of interstellar matter and its primary constituents (e.g. Kewley et al. 2006; Crawford et al. 1999; Baldwin et al. 1981). Additionally, the omnipresence of the H II regions in some galaxies allow for the study of galactic disk dynamics (e.g. Epinat et al. 2008), magnetic fields and turbulence at large and small-scales (e.g. Odell 1986; Haverkorn et al. 2015; Beck et al. 1996; Quireza et al. 2006; Pavel, Clemens 2012), and the importance of various feedback mechanisms that inject energy into the ISM, i.e. stellar winds, supernovae and radiation pressure (e.g. McLeod et al. 2020; Ramachandran et al. 2018, 2019).

More recently, the use of integral field spectroscopy on nearby galactic and extragalactic H II regions has offered a more complete view of their physical properties (e.g. Leroy et al.

2016; Sánchez et al. 2012; Bundy et al. 2014). Also, increasing spectral and spatial resolution has allowed for the study of the complex dynamical structures of the H II regions and pushed the limit of previous analysis methods meant for integrated/unresolved spectra of H II regions (e.g. Martins et al. 2010; Sánchez et al. 2012; Drissen et al. 2014). Typical fitting procedures used to extract the dynamics and emission lines flux measurements from H II regions spectra require a good prior estimate of the velocity as well as the number of velocity components to be fitted (e.g. Zeidler et al. 2019; Bittner et al. 2019; Sánchez et al. 2007). Defining the range of those priors is usually not a problem when the ensemble of spectra shows similar characteristics. While the typical range of velocity seen in galactic disks can easily vary by a few hundreds of $\mathrm{km\,s^{-1}}$ (e.g. Dressler et al. 1983; Bregman 1980; Sancisi et al. 2008), and the internal dynamics of H II regions can add thermal/turbulent broadening and expansion velocity to the galactic contribution (e.g. SOFUE 1995; Arsenault 1986), the typical velocity prior for a given spectral data cube can be very broad and is often not precise enough to ensure a proper fit of the entire data set. We are additionally facing new challenges in the dynamical analysis, because the spatially resolved H II regions spectra often contain emission from different phases of the ISM (along the line of sight) and can be composed of multiple dynamically distinct components (e.g. expanding shells, Rozas et al. 2007; Relaño, Beckman 2005) having each a different thermal/turbulent broadening. Of course, fitting two or more components with the proper velocity and broadening priors is the best approach in such case, but only when such components are actually present in the spectra (e.g. Relaño et al. 2005; Le Coarer, E. et al. 1993).

Ultimately, extracting the information in a consistent manner from high spectral and spatial resolution data cubes requires a dedicated method to estimate the priors on the different spectral parameters, taking into account the variation of the observed spectral features across the field-of-view.

SITELLE, the Imaging Fourier Transform Spectrograph (IFTS) of the Canada-France-Hawaii Telescope (CHFT), produces spectral data cubes containing over 4 million pixels with adjustable resolving power (up to 10,000) and has an instrumental line shape described by a sine cardinal function (Martin, Drissen 2017; Baril et al. 2016; Drissen et al. 2019). Its $11' \times 11'$ field-of-view (FOV) contains more than 4 million pixels for which the spectral sampling and resolution varies as a function of their relative position angle with the mobile mirror. Moreover, emission lines intensities (and therefore line intensity ratios) may vary significantly across the parameter space of the physical properties observed in H II regions.

All together, these characteristics make a typical template fitting strategy (e.g. cross-correlation function maximization) very difficult to implement since the sine cardinal function side lobes affect neighbouring line intensity and shape, and the position of the lobes with respect to the central position of the line varies with spectral resolution (changes across the FOV). In addition, the variation of line intensity ratios between different emission regions

can lead to gross errors on the velocity estimates when a single template spectrum is used. Therefore, an adapted approach is developed here to solve these issues while still fitting entire data cubes, using the same uniform and reproducible method and including the dynamical and spectral complex nature of the resolved H II regions.

This paper explores the use of a Convolution Neural Network to resolve deficiencies in the existing fitting software ORCS – *Outils de Réduction de Cubes Spectraux*. Although the ORCS fitting routines are robust, they require a human-generated prior for all fits; this paper demonstrates the use of machine learning to estimate the priors with no human input. In § 2, we outline the Convolution Neural Network and the synthetic data set used to train the network. We explore the success of our CNN to the synthetic data in § 3. In § 4, we discuss the applicability of our methodology to low resolution spectra. Additionally, we apply the CNN to a field of M33 in order to test its efficacy in real observations. Finally, in § 5, we recap the main successes and outline our future work.

4.2. Methodology

4.2.1. Convolutional Neural Networks

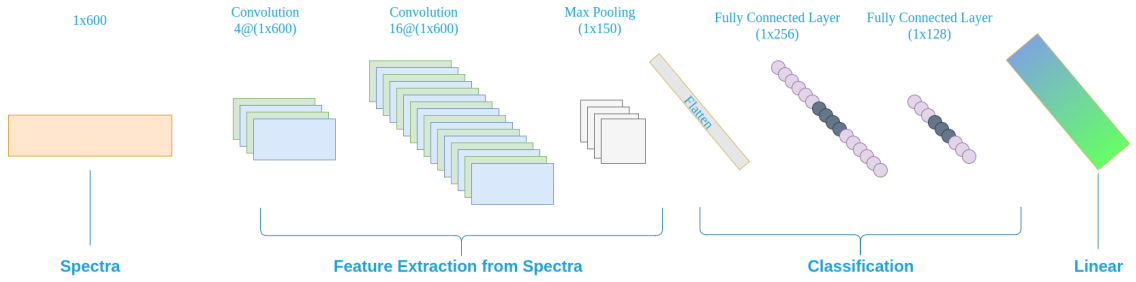

Fig. 4.1. A cartoon of the convolutional neural network used in this work. As described in the text, it is an adaptation of the STARNET topology (Fabbro et al. 2018). The input spectra is first convolved in two separate layers before being condensed in a pooling layer. Once flattened, the vector is passed to two hidden layers. Finally, the velocity and broadening parameters are estimated using two separate output nodes denoted by the blue-green bar.

Neural Networks have been used extensively in astronomy to classify galaxies (Storrie-Lombardi et al. 1992), separate galaxies from stars (Bertin 1994), categorize dynamic parameters of galaxy clusters (e.g. Ntampaka et al. 2016; Ntampaka et al. 2019), explore astrophysical morphologies at differing scales (e.g. Sadaghiani et al. 2019; Iwasaki et al. 2019), derive galaxy redshift from wide band images (Pasquet et al. 2019), and extract emission-line parameters from spectra (e.g. Olney et al. 2020; Ucci et al. 2019; Baron 2019). A recent effort to calculate the parameters of H II regions from their spectra, GAME[1], employs

[1] https://game.sns.it/

a combination of Decision Trees and AdaBoost in order to predict physical parameters (Ucci et al. 2017; Ucci et al. 2018). In lieu of this, our method uses a Convolutional Neural Network (CNN) architecture designed by Fabbro et al. (2018), monikered `STARNET`, which has already demonstrated success in estimating emission-line parameters from stellar spectra.

During the course of this work, we became aware of the work of Keown et al. (2019), which uses an approach similar to ours to estimate the velocity and broadening of high resolution radio emission lines, taking into account possible multiple velocity components. While their work focuses on high resolution, isolated emission lines, ours focuses on lower resolution spectra observed on a wide field of view, hence often with a wide velocity distribution. In addition, the `SITELLE` ILS extended structure prevents us in any case from considering the different emission lines separately.

Our convolutional neural network is graphically depicted in figure 4.1 and laid out as follows:

(1) 8x8 convolution with 4 filters
(2) 4x4 convolution with 8 filters
(3) Global max pooling with 4 filters
(4) 20% dropout
(5) 256 fully-connected nodes
(6) 128 fully-connected nodes
(7) 2 output neurons

The CNN takes the normalized SITELLE emission spectra obtained with the SN3 filter (651-685 nm) and returns an estimate on the velocity ($\mathrm{km\,s^{-1}}$) of the lines and their broadening ($\mathrm{km\,s^{-1}}$), assuming they are consistent over the five major emission lines in SN3. We tested several scaling functions (RobustScaler, StandardScaler, and MinMaxScaler); although we obtained the tightest constraints with the MinMaxScaler, the activation map revealed fitting nonphysical features and noise. We therefore normalize the spectrum to have a maximum value equal to unity.

In order to ensure the appropriate hyper-parameters, we explored their spaces extensively using the random search algorithm, as implemented by `sklearn`, embedded in a 10-fold cross correlataion. Throughout our training, we saw no significant deviation from the results reported by Fabbro et al. (2018). Therefore, we adopted the same hyper-parameter values as used in the standard `STARNET` procedure. Structural hyper-parameters can be readily seen in figure 4.1. In order to view the other parameters (i.e. learning rates, decay rates, etc.), we suggest the reader view our github page: `https://github.com/sitelle-signals/Pomplemousse`. We report a maximum number of 25 epochs and an initial batch size of 2 spectra.

4.2.2. Synthetic Data

In order to demonstrate the feasibility of using a CNN to identify the correct spectral parameters, we construct a set of synthetic data on which to train and test the network. The synthetic data set used in this study was created using the `ORB` software developed to reduce data from `SITELLE` (Martin et al. 2016). To generate synthetic spectra, We use the `ORB create_cm1_lines_model` function which requires a number of parameters that will be defined in this section. Since our tool was developed primarily for SITELLE's programs and the SIGNALS collaboration, we focused on the SN3-filter which covers a band pass between 647 and 685 nm. In accordance with the SIGNALS survey, we select a primary spectral resolving power of 5000, an exposure time of 13.3s per step, and 842 steps (Rousseau-Nepton et al. 2019). In order to replicate the change of spectral resolution across the cube, we allow the resolving power to randomly vary between 4800 and 5000 since the resolution will vary between these values in any given SN3 observation which is a part of the SIGNALS program. We will model the following lines: [N II]λ6548, Hα(6563)Å, [N II]λ6583, [S II]λ6716, and S[II]λ6731. Furthermore, we use the `sincgauss` function as described in Martin et al. (2016) to include line broadening. We randomly varied the velocity between -200 and 200 $\mathrm{km\,s^{-1}}$, while the broadening was randomly varied between 0 and 50 $\mathrm{km\,s^{-1}}$. These ranges were selected from our prior knowledge of the distribution of velocities in M33 (Epinat et al. 2008) and the typical broadening in SITELLE data cubes at this spatial resolution. Note that we randomly selected the resolution, broadening, and velocity parameters with replacement for each synthetic spectrum. The final input required to construct the synthetic spectra is the amplitude of each emission line.

In order to calculate reasonable relative fluxes for the five lines while ensuring we are sampling the desired physical parameter space, we used the 3MdB[2] – Mexican Million Models Database (Morisset et al. 2015). The 3Mdb contains models created using the `CLOUDY v17.01` photoionization code based on a pre-selected set of emission region parameters and underlying ioinizing stellar spectra (Ferland et al. 2017). We use the `BOND` dataset described in Asari et al. (2016) which contains spectra from H II regions similar to those expected to be found in SIGNALS. The `BOND` data-set contains 63000 spectra. Though the data set covers the physical parameter space of the emission nebulae we wish to study, it also contains a number of models that are outside the scope of our study. We describe varying parameters used in table 4.1. While the `BOND` simulations have two simulation geometries, completely filled and thin shell, we remove all thin shell (fraction=0.03) simulations from our sample. This leaves us with filled spheres with a density of approximately 100 $\mathrm{cm^3}$ and represents a younger population of H II regions (e.g. Asari et al. 2016; Stasińska et al. 2015; Cedrés et al. 2013).

[2] `https://sites.google.com/site/mexicanmillionmodels/`

Parameter	Lower Limit	Upper Limit	Step Size
log(U)	-3.5	-2.5	0.5
Age (Myr)	1	6	1
12+log(O/H)	7.4	9.0	0.2
log(N/O)	-2	0	0.5

Table 4.1. H II region parameter selection used during the M3db runs of the `BOND` simulations. The initial run-parameters were cut further in order to focus on the emission expected in the SIGNALS program. The step sizes were set by the 3Mdb runs (see Morisset et al. (2015) for more information)

We further constrained the ionization parameter, U, and metallicity proxy, 12+log(O/H), to focus on SIGNALS-type H II regions (e.g. Rousseau-Nepton et al. 2019; Pérez-Montero et al. 2019; Kashino, Inoue 2019; Zinchenko et al. 2019). With these constraints, we extracted the amplitudes of the five emission lines present in SN3, first randomly selecting a model which passed our selection criteria. We then normalized the amplitudes with respect to Hα. After combining the five lines (with the appropriate instrumental line shape) and the simulated continuum emission, we add a noise component. The noise is sampled from a normal distribution centered at zero with a standard deviation equal to 2% the max amplitude; we indeed expect a nominal signal-to-noise ratio larger than 50 for Hα in the SIGNALS program. SNR effects will be investigated later in the article. Figure 4.2 shows a sample spectrum. At this stage, we create 10,000 mock spectra in the form of `FITS` files which contain the emission parameter information (e.g. velocity, broadening, resolution).

4.2.3. SITELLE Data

4.2.3.1. *Calibration and Data Reduction*

Observations of M33 were taken during the Queued Service Observing period 18B (Program 18BP41, P.I. Laurie Rousseau-Nepton) at the Canada France Hawaii Telescope on the summit of Mauna Kea, Hawaii, using SITELLE. These exposures were taken with the SN3 filter which covers a range from 651-685 nm for a total of 4h with a spectral resolving power of R$\sim$5000. The pointing was centered on a single field in M33 and is part of a larger observation of M33 in its entirety. This observation also forms a basis for the SIGNALS program, lead by Laurie Rousseau-Nepton, which aims to further categorize H II and star-forming regions in nearby galaxies. We note that the authors of this paper are members of the SIGNALS collaboration.

The raw data were reduced and calibrated using SITELLE's personalized software, ORBS (version 3.1.2 Martin et al. 2016). We are able to resolve five spectral emission lines from our observations: [S II]λ6713, [S II]λ6731, [N II]λ6548, Hα, [N II]λ6584. Using the function `SpectralCube.Map_Sky_Velocity()`, we fit the OH sky line velocities, assumed at rest w.r.t.

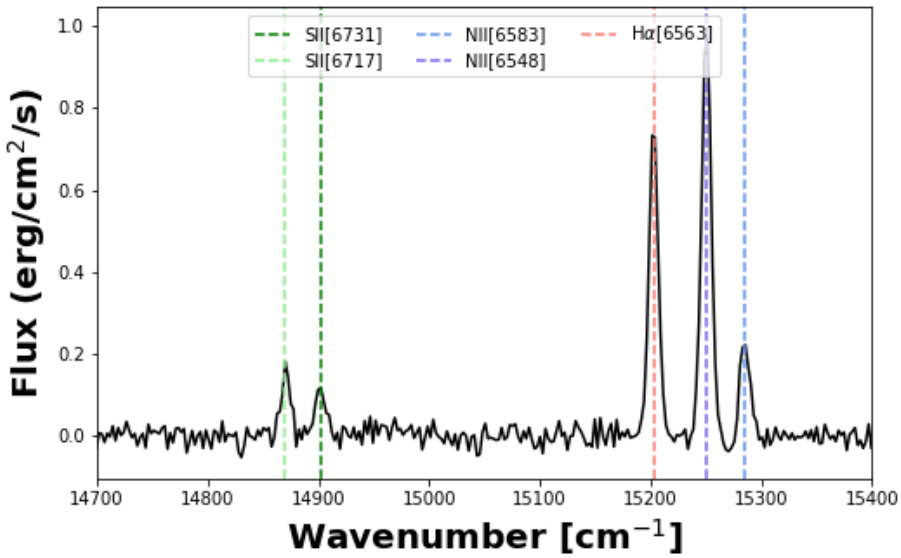

Fig. 4.2. Example spectrum simulated using the process described in §4.2.2. As our population statistics suggest, this is not the only expected spectral shape. However, it is representative of the sample and clearly demonstrates the five emission line peaks. This is the SN3 spectral coverage of SITELLE.

the observer, with a geometric model of the interferometer; afterwards, we used the function `SpectralCube.Correct_Wavelength()` to refine the wavelength calibration of our data cube using the OH-lines fit.

4.3. Results

In this section we apply our convolutional neural network outlined in §4.2.1 to our synthetic spectra with a resolution R∼5000. We retained 70% (7,000) of the spectra as our training set, 20% (2,000) as our validation set, and the remaining 10% (1,000) as the test set (e.g. Tetko, Villa 1997). Training and validating our algorithm results in over 95% accuracy for both predicted parameters: the velocity and the broadening. Accuracy is defined as the ratio of correct parameter estimations to the total number of estimates. An estimate is considered correct if it agrees with the ground truth value up to two digits after the decimal (i.e. to the hundredth place). The combined mean absolute error, another common metric for regression tasks, is 5kms^{-1}. Figures 4.3, 4.4, and 4.5 visually depict the accuracy of the CNN on the test set and the associated residuals, respectively. As the figures depict, the algorithm was well trained and is able to accurately predict both the velocity and the spectral broadening. As evidenced in figures 4.3 and 4.4, the predicted values are close to the ground truth values. The KDE plots in figure 4.3 demonstrate that the parameter space is being well sampled for both the velocity and broadening. Figure 4.5 demonstrates

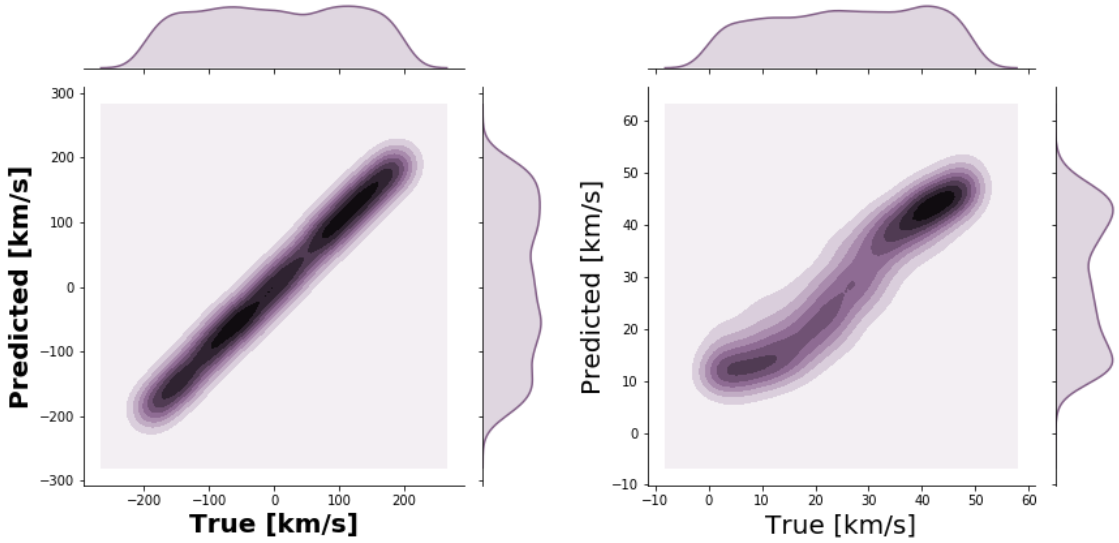

(a) (b)

Fig. 4.3. Kernel Density Estimation (KDE) plots for the test set. Left: True vs Predicted Velocity values in $\mathrm{km\,s^{-1}}$. Right: True vs Predicted Broadening values in $\mathrm{km\,s^{-1}}$. In both plots we can see that the predicted values accurately mimic the true values. Note the change in scales between the two plots.

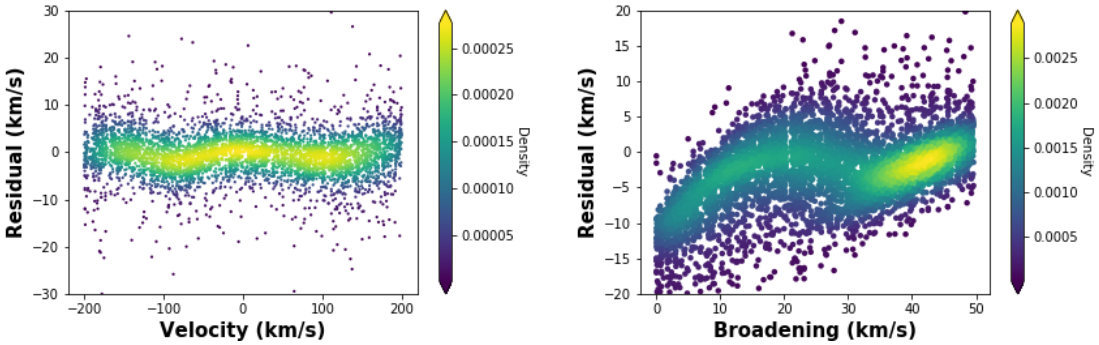

(a) (b)

Fig. 4.4. Left: Velocity Residual as a function of the true velocity. Although there exists a background substructure, it only affects a fraction of a percent of the total test set and is thus negligible. Right:Broadening residual as a function of the true broadening. The pattern demonstrates a bias for low broadening values that is likely caused by the networks inability to distinguish a low amount of broadening. Moreover, the broadening naturally segregates itself into two physical peaks typical of H II regions and supernovae remnants, respectively (e.g. Veilleux, Osterbrock 1987; Vasiliev et al. 2015).

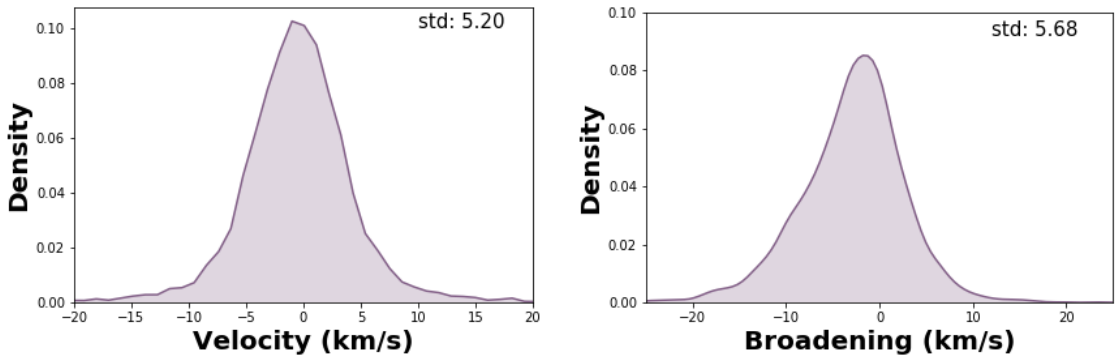

(a) (b)

Fig. 4.5. Left: Density plot of the velocity residuals in $\mathrm{km\,s^{-1}}$ along with the standard deviation. Right: Density plot of the broadening residuals in $\mathrm{km\,s^{-1}}$ in addition to the standard deviation. The asymmetry is likely due to the diversity of resolving power introduced in the training set.

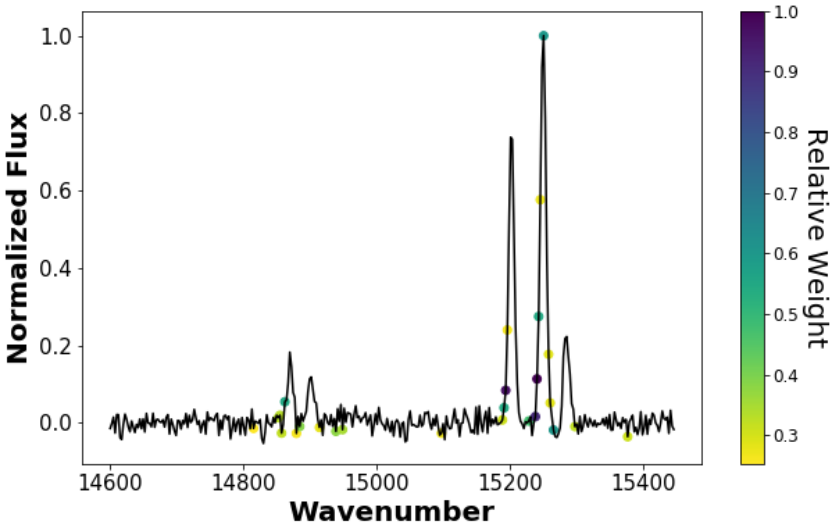

Fig. 4.6. Activation or Saliency Map of our convolutional neural network applied to an example spectrum. The colored points represent the exact locations of the nodes in the input spectrum. Their color indicates their relative weight in the network. Weights under 0.25 are not shown for clarity.

the Gaussian distribution of errors about zero; although the right panel reveals the slightly skewed error distribution of the broadening parameter, the shape is globally Gaussian and any distortion is believed to be caused by asymmetries within the training set. We report a standard deviation of $\sim 20\ \mathrm{km\,s^{-1}}$ for the velocity parameter.

This is well within the required limits as described in Martin et al. (2016) and Rousseau-Nepton et al. (2019) for an initial guess to be supplied to the `ORCS` software. The velocity

error is required to be less than the channel width with corresponds to approximately 40 $\mathrm{km\,s^{-1}}$ for a resolution of 5000. The standard deviation of the broadening parameter is $\sim$ 2.5 $\mathrm{km\,s^{-1}}$. Since SITELLE resolves the broadening parameter down to approximately 3 $\mathrm{km\,s^{-1}}$ for high SNR regions (1000), our broadening errors are well below SITELLE's resolving power.

Although the spread of errors shown in the figure 4.5 do not reveal overt overfitting, we applied a standard k-fold cross-validation algorithm on ten partitions of the training, validation, and test data (e.g. Picard, Cook 1984; Bengio, Grandvalet 2004). We also implemented a modified k-fold cross-validation algorithm in which we varied only the training and validation data while retaining the same test set. We report approximately the same accuracy values (within 5%) regardless of the fold and cross-validation technique. This further indicates the absence of overfitting (e.g. Cawley, Talbot 2010; Molinaro et al. 2005).

Additionally, we created an saliency map of our example spectrum from figure 4.2 which can be seen with the filled circles in figure 4.6. An activation map maps out the regions of the input (in this case the spectrum) used by the convolutional neural network to learn (e.g. Simonyan et al. 2014) by calculating the gradient of the output with respect to the input. We can clearly see by the clustering of data points in the image around the Hα and [N II]λ6548 lines that the network considers these lines to be the most important components for determining the velocity and broadening. This is consistent with our expectations since these two lines, unlike the others, are consistently above the continuum in H II regions. It is sensible that the network does not weigh the [S II] doublet heavily since they are often unobservable due to noise. Moreover, the network does not focus only on the peaks of the Hα and [N II]λ6548 lines, but also on their base. This indicates that the widening of the lines – which is directly affected by the velocity and broadening components – plays a crucial role in parameter estimation, as expected.

4.4. Discussion

While in Section 3, we demonstrated that the CNN algorithm is capable of extracting the correct spectral parameters (velocity and broadening) of the Hα, N[II], S[II] lines for synthetic SITELLE observations, in this Section, we examine the versatility of the model and its robustness when applied to real SITELLE observations. We also discuss the novelty of using such CNN algorithms for IFU observations in general (i.e. from other telescopes, especially in context of upcoming 30 and 40 -m class telescopes.

4.4.1. Versatility of the Model

While this technique is developed for the SIGNALS collaboration science case, aiming to obtain IFU observations of dozens of nearby galaxies, and thus R$\sim$5000, we demonstrate its

applicability to other studies of H II regions using SITELLE at various spectral resolutions. Since there exists a number of other SN3 observations which are not a part of the SIGNALS program that were taken with an average spectral resolving power near R∼2000, we wished to directly test our existing network and weights against synthetic data created with R∼2000 (e.g. Puertas et al. 2019; Gendron-Marsolais et al. 2018; Rousseau-Nepton et al. 2018). However, since the resolution sets the number of steps (i.e. data points) in our spectrum, a reduction of the resolution affects the length of the input data. In order to feed lower resolution spectra into our CNN, we would be required to smooth or interpolate the data so that we would have an input of an equivalent length – a requisite for use in a CNN. In doing so, we would be assuming a form of the interpolation (i.e. linear, a higher-order polynomial, spline, etc.) which might inject non-physical and potentially biased information into the spectra (Horowitz 1974; Scargle 1982; Schulz, Stattegger 1997). We therefore do not modify the spectra, but instead we create an entirely new set of training, validation, and test data using the same routines employed to create our high spectral resolution synthetic dataset with a resolution set to R∼2000.

After creating 10,000 synthetic spectra with a lower spectral-resolution, we divided the set into the training (70%), validation (20%), and test (10%) sets. After training and validating our convolutional neural network, we applied it on our test data. We report a nominal accuracy of both predictors (velocity and broadening) of 92% compared to 95% in the case of R 5000. The standard deviation of the errors for the velocity and broadening are 75 and 12 $\mathrm{km\,s^{-1}}$, respectively. We ran both k-fold cross-validation algorithms and again found consistency across the accuracy predictors. The results are coherent with our supposition that the method would extend well to relatively low resolution spectra since, even at R∼2000, we are able to reasonably resolve the emission lines. The reduced accuracy is reasonable since the emission lines are less well-resolved.

We attempted to use the network to predict low resolution SITELLE spectra (R∼1000); however, at this resolution, the lines are often indistinguishable and the algorithm fails to achieve high-fidelity results. Typical SITELLE's observing strategy for targets in the local Universe and for the SIGNALS project, have an increased spectral resolution for the Hα filter (SN3) and often a lower resolution for other filters (typically R∼1000). The dynamical priors (velocity and broadening) can then be estimated using the higher resolution SN3 filter and applied on the other observations of the same field with the other filters. Overall, our results demonstrate that a CNN network is capable of reliably estimating spectral parameters (velocity and broadening) in SITELLE synthetic observations at high (R=5000) and low (R=2000) resolution, but that beyond R =1000-1500, it fails because of the poor quality of observations. In other words, these results not only demonstrate that machine learning algorithms can be used to estimate kinematic parameters, but they also demonstrate the techniques limitations.

4.4.2. Validation on a Real Data-set: the Case of M33

With the ability of the CNN to predict velocity and broadening parameters accurately for synthetic data, we apply our methodology to an emission region of M33's South-East field (figure 4.7). This region is an excellent test-bed for our algorithm since it contains several types of emission regions (i.e. H II region, planetary nebulae, etc.) and is part of the SIGNALS survey.

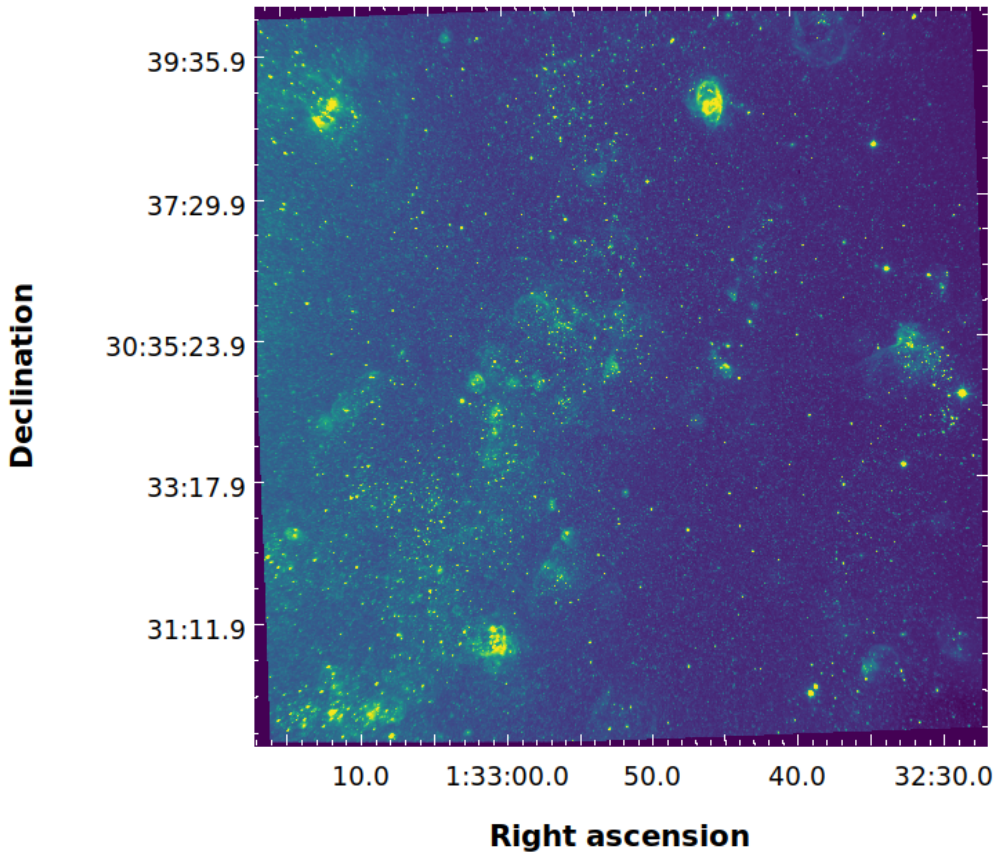

Fig. 4.7. Deep, co-added SITELLE observation (4hr) of M33 Field 7 using the SN3 filter. The image illustrates the density of emission-line regions in the outskirts of M33.

Fits were calculated using the `ORCS fit_lines_in_region()` command centered on our five lines. Each grouping ([S II]λ6713/[S II]λ6731, [N II]λ6548/[N II]λ6584, and Hα) was fit simultaneously with a Gaussian convolved with a sinc function following the standard SITELLE procedure (Martin, Drissen 2017); All lines were tied together with respect to the velocity and broadening. Fits were optimized using the Levenberg-Marquardt least-squares minimization algorithm. In order to execute a fit in `ORCS`, the user is required to input an initial guess for the velocity and broadening parameters; this is due to the nature of the minimization algorithm. The first set of priors were created by initially binning our

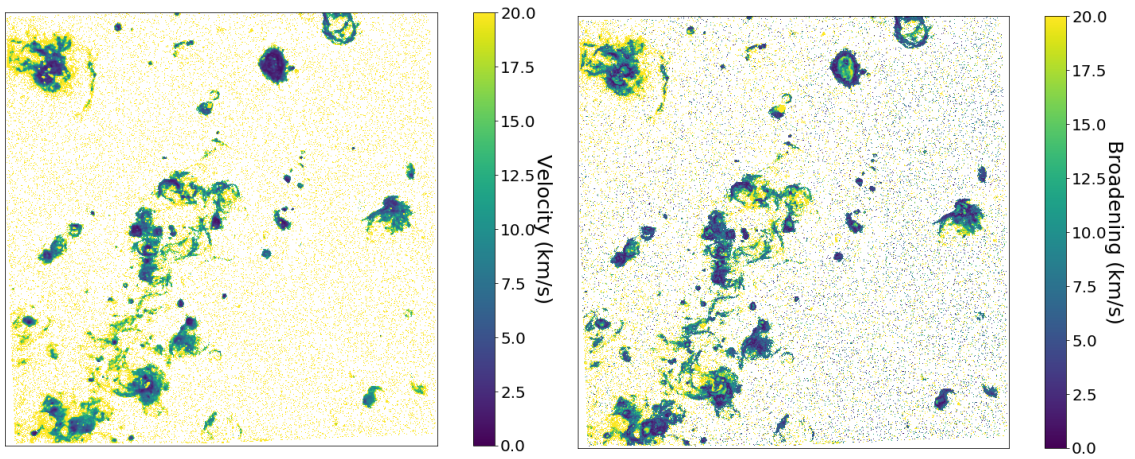

(a) (b)

Fig. 4.8. Left: Residual map of the velocity calculated from the absolute difference between the final ORCS fit and the machine learning priors calculated on an unbinned cube. Right: Residual map of the broadening calculated from the absolute difference between the final ORCS fit and the machine learning priors calculated on an unbinned cube. Both maps were smoothed using a 2-dimensional Gaussian kernel with a sigma value equal to 2 pixels.

cube into spatial bins of 8x8 followed by the standard ORCS fitting procedure. This standard method still requires an initial guess that the user must input. However, the machine learning method for determining priors does not require any user input and can be applied directly on the unbinned data. All fits were run using a computing server located at the CFHT headquarters in Waimea, Hawaii named *iolani*. The server has 2 Intel XEON E5-2630 v3 CPUs operating at 2.40GHz with 8 cores each. The configuration also has 64 GB of RAM available for computing purposes.

A key benefit of the machine learning prior fits over the standard procedure is the economy of time associated with the machine learning algorithm. Since no fitting and iterating is necessary, the calculation time scales approximately linearly with the number of spectra. Using a coarse initial binning, 8x8, the standard algorithm to calculate the priors takes approximately 4 hours in order to cover the entire cube. However, the unparallelized machine learning algorithm takes only 180 seconds[3] to cover the same binned cube. Hence the machine learning algorithm calculates the priors more than 100 times faster than the standard algorithm. We also calculate the time the machine learning algorithm takes to estimate the velocity and broadening parameters for an unbinned cube; this takes approximately 4 hours – the same amount of time to calculate the standard priors on an binned (8x8) cube.

In addition to being considerably faster when estimating the priors, the machine learning algorithm also obtains accurate estimates. In order to quantify this notion, we calculate the

[3]assuming a near-perfect speedup, we expect the parallelized algorithm to take approximately 25 seconds to run on *iolani*.

residual values over the cube between the unbinned final fits – using an 8x8 machine learning prior – and the unbinned machine learning estimates. We only retained pixels for the residual analysis which demonstrated a flux value above our threshold of 1.5×10^{-17} ergs/s. This threshold was chosen since it masks out all `nan` values and maintains the regions with clear emission. Figure 4.8 demonstrates that the residuals are low in central parts of the emission regions, where the signal-to-noise is high, while the residuals are higher in the outskirts where the signal-to-noise is low. This is likely due to the fact that our synthetic data was created using a high signal-to-noise ratio of 50; we will explore the effects of the SNR ratio in a future paper. While it is often desirable to study the emission in the outskirts in addition to the central emission, the low-residual regions outline locations of high-fidelity fits. In order to recover the velocity and broadening parameters in these regions, the machine learning estimates on either the binned or unbinned cube can be used as priors for a standard `ORCS` fit. Moreover, since the standard prior calculation requires binning spatially, substructure information is inherently lost in these priors. On the other hand, the convolutional neural network priors do not require any binning and thus retain all structural spatial information.

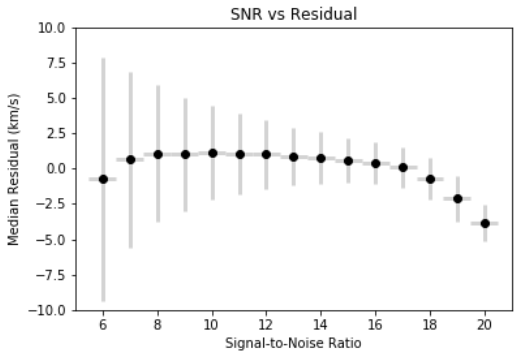

Fig. 4.9. Proxy signal-to-noise ratio versus mean absolute velocity residual ($\mathrm{km\,s^{-1}}$) for the South West field of M33. For each SNR bin, we excluded outliers before calculating the mean absolute residual and standard deviation (grey y-axis error bars). Each SNR bin has a width of 1.

Although we do not study all the complexities of the SNR impact on our CNN in this article, we include a short discussion on it here. We calculate the SNR by dividing the Hα flux by its fit uncertainty as calculated in our final `ORCS` fit. Although this is not exactly the SNR, it acts as a proxy value. With the residual maps and the SNR proxy map, we have the residual and signal-to-noise information for each pixel. We then binned residuals by signal-to-noise ratio with a step size of 1 between 5 and 20. Twenty is the maximum value of the SNR proxy and below 5 we do not see any coherent structure in the spectra. We culled outliers that were outside of the 3-σ range. Finally, we calculated the median absolute residual and standard deviation in each SNR bin. As evidenced by figure 4.9, the accuracy of the CNN increases as the signal-to-noise ratio rises, an expected trend. Figure

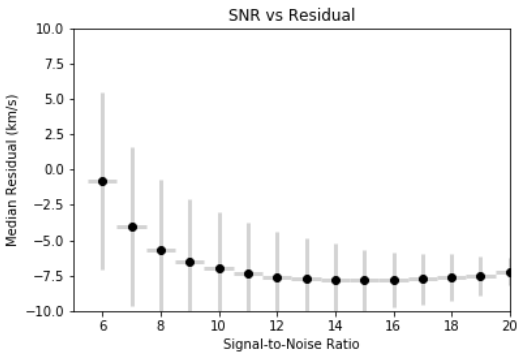

Fig. 4.10. Proxy signal-to-noise ratio versus mean absolute broadening residual ($\mathrm{km\,s^{-1}}$) for the South West field of M33. For each SNR bin, we excluded outliers before calculating the mean absolute residual and standard deviation (grey y-axis error bars). Each SNR bin has a width of 1.

4.10 demonstrates a similar trend in the signal-to-noise ratio until approximately an SNR of 16. The trend unexpectedly reverses for SNR values greater than 16. We report that this is due to the presence of multiple components serendipitously located in high (> 16) SNR regions (see appendix for discussion). Multiple components affect the broadening strong than then velocity estimates since the lines blend together. Even in standard fitting procedures, this poses a serious issue. In our following paper, we will explore the effects of the SNR on the training data.

4.4.3. Universal Applicability

The methodology described in this paper is not limited to SITELLE data cubes. Indeed, the methodology naturally lends itself to any IFU-like data cube in which the observer has access to high-resolution spectral data such as the K-band Multi Object Spectrograph, KMOS (e.g. Sharples et al. 2013), or the Multi Unit Spectroscopic Explorer, MUSE (e.g. Bacon et al. 2010). Since the machine learning algorithm is able to achieve reasonable estimations of the kinetic parameters (velocity and broadening) in a fraction of the time the standard fitting procedures take, it will play a crucial role in upcoming missions aimed at completing large-scale surveys using IFUs such as the Near-Infrared Spectrograph, NIRSpec (e.g. Oliveira de et al. 2018), on the James Webb Space Telescope and the MEGARA – Multi-Espectrógrafo en GTC de Alta Resolución para Astronomía – instrument on the Gran Telescopio Canarias (e.g. Paz et al. 2012).

4.5. Conclusions

A convolution neural network has been exploited in several astronomical applications ranging from dynamic mass estimates of galaxy clusters (e.g. Ntampaka et al. 2019) to the

extraction of spectral parameters (e.g. Fabbro et al. 2018). This work applies a modified `STARNET` architecture (Fabbro et al. 2018) to high resolution (R>2000) SITELLE observations of H II regions in order to estimate the velocity and broadening parameters. Training, validation, and testing the machine learning algorithm with synthetic data integrating the 3Mdb database (Morisset et al. 2015) demonstrates the feasibility of the method. We demonstrate that the algorithm fails to predict the spectral parameters for low resolution (R$\simeq$1000) observations. We believe this is due to the lack of resolved spectral information resulting in partial blending of the main emission lines. However, above R 2000, we are able to disentangle the lines better. We apply the convolutional neural network to the Southwest field of M33 to calculate the velocity and broadening priors. Compared to the standard method for computing the priors, our method is over 100 times faster. Additionally, the machine learning algorithm can reliably estimate the emission-line parameters for the entire unbinned cube in roughly the same amount of time it takes the standard algorithm to calculate the priors on an 8x8 binned cube.

The work presented here represents the first in a series of articles on the applications of machine learning to SITELLE spectra. In a subsequent article, we will present our work on the effects of the signal-to-noise ratio on convolution neural networks and how to mitigate the negative impacts.

We will also demonstrate the applicability of our methodology to calculate the fluxes (and ratios thereof) of emission lines, which will allow for the rapid classification of emission regions through grids of photo-ionization models (e.g. 3MdB). In the third proposed paper of the series, we will describe a machine learning methodology to identify possible multiple, blended components within emission lines.

The authors would like to thank the Canada-France-Hawaii Telescope (CFHT) which is operated by the National Research Council (NRC) of Canada, the Institut National des Sciences de l'Univers of the Centre National de la Recherche Scientifique (CNRS) of France, and the University of Hawaii. The observations at the CFHT were performed with care and respect from the summit of Maunakea which is a significant cultural and historic site. C. R. acknowledges financial support from the physics department of the Université de Montréal. J. H.-L. acknowledges support from NSERC via the Discovery grant program, as well as the Canada Research Chair program.

The progamming aspects of this paper were completed thanks to the following packages of the python programming language (Van Rossum, Drake 2009): `numpy` (Walt van der et al. 2011, `scipy` (Virtanen et al. 2020), `matplotlib` (Hunter 2007), `pandas` (McKinney 2010), `seaborn` (Waskom et al. 2017), `astropy` (Collaboration et al. 2018; Robitaille et al. 2013), `tensorflow` (Abadi et al. 2015, and `keras` (Chollet 2015).

Appendix

SNR and the Residual As noted in §4.4.2, the broadening parameter (and the velocity parameter to a much lesser extent) exhibits an unexpected trend in its SNR vs residual plot (figure 4.10). In this section, we explore potential reasons for this behavior: a dependence on the SNR of the training set, or an effect from multiple line components in high SNR regions. In order to determine whether or not the SNR of the training set has a negative impact on high SNR regions, we create a set of 1,000 synthetic data following the same prescription described before (§4.2); however, we allow the SNR to vary between 20 and 80 instead of being fixed at 50. Because we are only created 1,000 synthetic spectra, we reduce the sampling rate of the velocity and broadening. This is not expected to have any effect on the results. We then apply our already trained network on the synthetic data. Figure

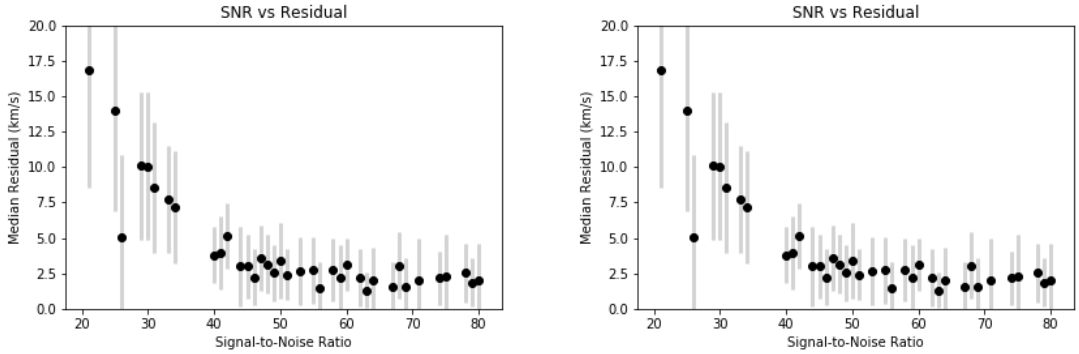

(a) (b)

Fig. 4.11. Left: Proxy signal-to-noise ratio versus mean absolute broadening residual ($\mathrm{km\,s^{-1}}$) for synthetic data created to simulate a range of SNR values. For each SNR bin, we excluded outliers before calculating the mean absolute residual and standard deviation (grey y-axis error bars). Each SNR bin has a width of 1. Right: Ratio of double vs single component AIC parameters for the masked region of interested.

4.11 demonstrates that the network performs well for high SNR values. Thus the network is not biased for high SNR regions. Note that the SNR value used in this section is the true signal-to-noise ratio as compared to that used in §4.4.2 which is a proxy value calculated by dividing the Hα flux by its fit uncertainty.

In order to determine whether or not the regions of high SNR in the South West field of M33 have single or double emission components, we turn to the standard `ORCS` fitting procedure. We selected pixels which fit the following prescription: have a broadening residual higher than 10 $\mathrm{kms^{-1}}$ and a signal-to-noise ratio over 12. We fit the Hα and [N II] doublet assuming a single emission component and a double emission component. The double emission fit resulted in a statistically significantly better fit statistic. This is a strong indication that the region is best described by a double emission component rather than a single

emission component. Moreover, we computed the AIC parameter for each region defined by $AIC = 2n - ln(L)$, where n is the number of fit parameters and L is the Gaussian likelihood function (e.g. Akaike 1987; Liddle 2007; Kieseppa 1997). In our case, the likelihood is Gaussian, therefore the log-likelihood function reduces to the usual half χ-squared. The right hand-size of figure 4.11 shows the ratio of the double component AIC parameter vs the single component AIC parameter defined as $exp(-(AIC_1 - AIC_0)/2)$. Since the ratio is consistently below one, the double component model is favored over the single component model. We thus conclude that, at least in these regions, the rise in the residual value is due to the existence of double component emission. Therefore, we believe that figure 4.10 does not reflect a failure of the network in high SNR regions, but rather a failure of the network in regions with double emission components that serendipitously appear in regions of high SNR in the South West field of M33. Future work will explore the applicability of a modified network to estimate the broadening and velocity parameter in such regions.

References

TensorFlow: Large-Scale Machine Learning on Heterogeneous Distributed Systems. // . 2015. 19.

Akaike Hirotugu. Factor analysis and AIC // Psychometrika. 1987. 52, 3. 317–332.

Arsenault Robin. INTEGRATED Ha PROFILES OF GIANT EXTRAGALACTIC H n REGIONS // Astrophysical Journal. 1986. 92, 3.

Asari N. Vale, Stasińska G., Morisset C., Fernandes R. Cid. BOND: Bayesian Oxygen and Nitrogen abundance Determinations in giant H II regions using strong and semi-strong lines // Monthly Notices of the Royal Astronomical Society. VIII 2016. 460, 2. 1739–1757. arXiv: 1605.01057.

The MUSE second-generation VLT instrument. // . VII 2010. 7735. 773508. Conference Name: Ground-based and Airborne Instrumentation for Astronomy III.

Baldwin J. A., Phillips M. M., Terlevich R. Classification parameters for the emission-line spectra of extragalactic objects // Publications of the Astronomical Society of the Pacific. II 1981. 93. 5.

Baril M.R., Grandmont F.J., Mandar J., Drissen L., Martin T., Rousseau-Nepton L. Commissioning SITELLE: an imaging Fourier transform spectrometer for the Canada France Hawaii Telescope // International Society for Optics and Photonics. Proceedings of SPIE. 2016. 990829.

Baron Dalya. Machine Learning in Astronomy: a practical overview // arXiv:1904.07248 [astro-ph]. IV 2019. arXiv: 1904.07248.

Beck Rainer, Brandenburg Axel, Moss David, Shukurov Anvar, Sokoloff Dmitry. GALACTIC MAGNETISM: Recent Developments and Perspectives // Annual Review of Astronomy and Astrophysics. 1996. 34, 1. 155–206. _eprint: https://doi.org/10.1146/annurev.astro.34.1.155.

Bengio Yoshua, Grandvalet Yves. No Unbiased Estimator of the Variance of K-Fold Cross-Validation // Journal of Machine Learning Research. 2004. 5. 1089–1105.

Bertin E. Classification of Astronomical Images with a Neural Network // Science with Astronomical Near-Infrared Sky Surveys. Dordrecht: Springer Netherlands, 1994. 49–51.

Bittner A., Falcón-Barroso J., Nedelchev B., Dorta A., Gadotti D. A., Sarzi M., Molaeinezhad A., Iodice E., Rosado-Belza D., Lorenzo-Cáceres A. de, Fragkoudi F., Anta P. M. Galán-de, Husemann B., Méndez-Abreu J., Neumann J., Pinna F., Querejeta M., Sánchez-Blázquez P., Seidel M. K. The GIST Pipeline: A Multi-Purpose Tool for the Analysis and Visualisation of (Integral-field) Spectroscopic Data // Astronomy & Astrophysics. VIII 2019. 628. arXiv: 1906.04746.

Bregman J. N. The galactic fountain of high-velocity clouds // The Astrophysical Journal. III 1980. 236. 577–591.

Bundy Kevin, Bershady Matthew A., Law David R., Yan Renbin, Drory Niv, MacDonald Nicholas, Wake David A., Cherinka Brian, Sánchez-Gallego José R., Weijmans Anne-Marie, Thomas Daniel, Tremonti Christy, Masters Karen, Coccato Lodovico, Diamond-Stanic Aleksandar M., Aragón-Salamanca Alfonso, Avila-Reese Vladimir, Badenes Carles, Falcón-Barroso Jésus, Belfiore Francesco, Bizyaev Dmitry, Blanc Guillermo A., Bland-Hawthorn Joss, Blanton Michael R., Brownstein Joel R., Byler Nell, Cappellari Michele, Conroy Charlie, Dutton Aaron A., Emsellem Eric, Etherington James, Frinchaboy Peter M., Fu Hai, Gunn James E., Harding Paul, Johnston Evelyn J., Kauffmann Guinevere, Kinemuchi Karen, Klaene Mark A., Knapen Johan H., Leauthaud Alexie, Li Cheng, Lin Lihwai, Maiolino Roberto, Malanushenko Viktor, Malanushenko Elena, Mao Shude, Maraston Claudia, McDermid Richard M., Merrifield Michael R., Nichol Robert C., Oravetz Daniel, Pan Kaike, Parejko John K., Sanchez Sebastian F., Schlegel David, Simmons Audrey, Steele Oliver, Steinmetz Matthias, Thanjavur Karun, Thompson Benjamin A., Tinker Jeremy L., Bosch Remco C. E. van den, Westfall Kyle B., Wilkinson David, Wright Shelley, Xiao Ting, Zhang Kai. OVERVIEW OF THE SDSS-IV MaNGA SURVEY: MAPPING NEARBY GALAXIES AT APACHE POINT OBSERVATORY // The Astrophysical Journal. XII 2014. 798, 1. 7.

Cawley Gavin C, Talbot Nicola L C. On Over-fitting in Model Selection and Subsequent Selection Bias in Performance Evaluation // Journal of Machine Learning Research. 2010. 11. 2079–2107.

Cedrés B., Beckman J. E., Bongiovanni A., Cepa J., Ramos A. Asensio, Giammanco C., Cabrera-Lavers A., Alfaro E. The filling factor - radius relation for 58 HII regions across

the disk of NGC6946 // The Astrophysical Journal. II 2013. 765, 1. L24. arXiv: 1302.1009.

Chollet Fancois. Keras. 2015.

Collaboration The Astropy, Price-Whelan A. M., Sipőcz B. M., Günther H. M., Lim P. L., Crawford S. M., Conseil S., Shupe D. L., Craig M. W., Dencheva N., Ginsburg A., VanderPlas J. T., Bradley L. D., Pérez-Suárez D., Val-Borro M. de, Aldcroft T. L., Cruz K. L., Robitaille T. P., Tollerud E. J., Ardelean C., Babej T., Bachetti M., Bakanov A. V., Bamford S. P., Barentsen G., Barmby P., Baumbach A., Berry K. L., Biscani F., Boquien M., Bostroem K. A., Bouma L. G., Brammer G. B., Bray E. M., Breytenbach H., Buddelmeijer H., Burke D. J., Calderone G., Rodríguez J. L. Cano, Cara M., Cardoso J. V. M., Cheedella S., Copin Y., Crichton D., DÁvella D., Deil C., Depagne É, Dietrich J. P., Donath A., Droettboom M., Earl N., Erben T., Fabbro S., Ferreira L. A., Finethy T., Fox R. T., Garrison L. H., Gibbons S. L. J., Goldstein D. A., Gommers R., Greco J. P., Greenfield P., Groener A. M., Grollier F., Hagen A., Hirst P., Homeier D., Horton A. J., Hosseinzadeh G., Hu L., Hunkeler J. S., Ivezić Ž, Jain A., Jenness T., Kanarek G., Kendrew S., Kern N. S., Kerzendorf W. E., Khvalko A., King J., Kirkby D., Kulkarni A. M., Kumar A., Lee A., Lenz D., Littlefair S. P., Ma Z., Macleod D. M., Mastropietro M., McCully C., Montagnac S., Morris B. M., Mueller M., Mumford S. J., Muna D., Murphy N. A., Nelson S., Nguyen G. H., Ninan J. P., Nöthe M., Ogaz S., Oh S., Parejko J. K., Parley N., Pascual S., Patil R., Patil A. A., Plunkett A. L., Prochaska J. X., Rastogi T., Janga V. Reddy, Sabater J., Sakurikar P., Seifert M., Sherbert L. E., Sherwood-Taylor H., Shih A. Y., Sick J., Silbiger M. T., Singanamalla S., Singer L. P., Sladen P. H., Sooley K. A., Sornarajah S., Streicher O., Teuben P., Thomas S. W., Tremblay G. R., Turner J. E. H., Terrón V., Kerkwijk M. H. van, Vega A. de la, Watkins L. L., Weaver B. A., Whitmore J. B., Woillez J., Zabalza V. The Astropy Project: Building an inclusive, open-science project and status of the v2.0 core package // The Astronomical Journal. VIII 2018. 156, 3. 123. arXiv: 1801.02634.

Crawford C. S., Allen S. W., Ebeling H., Edge A. C., Fabian A. C. The ROSAT Brightest Cluster Sample (BCS): – III. Optical spectra of the central cluster galaxies // Monthly Notices of the Royal Astronomical Society. VII 1999. 306, 4. 857–896. arXiv: astro-ph/9903057.

Dressler Alan, Sandage Allan, Wilson Mount. ROTATIONAL VELOCITIES AND CENTRAL VELOCITY DISPERSIONS FOR A SAMPLE OF SO GALAXIES // Astrophysical Journal. 1983. 265. 664–680.

Drissen Laurent, Martin Thomas, Rousseau-Nepton Laurie, Robert Carmelle, Martin R Pierre, Baril Marc, Prunet Simon, Joncas Gilles, Thibault Simon, Brousseau Denis, Mandar Julie, Grandmont Frédéric, Yee Howard, Simard Luc. SITELLE: an Imaging Fourier Transform Spectrometer for the Canada–France–Hawaii Telescope // Monthly Notices of the Royal Astronomical Society. V 2019. 485, 3. 3930–3946.

Drissen Laurent, Rousseau-Nepton Laurie, Lavoie Sébastien, Robert Carmelle, Martin Thomas, Martin Pierre, Mandar Julie, Grandmont Frédéric. Imaging FTS: A Different Approach to Integral Field Spectroscopy // Advances in Astronomy. 2014. 2014. 1–15.

Epinat B., Amram P., Marcelin M. GHASP: an H kinematic survey of 203 spiral and irregular galaxies - VII. Revisiting the analysis of H data cubes for 97 galaxies // Monthly Notices of the Royal Astronomical Society. IX 2008.

Fabbro Sebastien, Venn Kim, O'Briain Teaghan, Bialek Spencer, Kielty Collin, Jahandar Farbod, Monty Stephanie. An Application of Deep Neural Networks in the Analysis of Stellar Spectra // Monthly Notices of the Royal Astronomical Society. IV 2018. 475, 3. 2978–2993. arXiv: 1709.09182.

Ferland G. J., Chatzikos M., Guzmán F., Lykins M. L., Hoof P. A. M. van, Williams R. J. R., Abel N. P., Badnell N. R., Keenan F. P., Porter R. L., Stancil P. C. The 2017 Release of Cloudy // arXiv:1705.10877 [astro-ph]. VI 2017. arXiv: 1705.10877.

Franco J, Kurtz S E, García-Segura G, Hofner P. THE EVOLUTION OF HII REGIONS // Astrophysics and Space Science. 2000. 272. 169–179.

French Howard B. GALAXIES WITH THE SPECTRA OF GIANT H n REGIONS // Astrophysical Journal. 1980. 240. 41–59.

Garnett D R, Shields G A. THE COMPOSITION GRADIENT ACROSS M8 // Astrophysical Journal. 1987. 317. 82–101.

Gendron-Marsolais M., Hlavacek-Larrondo J., Martin T. B., Drissen L., McDonald M., Fabian A. C., Edge A. C., Hamer S. L., McNamara B., Morrison G. Revealing the velocity structure of the filamentary nebula in NGC 1275 in its entirety // Monthly Notices of the Royal Astronomical Society: Letters. V 2018. arXiv: 1802.00031.

Haverkorn Marijke, Akahori Takuya, Carretti Ettore, Ferriere Katia, Frick Peter, Gaensler Bryan, Heald George, Johnston-Hollitt Melanie, Jones David, Landecker Tom, Mao Sui Ann, Noutsos Aris, Oppermann Niels, Reich Wolfgang, Robishaw Timothy, Scaife Anna, Schnitzeler Dominic, Stepanov Rodion, Sun Xiaohui, Taylor Russ. Measuring magnetism in the Milky Way with the Square Kilometre Array // arXiv:1501.00416 [astro-ph]. I 2015. arXiv: 1501.00416.

Horowitz L.L. The efffects of spline interpolation on power spectral density // IEE transactions on Acoustics, Speech, and Signal Processing. 1974. ASSP-22. 22–27.

Hunter John D. Matplotlib: A 2D Graphics Environment // Computing in Science Engineering. V 2007. 9, 3. 90–95. Conference Name: Computing in Science Engineering.

Iwasaki Hiroyoshi, Ichinohe Yuto, Uchiyama Yasunobu. X-ray Study of Spatial Structures in Tycho's Supernova Remnant Using Unsupervised Deep Learning // Monthly Notices of the Royal Astronomical Society. IX 2019. 488, 3. 4106–4116. arXiv: 1907.09210.

Kashino Daichi, Inoue Akio K. Disentangling the physical parameters of gaseous nebulae and galaxies // Monthly Notices of the Royal Astronomical Society. VI 2019. 486, 1.

1053–1069.

Kennicutt R.C., Oey M.S. Systematic of HII region abundances in galaxies // Revista Mexicana de Astronomía y Astrofísica. 1993. 27. 21–28.

Keown Jared, Francesco James Di, Teimoorinia Hossen, Rosolowsky Erik, Chen Michael Chun-Yuan. CLOVER: Convnet Line-fitting Of Velocities in Emission-line Regions // The Astrophysical Journal. X 2019. 885, 1. 32. Publisher: American Astronomical Society.

Kewley Lisa J., Groves Brent, Kauffmann Guinevere, Heckman Tim. The Host Galaxies and Classification of Active Galactic Nuclei // Monthly Notices of the Royal Astronomical Society. XI 2006. 372, 3. 961–976. arXiv: astro-ph/0605681.

Kieseppa I. Akaike information criterion, curve-fitting, and the philosophical problem of simplicity // The British Journal for the Philosophy of Science. III 1997. 48, 1. 21–48.

Le Coarer, E. , Rosado M., Georgelin Y., Viale A., Goldes G. HAlpha survery of the Small Magellanic Cloud // Astronomy & Astrophysics. 1993. 280. 365–372.

Leroy Adam K., Hughes Annie, Schruba Andreas, Rosolowsky Erik, Blanc Guillermo A., Bolatto Alberto D., Colombo Dario, Escala Andres, Kramer Carsten, Kruijssen J. M. Diederik, Meidt Sharon, Pety Jerome, Querejeta Miguel, Sandstrom Karin, Schinnerer Eva, Sliwa Kazimierz, Usero Antonio. A PORTRAIT OF COLD GAS IN GALAXIES AT 60 pc RESOLUTION AND A SIMPLE METHOD TO TEST HYPOTHESES THAT LINK SMALL-SCALE ISM STRUCTURE TO GALAXY-SCALE PROCESSES // The Astrophysical Journal. X 2016. 831, 1. 16.

Liddle A. R. Information criteria for astrophysical model selection // Monthly Notices of the Royal Astronomical Society: Letters. V 2007. 377, 1. L74–L78.

Martin Thomas, Drissen Laurent. Calibrations of SITELLE's first data release // arXiv:1706.03230 [astro-ph]. VI 2017. arXiv: 1706.03230.

Martin Thomas B., Prunet Simon, Drissen Laurent. Optimal fitting of Gaussian-apodized or under-resolved emission lines in Fourier transform spectra providing new insights on the velocity structure of NGC 6720 // Monthly Notices of the Royal Astronomical Society. XII 2016. 463, 4. 4223–4238.

Martins F., Pomarès M., Deharveng L., Zavagno A., Bouret J. C. Near-IR integral field spectroscopy of ionizing stars and young stellar objects on the borders of H II regions // Astronomy and Astrophysics. II 2010. 510. A32.

McKinney Wes. Data Structures for Statistical Computing in Python // Proceedings of the 9th Python in Science Conference. 2010. 56–61. Conference Name: Proceedings of the 9th Python in Science Conference.

McLeod Anna F., Kruijssen J. M. Diederik, Weisz Daniel R., Zeidler Peter, Schruba Andreas, Dalcanton Julianne J., Longmore Steven N., Chevance Mélanie, Faesi Christopher M., Byler Nell. Stellar Feedback and Resolved Stellar IFU Spectroscopy in the nearby Spiral Galaxy NGC 300 // arXiv:1910.11270 [astro-ph]. I 2020. arXiv: 1910.11270.

Molinaro A. M., Simon R., Pfeiffer R. M. Prediction error estimation: a comparison of resampling methods // Bioinformatics. VIII 2005. 21, 15. 3301–3307.

A VIRTUAL OBSERVATORY FOR PHOTOIONIZED NEBULAE: THE MEXICAN MILLION MODELS DATABASE (3MDB). // . 2015. 3. 19.

Ntampaka M., Trac H., Sutherland D. J., Fromenteau S., Póczos B., Schneider J. DYNAMICAL MASS MEASUREMENTS OF CONTAMINATED GALAXY CLUSTERS USING MACHINE LEARNING // The Astrophysical Journal. XI 2016. 831, 2. 135.

Ntampaka M., ZuHone J., Eisenstein D., Nagai D., Vikhlinin A., Hernquist L., Marinacci F., Nelson D., Pakmor R., Pillepich A., Torrey P., Vogelsberger M. A Deep Learning Approach to Galaxy Cluster X-ray Masses // The Astrophysical Journal. V 2019. 876, 1. 82. arXiv: 1810.07703.

Odell C. R. Turbulent motion in galactic H II regions // The Astrophysical Journal. V 1986. 304. 767.

Oey M.S., Kennicutt R.C. Abundances of HII regions in early-type spiral galaxies // Astrophysical Journal. 1993. 411. 137–152.

Oliveira Catarina Alves de, Birkmann Stephan M., Boeker Torsten, Ferruit Pierre, Giardino Giovanna, Luetzgendorf Nora, Puga Elena, Rawle Tim, Sirianni Marco, Plate Maurice te. Preparing the NIRSpec/JWST science data calibration: from ground testing to sky // arXiv:1805.06922 [astro-ph]. V 2018. arXiv: 1805.06922.

Olney Richard, Kounkel Marina, Schillinger Chad, Scoggins Matthew T., Yin Yichuan, Howard Erin, Covey K. R., Hutchinson Brian, Stassun Keivan G. APOGEE Net: Improving the derived spectral parameters for young stars through deep learning // arXiv:2002.08390 [astro-ph]. II 2020. arXiv: 2002.08390.

Osterbrock D.E., Ferland G.J. Astrophysics of gaseous nebulae and active galactic nuclei. Sausalito, CA USA: University Science Books, 1989. 1.

Pasquet Johanna, Bertin Emmanuel, Treyer Marie, Arnouts Stéphane, Fouchez Dominique. Photometric redshifts from SDSS images using a Convolutional Neural Network // Astronomy & Astrophysics. I 2019. 621. A26. arXiv: 1806.06607.

Pavel Michael D., Clemens D. P. H II REGION DRIVEN GALACTIC BUBBLES AND THEIR RELATIONSHIP TO THE GALACTIC MAGNETIC FIELD // The Astrophysical Journal. XII 2012. 760, 2. 150.

Paz A, Carrasco Esperanza, Gallego Jesús, Sanchez F., Medina J, Vargas M {Garc'i}a, Arrillaga X., Carrera M., Castillo-Morales África, Castillo-Domínguez Edgar, Cedazo Raquel, Eliche-Moral M. Carmen, Ferrusca D., Gonzalez-Guardia E., Maldonado Manuel, Marino Raffaella, Delgado I {Mart'i}nez, Morales Isis, Mujica Einar, Vega O. MEGARA: the future optical IFU and multi-object spectrograph for the 10.4m GTC Telescope // SPIE. 8446. IX 2012.

Picard Richard R., Cook R. Dennis. Cross-Validation of Regression Models // Journal of the American Statistical Association. 1984. 79, 387. 575–583. Publisher: [American Statistical Association, Taylor & Francis, Ltd.].

Puertas S. Duarte, Iglesias-Páramo J., Vilchez J. M., Drissen L., Kehrig C., Martin T. Searching for intergalactic star forming regions in Stephan's Quintet with SITELLE. I. Ionised gas structures and kinematics // Astronomy & Astrophysics. IX 2019. 629. A102. arXiv: 1909.05797.

Pérez-Montero Enrique, García-Benito Rubén, Vílchez José M. Revisiting the hardening of the stellar ionizing radiation in galaxy discs // Monthly Notices of the Royal Astronomical Society. III 2019. 483, 3. 3322–3335.

Quireza Cintia, Rood Robert T., Bania T. M., Balser Dana S., Maciel Walter J. The Electron Temperature Gradient in the Galactic Disk // The Astrophysical Journal. XII 2006. 653, 2. 1226–1240.

Ramachandran Varsha, Hamann W.-R., Hainich R., Oskinova L. M., Shenar T., Sander A. A. C., Todt H., Gallagher J. S. Stellar population of the superbubble N206 in the LMC II. Parameters of the OB and WR stars, and the total massive star feedback // Astronomy & Astrophysics. VII 2018. 615. A40. arXiv: 1802.07494.

Ramachandran Varsha, Hamann W.-R., Oskinova L. M., Gallagher J. S., Hainich R., Shenar T., Sander A. A. C., Todt H., Fulmer L. Testing massive star evolution, star-formation history and feedback at low metallicity : Spectroscopic analysis of OB stars in the SMC Wing // Astronomy & Astrophysics. V 2019. 625. A104. arXiv: 1903.01762.

Relaño M., Beckman J. E. Expansive components in H II regions // Astronomy & Astrophysics. II 2005. 430, 3. 911–926.

Relaño M., Beckman J. E., Zurita A., Rozas M., Giammanco C. The internal dynamical equilibrium of H II regions: A statistical study // Astronomy & Astrophysics. II 2005. 431, 1. 235–251.

Robitaille Thomas P., Tollerud Erik J., Greenfield Perry, Droettboom Michael, Bray Erik, Aldcroft Tom, Davis Matt, Ginsburg Adam, Price-Whelan Adrian M., Kerzendorf Wolfgang E., Conley Alexander, Crighton Neil, Barbary Kyle, Muna Demitri, Ferguson Henry, Grollier Frédéric, Parikh Madhura M., Nair Prasanth H., Günther Hans M., Deil Christoph, Woillez Julien, Conseil Simon, Kramer Roban, Turner James E. H., Singer Leo, Fox Ryan, Weaver Benjamin A., Zabalza Victor, Edwards Zachary I., Bostroem K. Azalee, Burke D. J., Casey Andrew R., Crawford Steven M., Dencheva Nadia, Ely Justin, Jenness Tim, Labrie Kathleen, Lim Pey Lian, Pierfederici Francesco, Pontzen Andrew, Ptak Andy, Refsdal Brian, Servillat Mathieu, Streicher Ole. Astropy: A community Python package for astronomy // Astronomy & Astrophysics. X 2013. 558. A33. Publisher: EDP Sciences.

Rousseau-Nepton L., Martin R. P., Robert C., Drissen L., Amram P., Prunet S., Martin T., Moumen I., Adamo A., Alarie A., Barmby P., Boselli A., Bresolin F., Bureau M., Chemin L., Fernandes R. C., Combes F., Crowder C., Della Bruna L., Egusa F., Epinat B., Ksoll V. F., Girard M., Llanos V. Gómez, Gouliermis D., Grasha K., Higgs C., Hlavacek-Larrondo J., Ho I.-T., Iglesias-Páramo J., Joncas G., Kam Z. S., Karera P., Kennicutt R. C., Klessen R. S., Lianou S., Liu L., Liu Q., Amorim A. Luiz de, Lyman J. D., Martel H., Mazzilli-Ciraulo B., McLeod A. F., Melchior A.-L., Millan I., Mollá M., Momose R., Morisset C., Pan H.-A., Pati A. K., Pellerin A., Pellegrini E., Pérez I., Petric A., Plana H., Rahner D., Lara T. Ruiz, Sánchez-Menguiano L., Spekkens K., Stasińska G., Takamiya M., Asari N. Vale, Vílchez J. M. SIGNALS: I. Survey Description // Monthly Notices of the Royal Astronomical Society. XI 2019. 489, 4. 5530–5546. arXiv: 1908.09017.

Rousseau-Nepton Laurie, Robert Carmelle, Drissen Laurent, Martin R. Pierre, Martin Thomas. NGC628 with SITELLE : I. Imaging Spectroscopy of 4285 HII region candidates // Monthly Notices of the Royal Astronomical Society. 2018. arXiv: 1704.05121.

Rozas M., Richer M. G., Steffen W., García-Segura G., López J. A. H line profiles for a sample of supergiant HII regions: III. Model line profiles // Astronomy & Astrophysics. V 2007. 467, 2. 603–610.

SOFUE Yoshiaki. Galactic Center Molecular Arms, Ring and Expanding Shells.I. Kinematical Structures in Longitude-Velocity Diagrams // PASJ. X 1995. 47, 5. arXiv: astro-ph/9508110.

Sadaghiani Mahya, Sanchez-Monge a, Schilke Peter, Liu Hauyu Baobab, Clarke Seamus, Zhang Qizhou, Girart Josep Miquel, Seifried Daniel, Aghababaei Atefeh, Li Hua-bai, Juarez Carmen, Tang Kwok Sun. Physical Properties of the star-forming clusters in NGC 6334 // arXiv:1911.06579 [astro-ph]. XI 2019. arXiv: 1911.06579.

Sancisi Renzo, Fraternali Filippo, Oosterloo Tom, Hulst Thijs van der. Cold gas accretion in galaxies // The Astronomy and Astrophysics Review. VI 2008. 15, 3. 189–223.

Scargle J. D. Studies in astronomical time series analysis. II - Statistical aspects of spectral analysis of unevenly spaced data // The Astrophysical Journal. XII 1982. 263. 835.

Schulz Michael, Stattegger Karl. Spectrum: spectral analysis of unevenly spaced paleoclimatic time series // Computers & Geosciences. XI 1997. 23, 9. 929–945.

Sharples R., Bender R., Agudo Berbel A., Bezawada N., Castillo R., Cirasuolo M., Davidson G., Davies R., Dubbeldam M., Fairley A., Finger G., Förster Schreiber N., Gonte F., Hess A., Jung I., Lewis I., Lizon J.-L., Muschielok B., Pasquini L., Pirard J., Popovic D., Ramsay S., Rees P., Richter J., Riquelme M., Rodrigues M., Saviane I., Schlichter J., Schmidtobreick L., Segovia A., Smette A., Szeifert T., Kesteren A. van, Wegner M., Wiezorrek E. First Light for the KMOS Multi-Object Integral-Field Spectrometer // The Messenger. III 2013. 151. 21–23.

Shields G. A. Extragalactic H II Regions // Annual Review of Astronomy and Astrophysics. 1990. 28, 1. 525–560. _eprint: https://doi.org/10.1146/annurev.aa.28.090190.002521.

Shields G. A., Tinsley B. M. Composition gradients across spiral galaxies. II - The stellar mass limit // The Astrophysical Journal. I 1976. 203. 66.

Simonyan K., Vedaldi A., Zisserman A. Deep inside convolutional networks: Visualising image classification models and saliency maps // Proc. ICLR. 2014.

Stasińska G., Izotov Yu., Morisset C., Guseva N. Excitation properties of galaxies with the highest [O iii]/[O ii] ratios: No evidence for massive escape of ionizing photons // Astronomy & Astrophysics. IV 2015. 576. A83.

Storrie-Lombardi M. C., Lahav O., Sodre L., Storrie-Lombardi L. J. Morphological Classification of galaxies by Artificial Neural Networks // Monthly Notices of the Royal Astronomical Society. XI 1992. 259, 1. 8P–12P.

Sánchez S. F., Pérez E., Sánchez-Blázquez P., García-Benito R., Ibarra-Mede H. J., González J. J., Rosales-Ortega F. F., Sánchez-Menguiano L., Ascasibar Y., Bitsakis T., Law D., Cano-Díaz M., López-Cobá C., Marino R. A., Paz A. Gil de, López-Sánchez A. R., Barrera-Ballesteros J., Galbany L., Mast D., Abril-Melgarejo V., Roman-Lopes A. Pipe3D, a pipeline to analyse integral field spectroscopy data: II. Analysis sequence and CALIFA dataproducts // Revista Mexicana de Astronomía y Astrofísica. 2007. arXiv: 1602.01830.

Sánchez S. F., Rosales-Ortega F. F., Marino R. A., Iglesias-Páramo J., Vílchez J. M., Kennicutt R. C., Díaz A. I., Mast D., Monreal-Ibero A., García-Benito R., Bland-Hawthorn J., Pérez E., González Delgado R., Husemann B., López-Sánchez Á. R., Cid Fernandes R., Kehrig C., Walcher C. J., Paz A. Gil de, Ellis S. Integral field spectroscopy of a sample of nearby galaxies: II. Properties of the H ii regions // Astronomy & Astrophysics. X 2012. 546. A2.

Tetko I.V., Villa A.E.P. Efficient Partition of Learning Data Sets for Neural Network Training // Neural Networks. 1997. 10, 8. 1361–1374.

Ucci Graziano, Ferrara Andrea, Gallerani Simona, Pallottini Andrea. Inferring physical properties of galaxies from their emission line spectra // Monthly Notices of the Royal Astronomical Society. II 2017. 465, 1. 1144–1156. arXiv: 1611.00768.

Ucci Graziano, Ferrara Andrea, Gallerani Simona, Pallottini Andrea, Cresci Giovanni, Kehrig Carolina, Hunt Leslie K., Vilchez José M., Vanzi Leonardo. The interstellar medium of dwarf galaxies: new insights from Machine Learning analysis of emission line spectra // Monthly Notices of the Royal Astronomical Society. II 2019. 483, 1. 1295–1313. arXiv: 1810.10548.

Ucci Graziano, Ferrara Andrea, Pallottini Andrea, Gallerani Simona. GAME: GAlaxy Machine learning for Emission lines // Monthly Notices of the Royal Astronomical Society. VI 2018. 477, 2. 1484–1494. arXiv: 1803.10236.

Van Rossum Guido, Drake Fred L. Python 3 Reference Manual. Scott's Valley, CA: Create Soace, 2009.

Vasiliev E. O., Moiseev A. V., Shchekinov Yu. A. Velocity Dispersion of Ionized Gas and Multiple Supernova Explosions // Open Astronomy. I 2015. 24, 2.

Veilleux Sylvain, Osterbrock Donald E. SPECTRAL CLASSIFICATION OF EMISSION-LINE GALAXIES // Astrophysical Journal Supplement Series. 1987. 63. 295–310.

Virtanen Pauli, Gommers Ralf, Oliphant Travis E., Haberland Matt, Reddy Tyler, Cournapeau David, Burovski Evgeni, Peterson Pearu, Weckesser Warren, Bright Jonathan, Walt Stéfan J. van der, Brett Matthew, Wilson Joshua, Millman K. Jarrod, Mayorov Nikolay, Nelson Andrew R. J., Jones Eric, Kern Robert, Larson Eric, Carey C. J., Polat İlhan, Feng Yu, Moore Eric W., VanderPlas Jake, Laxalde Denis, Perktold Josef, Cimrman Robert, Henriksen Ian, Quintero E. A., Harris Charles R., Archibald Anne M., Ribeiro Antônio H., Pedregosa Fabian, Mulbregt Paul van, Contributors SciPy 1 0. SciPy 1.0–Fundamental Algorithms for Scientific Computing in Python // Nature Methods. III 2020. 17, 3. 261–272. arXiv: 1907.10121.

Walt Stefan van der, Colbert S. Chris, Varoquaux Gael. The NumPy Array: A Structure for Efficient Numerical Computation // Computing in Science Engineering. III 2011. 13, 2. 22–30. Conference Name: Computing in Science Engineering.

Waskom Michael, Botvinnik Olga, O'Kane Drew, Hobson Paul, Lukauskas Saulius, Gemperline David C, Augspurger Tom, Halchenko Yaroslav, Cole John B., Warmenhoven Jordi, Ruiter Julian de, Pye Cameron, Hoyer Stephan, Vanderplas Jake, Villalba Santi, Kunter Gero, Quintero Eric, Bachant Pete, Martin Marcel, Meyer Kyle, Miles Alistair, Ram Yoav, Yarkoni Tal, Williams Mike Lee, Evans Constantine, Fitzgerald Clark, Brian , Fonnesbeck Chris, Lee Antony, Qalieh Adel. mwaskom/seaborn: v0.8.1 (September 2017). IX 2017.

Weedman D. W., Feldman F. R., Balzano V. A., Ramsey L. W., Sramek R. A., Wuu C.-C. NGC 7714 - The prototype star-burst galactic nucleus // The Astrophysical Journal. VIII 1981. 248. 105.

Zeidler Peter, Nota Antonella, Sabbi Elena, Luljak Peter, McLeod Anna F., Grebel Eva K., Pasquali Anna, Tosi Monica. The young massive star cluster Westerlund 2 observed with MUSE. II. MUSEpack – a Python package to analyze the kinematics of young star clusters // The Astronomical Journal. X 2019. 158, 5. 201. arXiv: 1909.08143.

Zinchenko I A, Dors O L, Hagele G F, Cardaci M V, Krabbe A C. Effective temperature of ionizing stars of extragalactic H II regions–II: nebular parameter relations based on CALIFA data // MNRAS. 2019. 483, 2. 1901–1911.

Chapitre 5

Conclusions

Dans ce mémoire, nous avons exploré plusieurs projets portant sur les galaxies et les amas de galaxies; un sur l'ICM, un sur l'application de l'apprentissage automatique sur l'ICM et finalement un sur l'application directe de l'apprentissage automatique sur les spectres de SITELLE. Un amas de galaxies dans lequel la formation stellaire est extrêmement élevée présentement ($\sim 900 M_{\odot}/yr$), était le premier projet de ma maîtrise. Malgré le fait que l'enquête était classique, le projet a présenté plusieurs défis. En effet, il s'agit d'un des amas les plus lointains jamais observés en rayons X. Par conséquent, cette étude est devenue complexe et il a fallu trouver une façon d'extraire le plus d'information possible à partir de quelques centaines de photons. Je me suis mis à lire en détail la littérature sur les amas lointains et les techniques pour extraire leurs propriétés thermiques. Ma revue de la littérature nous a permis d'explorer plusieurs nouvelles techniques plausibles, ce qui a mené à une analyse. Les résultats de ce travail démontrent que cet amas contient un coeur froid qui est en train de s'effondrer sans le contrepoids de la rétroaction. De plus, le coeur froid est situé à presque 50 kpc de la BCG. C'est à cause de cette distance que la rétroaction n'affecte pas l'écoulement froid et donc l'écoulement peut s'effondrer et créer des étoiles. Il s'agit d'une découverte majeure qui remet en question les processus fondamentaux de formation d'étoiles dans l'univers lointain.

Le deuxième article se concentre sur l'apprentissage automatique et son application aux amas de galaxies. Notre approche consiste à utiliser directement les spectres rayons X pour entraîner nos réseaux. Plus précisément, nous utilisons l'apprentissage automatique pour déterminer le nombre de composantes thermiques sous-jacentes dans les amas de galaxies en étudiant leurs spectres. Avant ce travail, il n'y avait aucune méthodologie standard utilisée dans la communauté pour déterminer le nombre de composantes thermiques sous-jacentes présentes dans l'ICM, ce qui entraînait beaucoup d'erreurs dans les publications. Nous avons démontré qu'une combinaison de l'analyse de composantes principales et d'un classificateur

d'arbre aléatoire peut bien prédire ce chiffre. L'analyse de composantes principales réduit les spectres en leurs composantes les plus importantes, et permet donc de négliger la structure sans importance dans les spectres. Nous utilisons ensuite un classificateur d'arbre aléatoire pour classifier les spectres par leur nombre de composantes thermiques en utilisant les composantes principales. Nos résultats montrent que cette méthodologie nous permet de classifier les spectres avec une bonne précision. Nous classifions un spectre avec une seule composante thermique 83% du temps, un spectre avec deux composantes 80% du temps, un spectre avec trois composantes 96% du temps, et un spectre avec quatre ou plus que quatre composantes 80% du temps. Pour démontrer l'efficacité de notre méthodologie, nous l'avons appliquée directement à l'amas de galaxies de Persée. Nos résultats confirment qu'il existe plusieurs composantes thermiques dans l'amas. Au cours des prochains mois, nous planifions écrire un article de suivi dans lequel nous explorerons l'applicabilité d'un réseau de neurones pour estimer la température de ces composantes.

Dans le troisième article, nous nous sommes concentrés sur les spectres dans le visible mesurés par SITELLE. Cependant, cette fois nous avons utilisé un réseau de neurones convolutif qui prend les spectres bruts et trouve la vitesse et l'élargissement spectral des raies d'émission. Nous avons entraîné notre algorithme avec les données synthétiques créées avec `ORBS` — un logiciel écrit spécifiquement pour la réduction de données de SITELLE. Nous trouvons que lorsqu'appliqué aux données, notre réseau permet d'obtenir des paramètres spectraux presque autant précis que ceux obtenus via l'ajustement effectué par le logiciel `ORCS`. En outre, nous démontrons que le réseau utilise uniquement les raies d'émission pertinentes dans ses calculs. Nous utilisons aussi notre réseau pour estimer l'élargissement et la vitesse dans M33 — une galaxie proche avec plusieurs structures différentes dans le visible. Nous constatons que notre algorithme trouve des valeurs similaires à celles trouvées par `ORCS`. Or, la puissance de notre réseau est sa vitesse de calcul sans précédent avec laquelle elle fait les calculs. `ORCS` prend 10 jours à ajuster un cube spectral de SITELLE, tandis que notre réseau prend 4 heures à calculer les deux paramètres pour un cube entier. Ainsi, notre méthodologie réduit le temps nécessaire pour faire des calculs par plus d'un ordre de grandeur. Malgré le fait que nous avons appliqué cette méthode uniquement aux données de SITELLE, nous pouvons faire de petites modifications à notre algorithme afin de l'appliquer à d'autres données prises par des instruments similaires, tels que MUSE qui se trouve au Chili.

.

Pendant les mois de février et mars, j'ai aussi effectué un stage sur l'île d'Hawaii avec Dr Rousseau-Nepton. J'ai décidé de faire ce stage puisque nous voulions étudier les données prises par SITELLE pour mon doctorat; j'ai donc profité de cette expérience pour connaître l'instrument, faire des contacts et aider l'équipe de logiciels. Grâce à cette expérience, je suis désormais capable de réduire et analyser les cubes spectraux de SITELLE avec une

connaissance profonde des techniques requises. De plus, mon travail sur l'application de l'apprentissage automatique aux données SITELLE m'a mérité une place sur l'équipe de SIGNALS menée par Dr Rousseau-Nepton. Le travail que j'ai fait pendant ce stage formera la base de mon doctorat.

On a notamment déjà commencé à appliquer l'apprentissage automatique à d'autres facettes des spectres de SITELLE. On travaille sur un projet dans lequel nous essayons d'estimer les ratios des lignes d'émission importantes dans un spectre. Nos résultats préliminaires suggèrent que cette méthode va réduire significativement le temps nécessaire à les calculer et va nous donner les résultats avec une précision de même ordre que celle des techniques standards. En outre, dans un autre projet que nous venons de débuter, nous utilisons un réseau de neurones artificiel pour classifier le type d'émission. Nous nous attendons à ce que cette méthode nous permette de classifier l'émission plus précisément que les méthodes standards comme le diagramme de type Baldwin, Phillips et Telervich. Ces deux travaux sont uniques dans leur approche et représentent le type de travail que je planifie explorer pendant mon doctorat sous la supervision de Dr Hlavacek-Larrondo.

Annexe A

Autres publications à titre de co-auteur

A.1. On the Relation between Mini-Halos and AGN Feedback in Clusters of Galaxies

Auteurs: Richard-Laferrière A., Hlavacek-Larrondo J., Nemmen R.S., Rhea C.L., Taylor G.B., Prasow-Émond M., Gendron-Marsolais M.-L., Latulippe M., Edge A.C., Fabian A.C., Hogan M.T., Sanders J.S., Demontigny G.

Contributions de Carter Rhea: Analyse en rayons X de MACS J1447.4+0827 et la section §2.2.1. Calculs des propriétés en rayons X dans le tableau 3 et A2.

A.2. A Multiwavength Study Of The Massive Cool Core Cluster MACS J1447.4+0827

Auteurs: Prasow-Émond M., Hlavacek-Larrondo J., Rhea C.L., Latulippe M., Gendron-Marsolais M.-L., Richard-Laferrière A., Sanders J.S., Edge A.C., Allen S.W., Mantz A., Von der Linden A.

Contributions de Carter Rhea: Analyse en rayons X de MACS J1447.4+0827 et écriture des sections §2.1, 3.1, 4.1, 4.2.

Annexe B

Congrès où l'étudiant a présenté ses résultats

B.1. The Epoch of Galaxy Quenching

Médium: Présentateur sélectionné
Titre: Extreme Stellar Formation in a z=1.7 Galaxy Cluster
Lieu: Cambridge, UK
Année: 2020
Auteurs: C.L. Rhea et J. Hlavacek-Larrondo

B.2. 20 Years of Chandra

Médium: Affiche
Titre: Extreme Stellar Formation in a z=1.7 Galaxy Cluster
Lieu: Boston, MA
Année: 2019
Auteurs: C.L. Rhea et J. Hlavacek-Larrondo

B.3. The 12th Great Lakes Cosmology Workshop

Médium: Présentateur sélectionné
Titre: The Massive Galaxy Clusters SpARCS1049: A History
Lieu: Rochester, NY
Année: 2019
Auteurs: C.L. Rhea et J. Hlavacek-Larrondo

B.4. CASCA Annual General Meeting

Médium: Affiche
Titre: Explaining the Formidable Stellar Formation Rate of a Massive Galaxy Cluster at z=1.7
Lieu: Montréal, QC
Année: 2019
Auteurs: C.L. Rhea et J. Hlavacek-Larrondo

B.5. CRAQ Annual Meeting

Médium: Présentateur
Titre: Extreme Stellar Formation in a z=1.7 Galaxy Cluster
Lieu: Lac à l'eau claire, QC
Année: 2019
Auteurs: C.L. Rhea et J. Hlavacek-Larrondo

Annexe C

Demandes du temps observationnelles

Télescope (Instrument)	Identifiant	Temps	Cibles	Rôle	PI	Année
CFHT (SITELLE)	2020BC001	5 heures	M87	P.I.	Carter Rhea	2020
OMM	2020A	5 heures	Lyra Complex	P.I.	Carter Rhea	2020
CFHT (SITELLE)	20AD99	5 heures	NGC 1275	P.I.	Carter Rhea	2020
JVLA	20A-198	20 heures	Coma Cluster	Co-I et Phase 2	Julie Hlavacek-Larrondo	2019
Gemini North		2 heures	SpARCS 1049	Co-I	Tracy Webb	2019

Tableau C.1. Demandes de temps observationnelles